Fluorescent excitation of interstellar H2

Black, J.H.; Dishoeck, E.F. van

Citation

Black, J. H., & Dishoeck, E. F. van. (1987). Fluorescent excitation of interstellar H2. Retrieved from https://hdl.handle.net/1887/1982

THE ASTROPHYSICAL JOURNAL, 322:412–449, 1987 November 1

FLUORESCENT EXCITATION OF INTERSTELLAR H_2

JOHN H. BLACK
Steward Observatory, University of Arizona

AND

EWINE F. VAN DISHOECK[1]
Harvard-Smithsonian Center for Astrophysics
Received 1987 March 5; accepted 1987 April 22

ABSTRACT

Detailed models of interstellar clouds are used to investigate the infrared emission spectrum of H_2 excited by ultraviolet absorption and fluorescence. The populations of all accessible states of H_2 with rotational quantum number $J \leq 15$ are computed as functions of depth through the model clouds. The fluorescence spectrum in the infrared is sensitive primarily to the density and to the intensity of the ultraviolet radiation at the cloud boundary. Some details of the H_2 line emission are also affected by temperature, by the properties of the grains, and by the initial population distribution of the H_2 molecules upon formation. A finding list is presented for the stronger infrared lines of H_2, with wavelengths based on the best available spectroscopic data. Specific excitation by H Lyman-α radiation is considered as well. The differences between the H_2 infrared spectra due to the fluorescence process and to collisional excitation in a region of high temperature are explored.

A variety of recent observational results are discussed with reference to the theoretical models. The rich H_2 emission spectrum of the reflection nebula NGC 2023 can be reproduced by a model with density $n_H \approx 10^4$ cm^{-3}, $T \approx 80$ K, and an ultraviolet flux approximately 300 times that of the Galactic background starlight. The model is consistent with other observations, provides constraints on the scattering properties of the grains at ultraviolet wavelengths and on the models for the formation process of H_2 on the surfaces of grains, and suggests that H_2 lines contribute significantly to broad-band flux measurements at wavelengths 0.9–1.65 μm. The role of fluorescent excitation is explored for NGC 7027, the Galactic center, and the "bright bar" region of the Orion Nebula. Fluxes are predicted for fluorescent lines of H_2 in T Tauri, the discussion of which is relevant to Herbig-Haro objects as well. The potential use of H_2 fluorescence as a measure of star-forming activity is examined for unresolved ensembles of early-type stars and molecular clouds.

Subject headings: infrared: spectra — interstellar: molecules — line identifications — molecular processes — nebulae: planetary — nebulae: reflection

I. INTRODUCTION

The hydrogen molecule, H_2, is expected to be the most abundant molecule in interstellar space. In quiescent interstellar clouds, H_2 has been observed directly only by means of its ultraviolet absorption lines along lines of sight where the total visual extinction is $A_V^{\rm tot} \leq 2$ mag (Carruthers 1970; Spitzer and Jenkins 1975; Savage *et al.* 1977). In thicker quiescent clouds, the enormous ultraviolet extinction will prevent such observations; however, the intrinsically weak quadrupole vibration-rotation lines within the electronic ground state are, in principle, observable in absorption toward highly obscured infrared sources, and the expected line intensities are comparable to current limits of detectability in at least one cloud (Black and Willner 1984). In disturbed interstellar gas, where excited vibrational levels of H_2 are significantly populated, the infrared vibration-rotation lines can be observed in emission (Shull and Beckwith 1982 and references therein). Vibrational excitation temperatures $T_{\rm ex} \geq 1000$ K can be maintained either directly by collisional excitation in gas heated by shocks (Shull and Beckwith 1982) or intense ultraviolet radiation, or indirectly in colder regions as a consequence of absorption of ultraviolet starlight in the Lyman and Werner band systems followed by fluorescence. The fluorescence process has been discussed by Gould and Harwit (1963), by Black and Dalgarno (1976), by Shull (1978*a*), and by Black, Porter, and Dalgarno (1981).

Most previous observations of the infrared line emission of H_2 at 2 μm have yielded line intensity ratios that are consistent with thermal excitation in shocked regions (Shull and Beckwith 1982; Beckwith *et al.* 1983). Despite various earlier attempts to detect the infrared line emission due to radiative excitation of H_2 (Werner and Harwit 1968; Gull and Harwit 1971; Traub, Carleton, and Black 1978), it has only recently been identified unambiguously in Orion (Hayashi *et al.* 1985), and toward the reflection nebulae NGC 2023 (Gatley and Kaifu 1987; Gatley *et al.* 1987; Hasegawa *et al.* 1987) and Parsamyan 18 (Sellgren 1986). Owing to their proximity to bright early-type stars, reflection nebulae are excellent places to search for fluorescent H_2 emission, the intensity of which should scale with the intensity of the ultraviolet radiation field.

Ultraviolet photons with $\lambda > 912$ Å incident upon a molecular cloud can be absorbed by H_2 in its Lyman and Werner band systems. The initial absorptions are followed by fluorescence to the vibrational continuum of the ground state with a typical average probability of 0.10. This constitutes the principal dissociation process in the boundary layer of a cloud (Solomon 1965, as cited by

---

[1] Junior Fellow, Harvard Society of Fellows.

Field, Somerville, and Dressler 1966). The remaining 90% of the fluorescent transitions populate various bound excited vibration-rotation levels of the ground state. Molecules in these excited states then decay by the electric quadrupole transitions in the infrared on time scales of 10^6 s (Black and Dalgarno 1976). Because fluorescent excitation and dissociation result from the same initial absorptions, the total abundance of H_2 and its excited state populations are strongly coupled. Since the rates of ultraviolet absorption decrease rapidly with increasing optical depth in the lines, both the abundance and the excitation of H_2 are severely depth-dependent. Steady state models of interstellar clouds can be constructed to describe in detail the depth-dependent concentrations of H_2 in its various vibration-rotation levels (Black and Dalgarno 1977; van Dishoeck and Black 1986). The spectrum of infrared lines of H_2 produced by fluorescent excitation can be calculated from such models for comparison with observations.

Black and Dalgarno (1976) described the vibrational and rotational excitation of H_2 through the use of cascade matrices that characterize the efficiency with which ultraviolet fluorescence into some level (v_0, J_0) leads ultimately into levels ($v = 0$, J). This technique is valid only when the ultraviolet absorption rates are much smaller than the rates of spontaneous transitions in the vibration-rotation cascade, so that an excited molecule has time to relax to the ground vibrational state before it is likely to absorb another ultraviolet photon. As pointed out by Shull (1978*a*), an excited molecule can be as likely to absorb an ultraviolet photon as to emit an infrared photon when the ultraviolet radiation field is 10^4 or more times as intense as the mean starlight background in the Galaxy. In this regime of so-called multiple pumping, the excitation of $H_2(v \geq 1)$ depends not only on the quadrupole vibration-rotation transition probabilities but also on details of the radiative transfer of the ultraviolet pumping radiation. Shull (1978*a*) described the vibrational excitation and fluorescence of H_2 in the strong field case, but did not treat the rotational population distributions. Black and Dalgarno (1976) performed fully depth-dependent calculations of the populations of all vibrational states and of a limited number ($J \leq 10$) of rotational levels within them, but their results apply only in the low-field, single-pumping regime. In neither case were the effects of other physical properties, such as density, temperature, and intensity of radiation field, explored over a wide range of parameter space. In the present work, detailed models of the structure of and abundances in interstellar clouds (cf. van Dishoeck and Black 1986, hereafter vDB) have been used to compute explicitly the populations of 211 vibration-rotation levels ($v = 0$–14; $J \leq 15$) of H_2 as functions of depth. The principal remaining limitation of the present calculation is the neglect of vibrationally inelastic collisions, for which the rates are still highly uncertain. This restricts the applicability of these results to situations where the total hydrogen density is $n_{\rm H} = n({\rm H}) + 2n({\rm H}_2) \leq 10^5$ cm^{-3}. The current models are also unrealistic for temperatures $T > 2000$ K. The H_2 infrared line emission from regions with higher densities, $n_{\rm H} = 10^4$–10^8 cm^{-3}, which are exposed to more intense radiation, has recently been considered by Sternberg (1986).

Tielens and Hollenbach (1985*a*, *b*) have discussed the structure and chemistry of "photodissociation regions" in which surfaces of molecular clouds are exposed to intense ultraviolet fluxes. Their calculations were concerned primarily with the chemistry, heat balance, and atomic fine-structure line emission in such regions. Their representation of H_2 as a two-level system was adequate to explore some chemical effects of vibrationally excited H_2, but not to predict its spectrum due to fluorescence. The work reported here is complementary in that it is concerned primarily with the detailed description of the excitation of H_2 and of its radiatively excited infrared spectrum. As pointed out by Tielens and Hollenbach (1985*a*, *b*), the same ultraviolet photons that excite H_2 are effective in ionizing C, dissociating CO, and heating the gas. This theme has been pursued in the present work with respect to the relations between fluxes of atomic lines and fluxes of the infrared lines of H_2. The present models also include the effects of ultraviolet photoionization of excited $H_2(v \geq 4)$ upon the ionization and chemistry in "photodissociation regions." These and other chemical effects of excited H_2 will be discussed in more detail elsewhere (Black and van Dishoeck 1987, hereafter Paper II). As in our previous work (vDB), the thermal balance in the cloud is not considered explicitly in the models. Rather, the temperature and density are assumed either to be constant throughout the cloud or to satisfy a polytropic equation of state.

There are circumstances where the ultraviolet fluorescence of H_2 is directly observable: in the solar atmosphere (Jordan *et al.* 1977, 1978; Shull 1978*b*; Bartoe *et al.* 1979; Sandlin *et al.* 1986), in T Tauri stars and Herbig-Haro objects (Brown *et al.* 1981; Brown, Ferraz, and Jordan 1984; Schwartz 1983; Schwartz, Dopita, and Cohen 1985), and potentially in comets (Feldman and Fastie 1973) and supernova remnants (Raymond *et al.* 1981; Benvenuti, Dopita, and D'Odorico 1980). In these situations, the H_2 is excited not by an ultraviolet continuum but by strong emission lines such as H I Lyα and Lyβ, with which there are accidental resonances with H_2 lines. This resonance fluorescence will also inevitably lead to excitation of a limited number of infrared lines. This has been discussed very recently in reference to Herbig-Haro objects by Schwartz, Cohen, and Williams (1987). Although in many of these regions the resonance fluorescence will often be outshone in the infrared by strong collisionally excited emission, we have investigated the influence of the H I Lyα line on the fluorescent H_2 infrared spectrum.

The main goal of this paper is to use comprehensive models of interstellar clouds (cf. vDB) to compute the spectrum of fluorescent H_2 line emission and to relate its intensity to such cloud properties as density, size, temperature, and intensity of the ultraviolet radiation field. In § II we review the theory of fluorescent excitation, in § III we discuss the model infrared spectra, and in § IV we consider various applications ranging from reflection nebulae to the nuclei of starburst galaxies.

II. RADIATIVE EXCITATION OF H_2

We consider the abundance and excitation of H_2 in plane-parallel clouds. The techniques for computing steady state cloud models as described in vDB have been applied here with two modifications. First, the computation has been enlarged to include all 211 bound levels of all vibrational levels, $v = 0$–14, of the $X\,^1\Sigma_g^+$ state of H_2 with J up to an arbitrary limit of 15, and to treat explicitly the rates of *all* electronic transitions involving these levels. Second, photoionization out of excited H_2 levels with $v \geq 4$ is included explicitly, and the effect of direct photodissociation out of $v \geq 3$ is considered.

The reader is referred to vDB for background details. As discussed there, it is assumed that the abundance of H_2 is in steady state governed primarily by the rate of formation on grain surfaces and the rates of destruction by spontaneous fluorescent dissociation following absorption in the $B\,^1\Sigma_u^+$–$X\,^1\Sigma_g^+$ Lyman and $C\,^1\Pi_u$–$X\,^1\Sigma_g^+$ Werner band systems. Other formation and destruction mechanisms are included in the chemical network, but these tend to be of minor importance in the present context of high ultraviolet radiation fields and modest ($n_{\rm H} < 10^5$ cm^{-3}) densities. In notation similar to that of vDB, the concentration n_{vJ} in a level vJ of the $X\,{}^1\Sigma_g^+$ electronic state of H_2 at a certain depth into the cloud given by

$$n_{vJ}\left[A_{vJ}^X + (k_{vJ}^{\rm ex} - k_{vJ,vJ}^{\rm fl}) + \sum_i \sum_{J' \neq J} n(i) q_i(J, J')\delta_{v,0} + k_{vJ}^d + k_{vJ}^{\rm pi} + 1.051\zeta_0\right]$$
$$= n_{\rm H}\, n({\rm H}) k_{vJ}^{\varphi} + \sum_{v'=0}^{14} \sum_{J'=0}^{15} n_{v'J'}\left[A_{v'J',vJ} + k_{vJ,v'J'}^{\rm fl} + \sum_i n(i) q_i(J', J)\delta_{v',0}\right](1 - \delta_{vJ,v'J'})\,. \quad (1)$$

The spontaneous transition probabilities $A_{v'J',vJ}$ for the quadrupole vibration-rotation lines have been taken from Turner, Kirby-Docken, and Dalgarno (1977), and their sums over all final states for each initial state are defined by $A_{vJ}^X = \sum_{v''}\sum_{J''} A_{vJ,v''J''}$. Ultraviolet absorption out of level vJ leads to fluorescent excitation at a rate $k_{vJ}^{\rm ex}$ and to spontaneous radiative dissociation at a rate k_{vJ}^d. The specific rate at which absorption out of $v'J'$ populates level vJ by fluorescence is denoted by $k_{vJ,v'J'}^{\rm fl}$. The Kronecker delta function, $\delta_{v,0}$, specifies that collisional terms are included only for rotational transitions within $v = 0$, where $n(i)$ is the number density of collision partners (i = H, H_2, and H^+) and $q_i(J, J')$ is the collisional rate coefficient for transitions $J \rightarrow J'$. The adopted cross sections and rates for collisional processes are discussed in vDB. The collisional de-excitation rates of H_2 by H used in this work were based on the results of Green and Truhlar (1979). Collisions of H_2 with H or H_2 result in $\Delta J = J' - J'' = \pm 2$ transitions. Only reactive collisions of H_2 with species such as H^+ allow $\Delta J = \pm 1$ transitions and can thus affect the ortho/para H_2 ratio. A cosmic-ray ionizing frequency $\zeta_0 = 5 \times 10^{-17}$ s^{-1} has been assumed in all the models discussed in the present work.

The specific molecule formation rate coefficient k_{vJ}^{φ} has been evaluated for three different models of the H_2 formation process, in order to determine the sensitivity of the H_2 populations to their initial distribution upon formation. In formation model $\varphi = 1$ it is assumed that one-third of the 4.5 eV binding energy of H_2 is deposited statistically as internal excitation of the newly formed molecule,

$$k_{vJ}^{\varphi=1} \propto g_N(2J + 1)\exp\left[-E(v, J)/12{,}098\right]\,, \quad (2)$$

where $E(v, J)$ is the energy in inverse centimeters of level vJ referred to $E(0, 0) = 0$. The nuclear spin statistical weight has values $g_N = 1$ for even values of J and $g_N = 3$ for odd values of J. In formation model $\varphi = 2$ (Leonas and Pjarnpuu 1981), the initial population distribution is given by

$$k_{vJ}^{\varphi=2} \propto \begin{cases} g_N/4\,, & v = 14\,, \quad J = 0, 1\,, \\ 0\,, & v \neq 14\,. \end{cases} \quad (3)$$

Formation model $\varphi = 3$ is suggested by a recent treatment of the H_2 catalysis process (Duley and Williams 1986) in which newly formed molecules appear with an amount of vibrational excitation comparable in energy to the difference between the binding energy of the molecule and the depth of a potential well on an amorphous silicate surface (i.e., $v \leq 7$). The rotational excitation is predicted to be low ($J \leq 1$), which we take to mean that the initial J-distribution can be described by a thermal distribution at an effective formation temperature $T_f \approx T_{\rm grain}$. Thus we assume that all molecules are initially formed in level ($v = 6$, J), and

$$k_{vJ}^{\varphi=3} \propto \begin{cases} g_N(2J + 1)\exp\left[-E(6, J)/kT_f\right]\,, & v = 6\,, \\ 0\,, & v \neq 6\,. \end{cases} \quad (4)$$

In steady state, the total rates of formation and destruction are in balance:

$$n(H_2)(\bar{k}^d + 1.051\zeta_0) = \sum_v \sum_J n_{vJ}(k_{vJ}^d + 1.051\zeta_0) \approx n_{\rm H}\, n({\rm H}) \sum_v \sum_J k_{vJ}^{\varphi}\,, \quad (5)$$

where $n_{\rm H} = n({\rm H}) + 2n(H_2)$ and $n(H_2) = \sum_v \sum_J n_{vJ}$. In practice we find that the total dissociation rate, $\bar{k}^d = (\sum_v \sum_J n_{vJ} k_{vJ}^d)/n(H_2)$, is a fraction 0.1–0.2 of the similarly defined total fluorescent excitation rate; therefore, the formation process contributes to excitation at a corresponding level. If the formation process preferentially populates levels different from those that dominate the fluorescent excitation (as in formation models $\varphi = 2$ and $\varphi = 3$), then the formation mechanism can have a significant effect on the populations of those specific levels. The total H_2 formation rate is

$$k^f = n_{\rm H}\, n({\rm H}) \sum_v \sum_J k_{vJ}^{\varphi}$$
$$= 3 \times 10^{-18} T^{1/2} y_f\, n_{\rm H}\, n({\rm H})\ {\rm cm^{-3}\ s^{-1}}\,, \quad (6)$$

where y_f is an efficiency parameter whose value has been taken to be $y_f = 3$ for most models reported here. For $y_f = 3$, the formation rate is somewhat larger than Jura's (1974) value when $T > 11$ K. In more detail, the value of y_f is expected to depend on grain temperature, gas temperature, and grain composition in a complicated fashion (cf. Hollenbach and McKee 1979; Burke and Hollenbach 1983). Specifically, when $T \gtrsim 300$ K or the grain temperature exceeds 100 K, the value of y_f is expected to be significantly reduced.

Two additional destruction processes must be considered when the ultraviolet flux is high enough to maintain significant populations of H_2 in levels with $v \geq 3$. When $v \geq 4$, H_2 can be ionized at a rate $\bar{k}^{\rm pi}$ (defined similarly to $\bar{k}^d$) by photons with $\lambda > 911.7$ Å, the Lyman limit of H. When $v \geq 3$, continuous photodissociation of H_2 is possible at $\lambda > 911.7$ Å. Cross sections for the first process have been published by Ford, Docken, and Dalgarno (1975), whereas those for the second process have been reported by Allison and Dalgarno (1969) and Glass-Maujean (1986). The model computations show that neither process contributes more than 11% to the overall destruction rate of H_2 at any depth. The photoionization process, $H_2(v \geq 4) + h\nu \rightarrow H_2^+(v') + e$, is, however, an important source of ionization of hydrogen in the outer layers of an interstellar cloud. In the intense boundary radiation field, the product $H_2^+(v')$ ions are rapidly photodissociated to form H and H^+. Since the H^+ ions affect the relative H_2 level populations through the proton interchange reaction, photoionization of H_2 must be included in cloud models for that reason. The rates of formation of $H_2^+(v')$ and the rates of its destruction by various processes are state-specific. Accordingly, a treatment of the steady state populations of H_2^+ in vibrational states $v = 0$–15 has been added to the present model calculations and will be discussed in more detail in Paper II.

The computation of a complete cloud model is complicated by the severe depth dependences of the ultraviolet line absorption rates, which govern both the total abundance (through the dissociation process) and the vibrational excitation (through fluorescent excitation) (Hollenbach, Werner, and Salpeter 1971; Black and Dalgarno 1977; Federman, Glassgold, and Kwan 1979). As in vDB, we assume that the contributions of line attenuation and grain extinction to the total opacity are separable. The continuum attenuation function depends on the scattering properties of the grains, which are still uncertain at ultraviolet wavelengths. Most calculations in this paper employ grain model 2 (cf. Roberge, Dalgarno, and Flannery 1981), which has an albedo $\omega \approx 0.6$ and an asymmetry parameter $g \approx 0.5$ at $\lambda \approx 1000$ Å. In practice, the continuum attenuation function has been represented by a wavelength-dependent function that varies as $\exp(-s_\lambda \tau_V)$ for large τ_V, where $s_\lambda \approx 3$ for grain model 2 at 1000 Å. Although grain model 2 is favored by several recent studies of grain scattering properties (Chlewicki and Greenberg 1984*a*, *b*; Draine and Lee 1984), some additional calculations were performed with the more forward-scattering grain model 3, which has $\omega \approx 0.8$ and $g = 1$ at $\lambda \approx 1000$ Å, corresponding to $s_{1000} \approx 0.8$.

The treatment of radiative transfer in the lines of the Lyman and Werner systems is the same as in vDB, except that more levels and lines are taken into account here. In that work on diffuse interstellar clouds exposed to ultraviolet radiation of relatively low intensity, the ultraviolet fluorescence of H_2 could be safely ignored as a contribution to the source function. In the limit of weak radiation fields, where ultraviolet absorption rates satisfy

$$k_{vJ}^{d} + k_{vJ}^{\mathrm{ex}} \ll A_{vJ} , \tag{7}$$

a molecule in level vJ is more likely to decay to a ground level $v = 0$, J than to absorb another ultraviolet photon, so that absorptions out of vibrationally excited levels can be neglected. Thus most of the ultraviolet fluorescence lines in H_2, which emerge at wavelengths longer than the 1225.5 Å threshold for Lyman system lines arising in $v'' = 0$, $J'' \leq 15$, will not contribute to the further excitation of H_2. Although this approximation to the source function in the transfer equation is less well justified in the present work where inequality (7) no longer holds, it has been retained for reasons of computational expediency. Absorption out of all bound levels with $v = 0$–14, $J \leq 15$ is, however, included here. Neglect of the diffuse ultraviolet fluorescence radiation is qualitatively similar to underestimating the albedo and forward-scattering component of the dust particles that partly control the penetration of external ultraviolet radiation. The magnitude of the effect of the diffuse ultraviolet radiation is expected to be at worst comparable to the effect of the uncertainty in the ultraviolet scattering properties of the grains. For normal gas-to-dust ratios, the additional opacity due to line overlap is negligible (Roberge 1981; Sternberg 1986).

In contrast to the models of vDB, in which both sides of a thin, plane-parallel cloud were exposed to external ultraviolet radiation, the current models were computed with one-sided radiation fields. This is more appropriate for the case of illumination by a single nearby star (as in a reflection nebula) and has the added virtue of eliminating a time-consuming iteration on the entire depth structure of the cloud. The wavelength dependence of the incident ultraviolet radiation is that of Draine (1978)[2] for wavelengths $\lambda < 2000$ Å and that of van Dishoeck and Black (1982) for $\lambda \geq 2000$ Å. The absolute intensity of the boundary radiation field is characterized by a scaling factor I_{UV} such that $\phi(\lambda = 1000\ \text{Å}) = 4.5 \times 10^{-8}$ photons cm^{-2} s^{-1} Hz^{-1} when $I_{\mathrm{UV}} = 1$, a value typical of the mean starlight background in the solar neighborhood. The corresponding radiation density at $\lambda = 1000$ Å is $u_\lambda = 8.94 \times 10^{-17}\, I_{\mathrm{UV}}$ ergs cm^{-3} Å^{-1}. It is assumed that no photons are present with wavelengths $\lambda \leq 912$ Å. Note that at the relevant wavelengths for H_2 excitation, $\lambda = 912$–1100 Å, the adopted radiation field is a factor of 2 more intense than the radiation fields given by Habing (1968), Black and Dalgarno (1977), or Mathis, Mezger, and Panagia (1983).

Even with the neglect of the diffuse fluorescent contribution to the source function, the equation of transfer must be solved for 22,445 absorption lines simultaneously with the equations of statistical equilibrium that describe the populations of 211 levels of $X\,^1\Sigma_g^+$ and up to 629 levels of the $B\,^1\Sigma_u^+$ ($v = 0$–36, $J \leq 16$) and 476 levels of the $C\,^1\Pi_u$ ($v = 0$–13, $J \leq 16$) states. The cascade through levels of the $X\,^1\Sigma_g^+$ state by 2937 vibration-rotation transitions is evaluated explicitly at each depth step into a model cloud. Most models reported in this paper employed 25 or 49 depth steps, depending on the parameters. The limited number of depth steps introduces an uncertainty in the $X\,^1\Sigma_g^+ v \geq 1$ column densities up to 15%–20%. The uncertainty in the relative populations of the various vJ levels is much less, however.

Fluorescent excitation of H_2 can have two observable consequences. The first is the nonthermal rotation and vibrational population distributions that are measurable by means of ultraviolet absorption lines superposed on the spectra of early-type stars (Jura 1975*a*, *b*; Black and Dalgarno 1976, 1977; vDB). The second observable consequence pertains to the interstellar molecular regions considered in this work, which are exposed to sufficiently high ultraviolet fluxes that the quadrupole vibration-rotation lines

---

[2] After this work was finished, we discovered that discrepant versions of the Draine (1978) radiation field exist in the literature. The formula for the wavelength dependence of the background intensity adopted here and by vDB,

$$\phi_v = 1.08 \times 10^{-3}\lambda^{-1} - 1.71\lambda^{-2} + 675\lambda^{-3}\ \mathrm{s^{-1}\ cm^{-2}\ Hz^{-1}} ,$$

is based upon that given by Roberge, Dalgarno, and Flannery (1981) and attributed by them to Draine (1978). Owing to an incautious truncation of coefficients following conversion of units, this formula yields values that differ significantly (larger by factors of 2.3 and 1.3 at $\lambda = 912$ and 1000 Å, respectively) from those obtained with Draine's original formula,

$$\phi_v = 1.068350 \times 10^{-3}\lambda^{-1} - 1.719258\lambda^{-2} + 685.3491\lambda^{-3}\ \mathrm{s^{-1}\ cm^{-2}\ Hz^{-1}} .$$

of H_2 in the infrared become detectable. In either case, it is the column density of H_2 in an excited level, $N_{vJ} = \int n_{vJ}(z)dz$, that is directly related to an observable quantity such as the equivalent width of an absorption line or the intensity of an emission line. In the models presented here, the specific intensity of each infrared emission line is computed:

$$I_{v'J',v''J''} = \frac{hc\tilde{\nu}}{4\pi} N_{v'J'} A_{v'J',v''J''} \text{ ergs s}^{-1}\text{ cm}^{-2}\text{ sr}^{-1} , \tag{8}$$

where $\tilde{\nu} = \nu/c$ is the transition frequency in inverse centimeters. These forbidden transitions in H_2 are so intrinsically weak that self-absorption in a line can be ignored.

The H_2 infrared line positions have been calculated from accurate molecular constants, except for a few cases where more accurate directly measured values are available. For $v = 0$, the rotational constants of Jennings, Rahn, and Owyoung (1985) have been adopted. For $v = 1$ and $v = 2$, rotational constants have been computed from the best available term energies, which derive from the accurate $v = 0$ energies in combination with the spectroscopic data of Bragg, Brault, and Smith (1982) for $J \leq 5$ and of Dabrowski (1984) for higher J. For $v = 3$, rotational constants have been computed from fits to the spectroscopic data quoted by Fink, Wiggins, and Rank (1965) and Dabrowski (1984). For the higher states of $X\,^1\Sigma_g^+$, $v \geq 4$, the constants of Dabrowski (1984) have been adopted.

III. RESULTS

a) Basic Properties and Calculated Spectra

A cloud model as described above consists of densities, level populations, and other physical attributes specified as functions of depth from an irradiated boundary to a designated center. Although models with gradients in density and temperature can be computed, most of the models discussed here are uniform. A particular model is characterized by values of total density n_H, temperature T, incident ultraviolet flux in terms of I_{UV}, total thickness described by the visual extinction A_V or the total H_2 column density $N(H_2)$, and the width of H_2 absorption lines given by the value of the Doppler parameter b. Three properties of interstellar grains are retained as disposable parameters: (1) the H_2 formation model (eqs. [2]–[4]), (2) the ultraviolet scattering properties and extinction curve, and (3) the overall H_2 formation efficiency (eq. [6]). Unless otherwise specified, models discussed below have $b = 4.0$ km s^{-1} and $y_f = 3$ and use grain model 2 of Roberge, Dalgarno, and Flannery (1981) for the extinction curve and scattering properties. The value of b is consistent with that typically measured for H_2 lines in diffuse interstellar clouds (Spitzer, Cochran, and Hirshfeld 1974) and, coincidentally, is equal to the thermal Doppler width at $T = 2000$ K that might characterize the intrinsic line width which enters the computation of the emission spectrum of shock-heated gas (see § III*g*, below).

In Figure 1 the depth dependences of several properties within a cloud are displayed. The total molecular density, $n(H_2)$, increases steadily with depth until it accounts for virtually all of the hydrogen. On such a linear depth scale, the transition from mostly atomic to mostly molecular composition is quite sharp. The sudden transition is due to self-shielding in the ultraviolet absorption lines which causes the absorption rates, $k_{vJ}^{ex} + k_{vJ}^{d}$, to decrease rapidly with increasing depth as soon as the predominant lines arising in vJ become optically thick. The line-center optical depth is

$$\tau_{v'J',v''J''} \approx \frac{N_{v''J''} \int \sigma_\nu d\nu}{\Delta\nu} = 1.06\left(\frac{N_{v''J''}}{2 \times 10^{14}}\right)\left(\frac{f}{0.01}\right)\left(\frac{\lambda}{1000}\right)\left(\frac{3}{b}\right) \tag{9}$$

for an ultraviolet absorption line $v'J' \leftarrow v''J''$, at a wavelength $\lambda = 10^8 c/\nu$ Å, that has an oscillator strength f, an absorption cross section σ_ν, a full width at half-maximum $\Delta\nu$ in hertz, and a corresponding Doppler broadening parameter b in kilometers per second. For a typical ultraviolet absorption line, self-shielding thus starts to become important at H_2 column densities of a few times 10^{14} cm^{-2}. The depth dependence of the dissociation rate $\bar{k}^d$ is included in Figure 1. As expected, it looks like a reflection of the $n(H_2)$ curve in the outer layers. As a consequence, the product $n(H_2)\bar{k}^d$ remains approximately constant until most of the hydrogen is molecular. Because the fluorescent excitation rates vary with depth as $\bar{k}^d$, the concentration of vibrationally excited H_2,

$$n(H_2^*) = \sum_{v \geq 1} \sum_{J} n_{vJ}(H_2) , \tag{10}$$

also remains nearly constant through the outer layers. This excited molecule density approaches a nonzero, asymptotic value in the limit $\bar{k}^d \ll \zeta_0$, where H_2 formation on grain surfaces is in balance with destruction by cosmic rays. In this limit, ultraviolet excitation is negligible, and the only contribution to the vibrationally excited population is from the formation process. For formation model $\varphi = 1$, the asymptotic value is $n(H_2^*) \approx 8.9 \times 10^{-11} n(H_2)$. The total column density $N(H_2) = 10^{22}$ cm^{-2} in the models is chosen such that this asymptotic limit is reached.

The basic properties of a set of cloud models are summarized in Table 1. The total intensity,

$$I_{\text{total}} = \sum_{v'} \sum_{J'} \sum_{v} \sum_{J} I_{v'J',vJ} \text{ ergs s}^{-1}\text{ cm}^{-2}\text{ sr}^{-1} , \tag{11}$$

sums over all vibration-rotation transitions except for the (0, 0) $S(0)$ and $S(1)$ pure rotational lines, which are excited predominantly by collisions rather than by fluorescence. Table 1 also includes the total column density of excited H_2 defined by

$$N(H_2^*) = \sum_{v \geq 1} \sum_{J} N_{vJ}(H_2) \text{ cm}^{-2} , \tag{12}$$

as well as the maximum value of the excited H_2 density in the models. In the adopted radiation field, the integrated intensity of ultraviolet light over the wavelength interval $\lambda = 912$–1130 Å is $4.76 \times 10^{-5} I_{UV}$ ergs s^{-1} cm^{-2} sr^{-1}. This can be used to define a

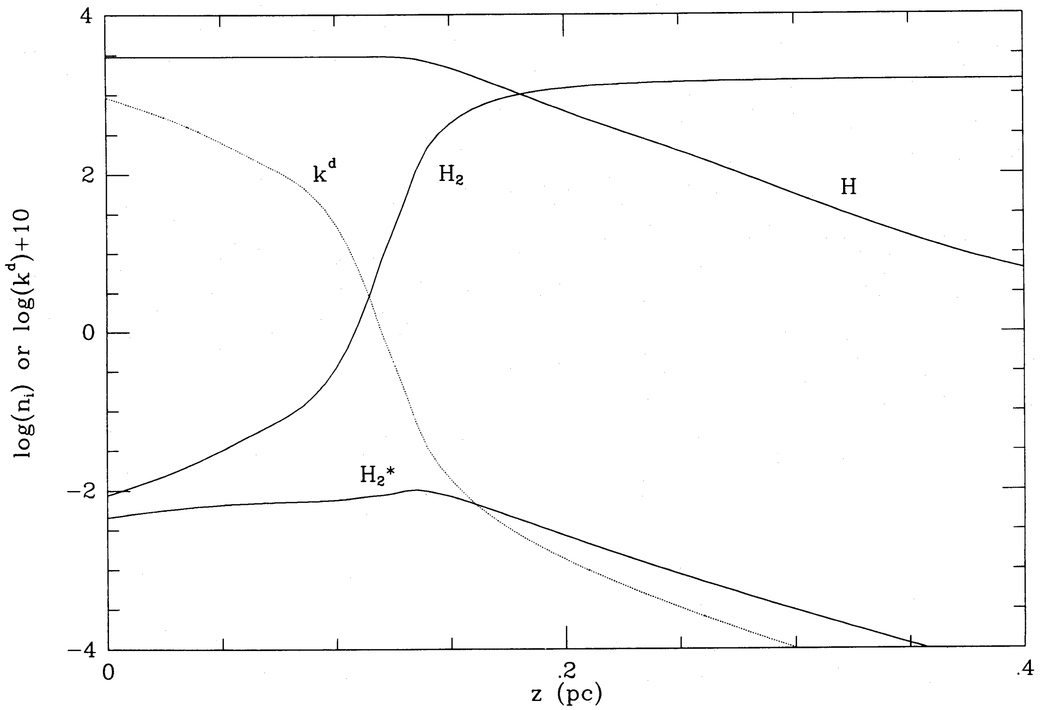

FIG. 1.—Depth dependences of hydrogen abundances. The solid curves show the variations of the H, H_2, and H_2^* number densities (cm^{-3}) with increasing linear depth from the cloud boundary at $z = 0$. The dotted curve shows the variation in the H_2 dissociation rate (s^{-1}). These results refer to reference model 14 of Table 1.

fluorescence efficiency for H_2, $\epsilon = 2.10 \times 10^4 I_{\rm total}/I_{\rm UV}$, which is the ratio of the infrared fluorescent intensity to the integrated intensity of ultraviolet light that is effective in exciting H_2. The values of ϵ are listed in Table 1 for each model.

Calculated infrared line spectra can be presented in several ways. Table 2 contains a selection of the strongest vibration-rotation line intensities for the models of Table 1. These intensities are presented as percentages of the total fluorescent intensity, viz., $100 I_{v'J',v''J''}/I_{\rm total}$. The strongest individual lines account for 1%–2% of the total line intensity. For $T = 100$ K the summed intensity in the (0, 0) $S(0)$ and $S(1)$ lines is 2.9×10^{-5} ergs s^{-1} cm^{-2} sr^{-1}. At $T = 30$ K this intensity has dropped to only 2.2×10^{-6} ergs s^{-1} cm^{-2} sr^{-1}, whereas for $T = 300$ K it is as much as 3.1×10^{-3} ergs s^{-1} cm^{-2} sr^{-1}. Because of the large number of infrared H_2 transitions, the lines may be blended in spectra of low resolution. Simulated model spectra at the low resolution $R = \lambda/\Delta\lambda = 100$ commonly used in observations have been constructed to illustrate these effects. All H_2 lines with $J' \leq 15$ have been included in the calculations, and have been assumed to have intrinsic widths like those of the ultraviolet absorption lines ($b = 4.0$ km s^{-1}). They have been convolved with a Gaussian function to represent a spectrometer resolution of $\Delta\lambda = 0.02$ μm between 2 and 2.5 μm, and $\Delta\lambda = 0.015$ μm between 1 and 2 μm. In Figure 2 the simulated spectra for our reference model, model 14, are presented in the wavelength intervals 2–2.5 μm and 1–2 μm. The line identifications for the most prominent features are included in the figure, whereas the line positions of the most important transitions are indicated at the bottom of the figure. The 2–2.5 μm region contains primarily $\Delta v = v' - v'' = 1$ transitions, whereas $\Delta v = 2$ transitions occur between 1 and 2 μm. Table 3 contains the positions and identifications of the stronger fluorescent lines computed for this model. All lines with intensities $100 I/I_{\rm total} \geq 0.05$—about 400 in number out of the total 2937 H_2 vibration-rotation lines with $J \leq 15$—are listed. As indicated in § II, the wavelengths in Table 3 derive from the best available spectroscopic data; therefore, this table can be used as a finding list of H_2 lines. The effect of resolution on the appearance of the spectrum is illustrated in Figure 3 for the reference model 14: it is obvious that many lines may contribute to a feature at low resolution. For example, weak lines within ± 0.021 μm of the strong (1, 0) $S(1)$ line at $\lambda = 2.121$ μm contribute 25% of the intensity of that one feature. At low resolution, $\lambda/\Delta\lambda < 260$, a feature at $\lambda = 2.07$ μm that would usually be attributed to the (2, 1) $S(3)$ line is actually a blend of four lines: the three weaker lines contribute more than 30% of the intensity of the unresolved blend. Blending of the (1, 0) $S(2)$ line at $\lambda = 2.03$ μm with two weaker lines may increase the intensity ascribed to that transition alone by 40%. As is evident from Table 3 and Figure 3, the problem of blending at low resolution is even more severe at shorter wavelengths, $\lambda = 1.0$–1.8 μm: indeed, few features can be identified primarily with single lines, and most features appear to sit atop a large pseudocontinuum formed by a multitude of weaker lines. Figure 4 illustrates the fluorescent spectrum of model 14 at low resolution at longer wavelengths.

Tables 1 and 2 contain the model results for a range of densities, temperatures, intensities and other parameters. In the following, the effects of each of these parameters on the *total* infrared intensity as well as on the *relative* intensities will be discussed.

b) *Effects of Density and Intensity of the Radiation Field*

It is obvious from Table 1 that the total H_2 infrared line intensity $I_{\rm total}$ depends strongly on the density $n_{\rm H}$ in the cloud and the total intensity of the ultraviolet radiation field incident on the cloud. These trends are illustrated in Figure 5, where $I_{\rm total}$ is shown as a function of the scaling factor for the radiation field $I_{\rm UV}$ for various densities $n_{\rm H}$. For a given density, $I_{\rm total}$ initially increases almost

TABLE 1

PROPERTIES OF CLOUD MODELS

Model	n_H (cm^{-3})	T (K)	I_{UV}	A_V (mag)	N(H) (cm^{-2})	$N(H_2^*)$ (cm^{-2})	$n_{max}(H_2^*)$ (cm^{-3})	I_{total} (erg s^{-1} cm^{-2} sr^{-1})	$I[(1,0)S(1)]$ (erg s^{-1} cm^{-2} sr^{-1})	ε	Notes
1	1.0(2)	100	1(0)	12.75	3.1(20)	2.8(13)	1.4(-5)	4.25(-6)	7.82(-8)	8.9(-2)	a
2	1.0(2)	100	3(1)	13.57	1.6(21)	1.9(14)	1.3(-5)	2.91(-5)	5.40(-7)	2.0(-2)	
3	1.0(2)	100	1(2)	13.95	2.2(21)	2.8(14)	1.2(-5)	4.22(-5)	8.00(-7)	8.9(-3)	
4	1.0(2)	100	1(3)	14.69	3.4(21)	4.1(14)	1.7(-5)	6.40(-5)	1.13(-6)	1.4(-3)	
5	1.0(2)	100	1(4)	15.44	4.7(21)	4.4(14)	2.1(-5)	7.01(-5)	1.21(-6)	1.5(-4)	
6	1.0(3)	100	1(0)	12.60	3.7(19)	3.4(13)	1.4(-3)	5.18(-6)	9.48(-8)	1.1(-1)	
7	1.0(3)	100	3(1)	12.93	5.7(20)	6.7(14)	1.3(-3)	1.01(-4)	1.78(-6)	7.1(-2)	
8	1.0(3)	100	1(2)	13.24	1.1(21)	1.2(15)	1.2(-3)	1.89(-4)	3.30(-6)	4.0(-2)	
9	1.0(3)	100	1(3)	13.98	2.3(21)	2.3(15)	1.3(-3)	3.64(-4)	5.87(-6)	7.7(-3)	
10	1.0(3)	100	1(4)	14.74	3.5(21)	2.4(15)	1.5(-3)	3.90(-4)	5.90(-6)	8.2(-4)	
11	3.0(3)	100	1(0)	12.59	1.4(19)	3.5(13)	1.2(-2)	5.26(-6)	9.67(-8)	1.1(-1)	
12	3.0(3)	100	1(1)	12.64	1.0(20)	3.4(14)	1.2(-2)	5.16(-5)	9.40(-7)	1.1(-1)	
13	3.0(3)	100	1(2)	12.98	6.5(20)	2.2(15)	1.1(-2)	3.33(-4)	5.78(-6)	7.0(-2)	
14	3.0(3)	100	1(3)	13.66	1.7(21)	4.7(15)	9.6(-3)	7.67(-4)	1.23(-5)	1.6(-2)	
15	3.0(3)	100	1(4)	14.44	3.0(21)	4.9(15)	1.1(-2)	8.32(-4)	1.23(-5)	1.8(-3)	
16	1.0(4)	100	1(0)	12.58	4.3(18)	3.4(13)	1.3(-1)	5.16(-6)	9.68(-8)	1.1(-1)	
17	1.0(4)	100	3(1)	12.63	9.7(19)	1.1(15)	1.3(-1)	1.59(-4)	2.86(-6)	1.1(-1)	
18	1.0(4)	100	1(2)	12.75	2.8(20)	3.0(15)	1.2(-1)	4.65(-4)	8.07(-6)	9.8(-2)	
19	1.0(4)	100	1(3)	13.33	1.2(21)	9.8(15)	8.5(-2)	1.60(-3)	2.52(-5)	3.4(-2)	
20	1.0(4)	100	1(4)	14.13	2.5(21)	1.1(16)	9.2(-2)	1.84(-3)	2.57(-5)	3.9(-3)	
21	3.0(4)	100	1(0)	12.58	1.4(18)	3.4(13)	1.1(0)	5.16(-6)	9.71(-8)	1.1(-1)	
22	3.0(4)	100	1(1)	12.58	1.3(19)	3.4(14)	1.2(0)	5.21(-5)	9.91(-7)	1.1(-1)	
23	3.0(4)	100	1(2)	12.64	1.2(20)	3.5(15)	1.1(0)	5.36(-4)	9.37(-6)	1.1(-1)	
24	3.0(4)	100	1(3)	13.06	7.9(20)	1.7(16)	6.4(-1)	2.81(-3)	4.22(-5)	5.9(-2)	
25	3.0(4)	100	1(4)	13.86	2.1(21)	2.1(16)	6.6(-1)	3.61(-3)	4.68(-5)	7.6(-3)	
26	3.0(3)	30	1(3)	13.80	2.0(21)	3.0(15)	5.8(-3)	4.92(-4)	6.81(-6)	1.0(-2)	
27	3.0(3)	300	1(3)	13.54	1.6(21)	7.1(15)	1.5(-2)	1.78(-3)	1.99(-5)	3.7(-2)	
28	3.0(3)	100	1(3)	15.78	5.1(21)	1.3(16)	8.4(-3)	2.17(-3)	3.59(-5)	4.6(-2)	b
29	3.0(3)	100	1(3)	15.80	5.1(21)	1.3(16)	8.3(-3)	2.12(-3)	3.47(-5)	4.5(-2)	c
30	3.0(3)	100	1(3)	13.66	1.7(21)	4.7(15)	1.1(-2)	7.79(-4)	1.27(-5)	1.6(-2)	d
31	3.0(3)	100	1(3)	13.67	1.8(21)	4.9(15)	1.0(-2)	8.10(-4)	9.43(-6)	1.7(-2)	e
32	3.0(3)	100	1(3)	13.64	1.7(21)	4.8(15)	1.0(-2)	7.93(-4)	1.28(-5)	1.7(-2)	f
33	3.0(3)	100	1(3)	13.61	1.7(21)	4.7(15)	9.4(-3)	7.46(-4)	1.22(-5)	1.6(-2)	g
34	3.0(3)	100	1(3)	2.32	1.7(21)	4.5(15)	1.0(-2)	7.40(-4)	1.13(-5)	1.6(-2)	h
35	3.0(3)	100	1(3)	3.99	5.5(21)	1.4(16)	8.7(-3)	2.28(-3)	3.60(-5)	4.8(-2)	i
36	3.0(3)	100	1(3)	4.38	8.0(21)	5.8(15)	2.7(-3)	9.32(-4)	1.49(-5)	2.0(-2)	j
37	3.0(3)	100	1(3)	2.24	3.4(22)	7.0(15)	7.6(-4)	1.11(-3)	1.83(-5)	2.3(-2)	k
S1		1000				1.5(15)		1.25(-4)	1.23(-5)		l
S2		2000				2.0(15)		1.45(-4)	1.23(-5)		m

NOTE.—In this and subsequent tables, the notation 1.0(20) means 1.0×10^{20}.

[a] All of models 1–37 were computed with grain model 2, formation model $\varphi = 1$, $N(H_2) = 1.0 \times 10^{22}$ cm^{-2}, $b = 4.0$ km s^{-1}, $y_f = 3.0$, and $\alpha = 0.0$, unless otherwise indicated.

[b] Grain model 3.

[c] Grain model 3 and $\alpha = 1.0$.

[d] Formation model $\varphi = 2$.

[e] Formation model $\varphi = 3$ and $T_f = 15$ K.

[f] Formation model $\varphi = 3$ and $T_f = 65$ K.

[g] $b = 1$ km s^{-1}.

[h] $N(H_2) = 1.0 \times 10^{21}$ cm^{-2}.

[i] Gas/extinction ratio is 4 times normal.

[j] Gas/extinction ratio is 4 times normal, and $y_f = 0.75$.

[k] Gas/extinction ratio is 15 times normal, and $y_f = 0.20$.

[l] $N(H_2) = 5.811 \times 10^{17}$ cm^{-2}.

[m] $N(H_2) = 3.804 \times 10^{16}$ cm^{-2}.

linearly with increasing I_{UV}, but eventually stops increasing and approaches an asymptotic value. This limit to fluorescent emission and the sensitivity to density result from the competition (averaged over depth) between grains and molecules for exciting photons in the ultraviolet and can be illustrated as follows:

The unshielded dissociation rate of H_2 in a one-sided radiation field is

$$\bar{k}^d = 7.5 \times 10^{-11} I_{UV} \text{ s}^{-1} , \tag{13}$$

hence, in steady state in the boundary layer of a cloud where $n(H_2) \ll n(H) \approx n_H$,

$$\frac{N(H_2)}{N_H} \approx \frac{n(H_2)}{n_H} \approx 1.2 \times 10^{-6} \left(\frac{T}{100}\right)^{1/2} \left(\frac{y_f}{3}\right) \frac{n_H}{I_{UV}} . \tag{14}$$

The onset of self-shielding can be said to occur when $\tau_{v'J',v''J''} \approx 1$ for a typical line. If, for example, this typical line has $v'' = 0$, $J'' = 1$, $\lambda = 1000$ Å, and $f = 0.01$, then for $N_{01} \approx 0.5N(H_2)$ the depth at which self-shielding begins can be expressed in terms of a

TABLE 2

Intensities of Selected Strong Fluorescent Lines of H_2

Band	(0,0)	(0,0)	(0,0)	(0,0)	(3,2)	(2,1)	(1,0)	(2,1)	(1,0)	(1,0)	(1,0)	(1,0)	(1,0)	(1,0)	(3,2)	(2,1)	(4,3)	(2,1)	(1,0)	(3,2)
Line	S(2)	S(3)	S(5)	S(9)	O(3)	O(3)	O(3)	O(2)	O(2)	Q(5)	Q(4)	Q(3)	Q(2)	Q(1)	S(1)	S(0)	S(3)	S(1)	S(0)	S(3)
$\lambda(\mu m)^a$	12.275	9.662	6.908	4.693	3.163	2.973	2.802	2.785	2.626	2.454	2.437	2.423	2.413	2.406	2.386	2.355	2.344	2.247	2.223	2.201
Model	Intensity:		$100I/I_{total}$																	
1	0.61	0.99	0.68	0.52	0.59	1.03	1.78	0.66	1.12	0.45	0.51	1.29	1.16	2.11	0.49	0.57	0.08	0.96	1.05	0.18
2	0.45	0.75	0.56	0.26	0.54	0.96	1.66	0.60	1.03	0.51	0.55	1.30	1.13	1.97	0.50	0.56	0.10	0.97	1.02	0.23
4	0.27	0.43	0.35	0.20	0.48	0.86	1.45	0.47	0.79	0.56	0.50	1.24	0.92	1.72	0.51	0.47	0.13	0.97	0.83	0.29
6	0.68	0.94	0.66	0.31	0.59	1.03	1.78	0.66	1.12	0.45	0.52	1.29	1.17	2.10	0.48	0.58	0.08	0.95	1.06	0.18
7	0.48	0.76	0.54	0.26	0.54	0.96	1.65	0.66	1.11	0.46	0.56	1.24	1.19	1.95	0.47	0.60	0.09	0.93	1.08	0.20
9	0.25	0.41	0.31	0.22	0.46	0.80	1.33	0.45	0.75	0.52	0.48	1.13	0.87	1.58	0.48	0.45	0.13	0.90	0.78	0.29
11	0.79	0.87	0.65	0.31	0.59	1.03	1.78	0.66	1.12	0.45	0.52	1.29	1.17	2.10	0.49	0.58	0.08	0.96	1.06	0.18
12	0.45	0.77	0.56	0.27	0.58	1.01	1.75	0.67	1.13	0.45	0.54	1.28	1.19	2.07	0.49	0.59	0.08	0.95	1.08	0.19
14	0.21	0.43	0.31	0.22	0.46	0.81	1.34	0.43	0.71	0.51	0.45	1.12	0.81	1.59	0.47	0.42	0.13	0.89	0.73	0.28
15	0.20	0.38	0.27	0.21	0.42	0.73	1.23	0.40	0.66	0.48	0.43	1.03	0.77	1.45	0.44	0.40	0.13	0.82	0.69	0.27
17	0.27	0.61	0.50	0.27	0.57	1.00	1.72	0.65	1.10	0.46	0.53	1.27	1.16	2.03	0.48	0.58	0.08	0.95	1.05	0.20
19	0.15	0.44	0.33	0.23	0.46	0.81	1.35	0.44	0.71	0.50	0.44	1.11	0.81	1.60	0.46	0.42	0.12	0.87	0.73	0.27
20	0.25	0.36	0.28	0.22	0.40	0.70	1.17	0.38	0.62	0.47	0.40	0.98	0.72	1.38	0.41	0.37	0.13	0.78	0.65	0.27
26	0.26	0.35	0.30	0.22	0.38	0.67	1.10	0.56	0.92	0.48	0.53	0.97	1.03	1.30	0.42	0.53	0.13	0.78	0.93	0.27
27	26.7	8.74	0.22	0.15	0.31	0.55	0.92	0.23	0.38	0.35	0.27	0.79	0.47	1.09	0.33	0.24	0.09	0.62	0.42	0.19
28	0.27	0.57	0.38	0.23	0.50	0.87	1.47	0.47	0.77	0.49	0.44	1.16	0.86	1.74	0.47	0.44	0.12	0.90	0.78	0.25
29	0.27	0.57	0.39	0.24	0.42	0.85	1.43	0.47	0.78	0.49	0.42	1.15	0.87	1.70	0.48	0.44	0.11	0.88	0.78	0.25
30	0.19	0.24	0.008	0.006	0.53	0.89	1.44	0.48	0.78	0.42	0.44	1.15	0.88	1.70	0.51	0.47	0.12	0.94	0.80	0.24
31	0.28	0.18	0.05	0.008	0.37	0.64	1.07	0.92	1.25	0.28	0.77	0.82	1.52	1.27	0.34	0.81	0.07	0.64	1.37	0.15
32	0.21	0.23	0.06	0.009	0.54	0.92	1.45	0.63	0.93	0.40	0.54	1.14	1.08	1.72	0.50	0.57	0.10	0.94	0.98	0.23
S1	1.12	8.22	11.7	0.74	2.2(-4)	4.4(-2)	8.67	1.2(-2)	2.44	2.39	1.49	6.91	2.91	10.3	2.5(-4)	1.3(-2)	7.6(-7)	4.9(-2)	2.63	1.3(-4)
S2	0.07	0.77	3.09	3.39	3.1(-2)	0.43	5.01	0.11	1.30	4.18	1.76	5.96	1.97	5.93	4.9(-2)	0.15	3.2(-3)	0.70	1.79	4.8(-2)

Band	(2,1)	(1,0)	(2,1)	(8,6)	(1,0)	(6,4)	(5,3)	(3,1)	(5,3)	(4,2)	(3,1)	(4,2)	(2,0)	(3,1)	(3,1)	(2,0)	(2,0)	(6,3)	(5,2)	(4,1)
Line	S(2)	S(1)	S(3)	O(3)	S(2)	Q(1)	Q(1)	O(3)	S(1)	Q(1)	Q(1)	S(1)	Q(1)	S(1)	S(2)	S(1)	S(2)	S(1)	S(1)	S(1)
$\lambda(\mu m)^a$	2.154	2.121	2.073	2.041	2.033	1.601	1.493	1.418[b]	1.400	1.398	1.314	1.311	1.238	1.233	1.207	1.162	1.138	0.988	0.923	0.866
Model	Intensity:		$100I/I_{total}$																	
1	0.44	1.84	0.41	0.33	0.91	0.68	0.87	0.82	0.62	1.00	1.02	0.78	0.75	0.87	0.41	0.71	0.36	0.26	0.25	0.19
2	0.49	1.86	0.49	0.29	0.98	0.61	0.78	0.75	0.64	0.91	0.93	0.80	0.70	0.89	0.46	0.72	0.39	0.27	0.26	0.19
4	0.47	1.76	0.60	0.26	0.89	0.54	0.69	0.68	0.67	0.81	0.83	0.83	0.62	0.90	0.46	0.72	0.38	0.28	0.27	0.20
6	0.45	1.83	0.41	0.33	0.93	0.68	0.86	0.82	0.62	1.00	1.01	0.78	0.75	0.86	0.42	0.70	0.37	0.26	0.25	0.19
7	0.50	1.77	0.44	0.30	1.00	0.62	0.79	0.76	0.61	0.92	0.94	0.76	0.70	0.84	0.47	0.68	0.40	0.25	0.24	0.18
9	0.46	1.61	0.58	0.25	0.85	0.52	0.67	0.64	0.64	0.78	0.79	0.79	0.58	0.85	0.46	0.67	0.37	0.27	0.25	0.19
11	0.45	1.84	0.41	0.33	0.93	0.68	0.86	0.82	0.62	1.00	1.01	0.78	0.75	0.87	0.42	0.71	0.36	0.26	0.25	0.19
12	0.48	1.82	0.42	0.32	0.97	0.67	0.85	0.81	0.62	0.98	1.00	0.78	0.74	0.86	0.45	0.70	0.38	0.26	0.25	0.19
14	0.44	1.60	0.56	0.26	0.80	0.53	0.68	0.65	0.64	0.79	0.80	0.79	0.59	0.84	0.44	0.66	0.35	0.27	0.25	0.19
15	0.42	1.47	0.54	0.24	0.77	0.49	0.62	0.58	0.60	0.72	0.72	0.73	0.53	0.78	0.43	0.61	0.34	0.26	0.24	0.18
17	0.48	1.80	0.44	0.32	0.96	0.66	0.84	0.79	0.62	0.97	0.98	0.78	0.73	0.86	0.45	0.70	0.39	0.26	0.25	0.19
19	0.43	1.58	0.54	0.26	0.78	0.54	0.69	0.65	0.62	0.79	0.80	0.76	0.59	0.82	0.43	0.64	0.34	0.26	0.25	0.18
20	0.40	1.40	0.52	0.23	0.72	0.47	0.59	0.56	0.57	0.68	0.69	0.70	0.51	0.74	0.41	0.58	0.32	0.25	0.23	0.17
26	0.52	1.38	0.54	0.21	0.96	0.44	0.56	0.54	0.56	0.65	0.66	0.69	0.49	0.74	0.51	0.58	0.42	0.24	0.23	0.17
27	0.27	1.12	0.38	0.17	0.49	0.36	0.46	0.44	0.44	0.53	0.54	0.54	0.40	0.58	0.27	0.46	0.22	0.19	0.18	0.13
28	0.42	1.66	0.51	0.28	0.80	0.58	0.73	0.69	0.63	0.85	0.86	0.78	0.63	0.84	0.42	0.67	0.34	0.27	0.25	0.19
29	0.43	1.64	0.51	0.28	0.75	0.58	0.74	0.59	0.65	0.86	0.72	0.79	0.62	0.85	0.41	0.65	0.35	0.27	0.26	0.19
30	0.44	1.63	0.48	0.36	0.80	0.69	0.84	0.73	0.74	0.93	0.91	0.88	0.65	0.92	0.45	0.69	0.36	0.33	0.30	0.21
31	0.84	1.16	0.30	0.20	1.38	0.43	0.54	0.51	0.45	0.63	0.63	0.55	0.46	0.60	0.84	0.47	0.68	0.19	0.18	0.13
32	0.57	1.62	0.46	0.25	0.97	1.45	0.74	0.75	0.66	1.04	0.93	0.98	0.67	0.90	0.57	0.69	0.46	0.25	0.27	0.24
S1	1.4(-2)	9.84	2.6(-2)	3(-13)	2.68	8(-10)	5.1(-8)	3.1(-4)	5.8(-4)	4.2(-6)	3.9(-4)	4.7(-6)	3.2(-2)	4.4(-4)	1.3(-4)	3.6(-2)	1.1(-2)	5(-10)	2.3(-8)	1.1(-6)
S2	0.26	8.49	0.71	2.2(-6)	3.18	1.1(-4)	8.7(-4)	4.3(-2)	1.4(-3)	7.0(-3)	5.3(-2)	1.1(-2)	0.31	8.7(-2)	3.5(-2)	0.52	0.21	9.8(-5)	5.4(-4)	2.7(-3)

[a] Wavelength in air.

[b] Always blended with (4, 2) *Q*(4) at $\lambda = 1.418$ μm, which is typically 0.2–0.3 times as strong as this line.

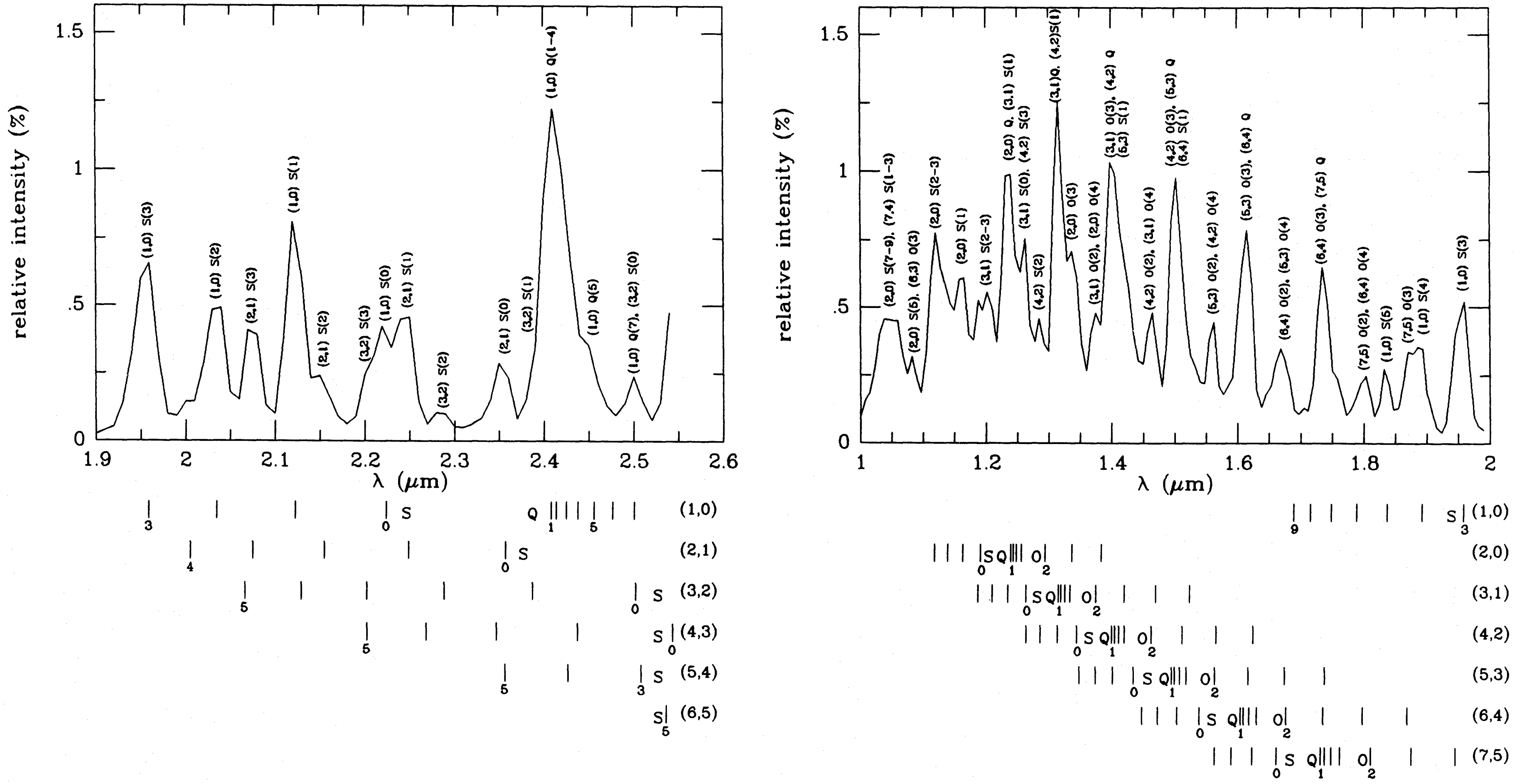

FIG. 2.—Simulated low-resolution spectra of H_2 emission in reference model 14. The model spectra have been convolved with Gaussians of width $\Delta\lambda = 0.02$ μm (*left*) and $\Delta\lambda = 0.015$ μm (*right*). Line positions in various vibration-rotation bands are indicated below each spectrum, and the major contributors to each strong feature are identified. The intensity is shown as a percentage of the total fluorescent intensity per resolution element; i.e., the intensity scale is in units $0.01 I_{\text{total}}/\Delta\lambda$, or 3.835×10^{-4} ergs s^{-1} cm^{-2} μm^{-1} sr^{-1} for the left panel and 5.113×10^{-4} ergs s^{-1} cm^{-2} μm^{-1} sr^{-1} for the right panel.

TABLE 3

STRONGEST FLUORESCENT LINES OF H_2 IN MODEL 14

$\tilde{\nu}^a$	λ^b	Transition	$100I/I_{total}$
(cm^{-1})	μm		per cent
354.37350[c]	28.21112	(0, 0) S(0)	2.35
587.03211[c]	17.03020	(0, 0) S(1)	1.48
814.42473[c]	12.275259	(0, 0) S(2)	.21
1034.67024[c]	9.6622810	(0, 0) S(3)	.43
1246.09811[c]	8.0228631	(0, 0) S(4)	.13
1447.27882[c]	6.907635	(0, 0) S(5)	.31
1637.046	6.1069	(0, 0) S(6)	.10
1720.899	5.8093	(1, 1) S(7)	.05
1814.496	5.5097	(0, 0) S(7)	.27
1978.984	5.0517	(0, 0) S(8)	.08
2018.494	4.9528	(1, 1) S(9)	.09
2130.102[d]	4.69333	(0, 0) S(9)	.22
2264.147	4.4155	(1, 1) S(11)	.09
2267.648	4.4087	(0, 0) S(10)	.06
2376.602	4.2065	(5, 4) O(5)	.06
2391.612	4.1801	(0, 0) S(11)	.15
2458.414	4.0666	(1, 1) S(13)	.05
2466.679	4.0529	(2, 1) O(7)	.08
2517.633	3.9709	(3, 2) O(6)	.06
2552.812	3.9162	(4, 3) O(5)	.12
2563.921	3.8992	(6, 5) O(3)	.07
2569.762	3.8904	(5, 4) O(4)	.06
2600.0[e]	3.8451	(0, 0) S(13)	.07
2626.460	3.8064	(1, 0) O(7)	.14
2685.504	3.7227	(2, 1) O(6)	.10
2729.822	3.6622	(3, 2) O(5)	.21
2756.803	3.6264	(4, 3) O(4)	.12
2763.565	3.6175	(5, 4) O(3)	.14
2856.483	3.4999	(1, 0) O(6)	.18
2908.775	3.4369	(2, 1) O(5)	.37
2944.738	3.3950	(3, 2) O(4)	.21
2956.311	3.3817	(5, 4) O(2)	.07
2961.679	3.3755	(4, 3) O(3)	.26
3008.130	3.3234	(6, 5) Q(1)	.07
3091.200	3.2341	(1, 0) O(5)	.63
3134.981	3.1889	(2, 1) O(4)	.37
3160.729	3.1630	(3, 2) O(3)	.46
3165.664	3.1580	(4, 3) O(2)	.14
3207.774	3.1166	(5, 4) Q(3)	.09
3224.653	3.1003	(5, 4) Q(2)	.07
3235.949	3.0894	(5, 4) Q(1)	.15
3329.040	3.0030	(1, 0) O(4)	.62
3362.408	2.9732	(2, 1) O(3)	.81
3375.974	2.9613	(3, 2) O(2)	.25
3383.984	2.9543	(4, 3) Q(5)	.08
3411.695	2.9303	(4, 3) Q(4)	.07
3434.063	2.9112	(4, 3) Q(3)	.19
3450.963	2.8970	(4, 3) Q(2)	.14
3462.292	2.8875	(4, 3) Q(1)	.29
3509.952	2.8483	(5, 4) S(0)	.06
3539.850	2.8242	(3, 2) Q(7)	.07
3568.225	2.8017	(1, 0) O(3)	1.34
3578.004	2.7941	(3, 2) Q(6)	.05
3589.170	2.7854	(2, 1) O(2)	.43
3611.073	2.7685	(3, 2) Q(5)	.16
3638.898	2.7473	(3, 2) Q(4)	.14
3661.342	2.7305	(3, 2) Q(3)	.36
3676.336	2.7194	(2, 1) Q(9)	.07
3678.285	2.7179	(3, 2) Q(2)	.27
3680.158	2.7165	(5, 4) S(1)	.11
3689.635	2.7096	(3, 2) Q(1)	.53
3753.274	2.6636	(4, 3) S(0)	.12
3768.134	2.6531	(2, 1) Q(7)	.13
3794.871	2.6344	(1, 0) Q(11)	.07
3806.770	2.6262	(2, 1) Q(6)	.10
3806.800	2.6262	(1, 0) O(2)	.71
3840.294	2.6033	(2, 1) Q(5)	.29
3868.528	2.5843	(2, 1) Q(4)	.26
3891.314	2.5691	(2, 1) Q(3)	.65
3906.478	2.5592	(1, 0) Q(9)	.14
3908.523	2.5578	(2, 1) Q(2)	.48
3920.053	2.5503	(2, 1) Q(1)	.94
3934.676	2.5408	(4, 3) S(1)	.24
3950.060	2.5309	(10, 8) O(3)	.08
3955.655	2.5273	(1, 0) Q(8)	.07
3988.761	2.5064	(5, 4) S(3)	.06
3997.637	2.5008	(3, 2) S(0)	.23
4000.075	2.4993	(1, 0) Q(7)	.23
4039.507	2.4749	(1, 0) Q(6)	.17
4073.739	2.4541	(1, 0) Q(5)	.51
4082.876	2.4486	(9, 7) O(5)	.08
4102.582[f]	2.436824	(1, 0) Q(4)	.45
4105.855	2.4349	(4, 3) S(2)	.11
4125.8739[f]	2.4230678	(1, 0) Q(3)	1.12
4143.4660[f]	2.4127801	(1, 0) Q(2)	.81
4155.25469[f]	2.4059349	(1, 0) Q(1)	1.59
4190.247	2.3858	(3, 2) S(1)	.47
4245.187	2.3550	(2, 1) S(0)	.42
4263.450	2.3449	(9, 7) O(4)	.08
4265.235	2.3439	(4, 3) S(3)	.13
4305.777	2.3218	(10, 8) Q(1)	.07
4372.445	2.2864	(3, 2) S(2)	.23
4437.230	2.2530	(9, 7) O(3)	.16
4448.958	2.2471	(2, 1) S(1)	.89
4497.8391[f]	2.2226833	(1, 0) S(0)	.73
4523.365	2.2101	(8, 6) O(5)	.13
4542.592	2.2008	(3, 2) S(3)	.28
4602.652	2.1721	(9, 7) O(2)	.08
4642.069	2.1536	(2, 1) S(2)	.44
4699.270	2.1274	(3, 2) S(4)	.09
4712.9054[f]	2.1212544	(1, 0) S(1)	1.60
4713.535	2.1210	(8, 6) O(4)	.12
4741.551	2.1084	(7, 5) O(6)	.05
4760.474	2.1001	(9, 7) Q(3)	.09
4798.307	2.0835	(9, 7) Q(2)	.07
4822.834	2.0729	(2, 1) S(3)	.56
4823.551	2.0726	(9, 7) Q(1)	.15
4831.006	2.0694	(12, 9) O(3)	.07
4841.305	2.0650	(3, 2) S(5)	.11
4897.691	2.0412	(8, 6) O(3)	.26
4917.0069[f]	2.0332026	(1, 0) S(2)	.80
4926.890	2.0291	(6, 4) O(7)	.06
4945.497	2.0215	(7, 5) O(5)	.18
4989.794	2.0035	(2, 1) S(4)	.19
5031.836	1.9868	(9, 7) S(0)	.06
5074.206	1.9702	(8, 6) O(2)	.13
5108.4040[f]	1.9570243	(1, 0) S(3)	1.07
5141.750	1.9443	(2, 1) S(5)	.25
5142.519	1.9440	(6, 4) O(6)	.07
5145.551	1.9429	(7, 5) O(4)	.18
5146.110	1.9427	(8, 6) Q(5)	.07
5146.794	1.9424	(9, 7) S(1)	.11
5154.249	1.9396	(12, 9) Q(1)	.06
5205.628	1.9205	(8, 6) Q(4)	.06
5253.408	1.9030	(8, 6) Q(3)	.16
5277.779	1.8942	(2, 1) S(6)	.08
5285.605	1.8914	(1, 0) S(4)	.37
5289.346	1.8901	(8, 6) Q(2)	.12
5311.340	1.8822	(5, 3) O(7)	.07
5313.358	1.8815	(8, 6) Q(1)	.25
5324.762	1.8775	(9, 7) S(3)	.05
5340.162	1.8721	(7, 5) O(3)	.37
5356.190	1.8665	(6, 4) O(5)	.24
5397.235	1.8523	(2, 1) S(7)	.12
5447.354	1.8353	(1, 0) S(5)	.53
5527.648	1.8086	(7, 5) O(2)	.20
5536.710	1.8056	(5, 3) O(6)	.08
5540.521	1.8044	(8, 6) S(0)	.10
5566.454	1.7960	(6, 4) O(4)	.23
5592.701	1.7876	(1, 0) S(6)	.16

TABLE 3—*Continued*

$\tilde{\nu}^a$ (cm^{-1})	λ^b µm	Transition	$100I/I_{total}$ per cent
5623.095	1.7779	(7, 5) Q(5)	.11
5669.074	1.7635	(8, 6) S(1)	.19
5678.910	1.7604	(11, 8) O(3)	.09
5680.408	1.7600	(7, 5) Q(4)	.09
5693.602	1.7559	(4, 2) O(7)	.07
5720.974	1.7475	(1, 0) S(7)	.28
5726.483	1.7458	(7, 5) Q(3)	.25
5760.586	1.7355	(5, 3) O(5)	.29
5761.176	1.7353	(7, 5) Q(2)	.19
5771.695	1.7321	(6, 4) O(3)	.49
5781.440	1.7292	(8, 6) S(2)	.08
5784.372	1.7283	(7, 5) Q(1)	.38
5831.779	1.7143	(1, 0) S(8)	.07
5869.432	1.7033	(13, 9) O(3)	.06
5876.153	1.7013	(8, 6) S(3)	.11
5924.972	1.6873	(1, 0) S(9)	.10
5927.655	1.6865	(11, 8) Q(3)	.05
5929.327	1.6861	(4, 2) O(6)	.09
5942.232	1.6824	(6, 4) Q(7)	.07
5970.171	1.6745	(6, 4) O(2)	.26
5981.457	1.6714	(5, 3) O(4)	.28
6019.476	1.6608	(6, 4) Q(6)	.05
6029.518	1.6581	(7, 5) S(0)	.16
6034.626	1.6567	(11, 8) Q(1)	.10
6066.969	1.6478	(10, 7) O(5)	.05
6077.752	1.6449	(3, 1) O(7)	.07
6086.233	1.6426	(6, 4) Q(5)	.16
6142.266	1.6276	(6, 4) Q(4)	.14
6163.885	1.6219	(4, 2) O(5)	.31
6170.692	1.6201	(7, 5) S(1)	.32
6187.362	1.6158	(6, 4) Q(3)	.35
6192.675	1.6144	(13, 9) Q(1)	.06
6197.628	1.6131	(5, 3) O(3)	.60
6217.391	1.6080	(5, 3) Q(9)	.05
6221.345	1.6069	(6, 4) Q(2)	.26
6244.079	1.6011	(6, 4) Q(1)	.53
6268.705	1.5948	(10, 7) O(4)	.06
6283.371	1.5911	(11, 8) S(1)	.07
6296.033	1.5879	(7, 5) S(2)	.15
6324.403	1.5807	(3, 1) O(6)	.08
6395.702	1.5631	(4, 2) O(4)	.31
6399.343	1.5622	(5, 3) Q(7)	.09
6404.081	1.5611	(7, 5) S(3)	.19
6407.274	1.5603	(5, 3) O(2)	.33
6456.572	1.5484	(10, 7) O(3)	.12
6475.567	1.5438	(5, 3) Q(6)	.07
6493.565	1.5396	(7, 5) S(4)	.07
6506.644	1.5365	(6, 4) S(0)	.23
6541.573	1.5283	(5, 3) Q(5)	.21
6563.423	1.5232	(7, 5) S(5)	.09
6570.116	1.5216	(3, 1) O(5)	.29
6597.082	1.5154	(5, 3) Q(4)	.18
6623.021	1.5095	(4, 2) O(3)	.67
6629.032	1.5081	(10, 7) O(2)	.07
6641.837	1.5052	(5, 3) Q(3)	.45
6659.746	1.5011	(6, 4) S(1)	.47
6671.530	1.4985	(4, 2) Q(9)	.06
6675.617	1.4976	(5, 3) Q(2)	.34
6698.241	1.4925	(5, 3) Q(1)	.68
6725.011	1.4866	(2, 0) O(6)	.05
6744.568	1.4823	(10, 7) Q(3)	.08
6777.326	1.4751	(9, 6) O(5)	.06
6797.157	1.4708	(6, 4) S(2)	.23
6803.562	1.4694	(10, 7) Q(2)	.07
6813.266	1.4673	(3, 1) O(4)	.30
6842.893	1.4610	(10, 7) Q(1)	.14
6843.949	1.4607	(4, 2) O(2)	.37
6852.945	1.4588	(4, 2) Q(7)	.11
6906.820	1.4474	(3, 1) Q(11)	.05
6917.405	1.4452	(6, 4) S(3)	.30
6929.074	1.4428	(4, 2) Q(6)	.09
6977.927	1.4327	(5, 3) S(0)	.30
6982.513	1.4318	(2, 0) O(5)	.20
6986.980	1.4308	(9, 6) O(4)	.07
6995.057	1.4292	(4, 2) Q(5)	.25
7019.222	1.4243	(6, 4) S(4)	.11
7037.090	1.4207	(10, 7) S(0)	.06
7050.593	1.4179	(4, 2) Q(4)	.21
7052.043	1.4176	(3, 1) O(3)	.65
7084.967	1.4111	(12, 8) O(3)	.06
7095.405	1.4090	(4, 2) Q(3)	.54
7101.575	1.4078	(6, 4) S(5)	.15
7125.343	1.4031	(3, 1) Q(9)	.07
7129.248	1.4023	(4, 2) Q(2)	.40
7130.888	1.4020	(10, 7) S(1)	.11
7142.450	1.3997	(5, 3) S(1)	.64
7151.926	1.3978	(4, 2) Q(1)	.79
7163.682	1.3955	(6, 4) S(6)	.05
7184.126	1.3916	(9, 6) O(3)	.16
7205.011	1.3875	(6, 4) S(7)	.08
7237.563	1.3813	(2, 0) O(4)	.20
7245.122	1.3799	(10, 7) S(3)	.07
7284.497	1.3724	(3, 1) O(2)	.36
7291.242	1.3711	(5, 3) S(2)	.32
7307.984	1.3680	(3, 1) Q(7)	.12
7341.614	1.3617	(9, 6) Q(5)	.05
7367.136	1.3570	(9, 6) O(2)	.09
7384.774	1.3538	(3, 1) Q(6)	.09
7422.824	1.3468	(5, 3) S(3)	.43
7440.684	1.3436	(12, 8) Q(1)	.08
7448.600	1.3422	(4, 2) S(0)	.37
7451.367	1.3417	(3, 1) Q(5)	.26
7452.009	1.3416	(8, 5) O(5)	.06
7488.28^f	1.335055	(2, 0) O(3)	.45
7507.369	1.3317	(9, 6) Q(3)	.12
7507.426	1.3317	(3, 1) Q(4)	.22
7535.939	1.3266	(5, 3) S(4)	.16
7552.656	1.3237	(3, 1) Q(3)	.56
7562.791	1.3219	(9, 6) Q(2)	.09
7582.815	1.3184	(2, 0) Q(9)	.06
7586.807	1.3177	(3, 1) Q(2)	.41
7599.793	1.3155	(9, 6) Q(1)	.19
7609.687	1.3138	(3, 1) Q(1)	.80
7624.311	1.3112	(4, 2) S(1)	.79
7629.575	1.3103	(5, 3) S(5)	.22
7644.113	1.3078	(12, 8) S(1)	.06
7670.413	1.3034	(8, 5) O(4)	.07
7702.978	1.2978	(5, 3) S(6)	.08
7732.63^f	1.292867	(2, 0) O(2)	.25
7755.649	1.2890	(5, 3) S(7)	.12
7768.209	1.2869	(2, 0) Q(7)	.09
7784.140	1.2843	(4, 2) S(2)	.40
7797.978	1.2820	(5, 3) S(9)	.07
7813.966	1.2794	(9, 6) S(0)	.09
7846.277	1.2741	(2, 0) Q(6)	.07
7877.279	1.2691	(8, 5) O(3)	.16
7914.033	1.2632	(2, 0) Q(5)	.20
7923.036	1.2618	(9, 6) S(1)	.18
7923.472	1.2617	(3, 1) S(0)	.38
7926.577	1.2612	(4, 2) S(3)	.55
7971.109	1.2542	(2, 0) Q(4)	.17
8009.424	1.2482	(9, 6) S(2)	.08
8017.19^f	1.246979	(2, 0) Q(3)	.42
8050.340	1.2418	(4, 2) S(4)	.21
8051.991^f	1.241589	(2, 0) Q(2)	.30
8070.898	1.2387	(8, 5) O(2)	.10
8071.657	1.2386	(9, 6) S(3)	.12
8074.754	1.2381	(8, 5) Q(5)	.07

TABLE 3—*Continued*

$\tilde{\nu}^a$ (cm^{-1})	λ^b µm	Transition	$100I/I_{total}$ per cent	$\tilde{\nu}^a$ (cm^{-1})	λ^b µm	Transition	$100I/I_{total}$ per cent
8075.3114^f	1.2380036	(2, 0) Q(1)	.59	9706.371	1.0300	(6, 3) Q(1)	.22
8103.086	1.2338	(7, 4) O(5)	.05	9721.012	1.0284	(7, 4) S(5)	.12
8110.300	1.2327	(3, 1) S(1)	.84	9727.356	1.0277	(7, 4) S(7)	.07
8118.563	1.2314	(9, 6) S(5)	.06	9858.970	1.0140	(5, 2) O(3)	.11
8154.401	1.2260	(4, 2) S(5)	.30	9907.130	1.0091	(10, 6) S(1)	.08
8162.507	1.2248	(8, 5) Q(4)	.05	9974.619	1.0023	(6, 3) S(0)	.12
8185.422	1.2213	(11, 7) O(3)	.05	9992.018	1.0005	(10, 6) S(3)	.06
8232.995	1.2143	(8, 5) Q(3)	.14	10085.559	.9912	(5, 2) O(2)	.07
8237.997	1.2136	(4, 2) S(6)	.10	10122.038	.9877	(6, 3) S(1)	.27
8280.967	1.2073	(3, 1) S(2)	.44	10152.646	.9847	(5, 2) Q(5)	.06
8286.038	1.2065	(8, 5) Q(2)	.11	10235.980	.9767	(5, 2) Q(4)	.05
8300.631	1.2044	(4, 2) S(7)	.18	10248.120	.9755	(6, 3) S(2)	.14
8321.488	1.2014	(8, 5) Q(1)	.22	10303.179	.9703	(5, 2) Q(3)	.13
8330.938	1.2000	(7, 4) O(4)	.06	10351.468	.9658	(6, 3) S(3)	.22
8339.787	1.1987	(4, 2) S(11)	.06	10353.901	.9656	(5, 2) Q(2)	.10
8342.060	1.1984	(4, 2) S(8)	.06	10387.876	.9624	(5, 2) Q(1)	.20
8362.266	1.1955	(4, 2) S(9)	.11	10430.917	.9584	(6, 3) S(4)	.09
8406.365^f	1.1892493	(2, 0) S(0)	.29	10446.889	.9570	(6, 3) S(9)	.06
8433.906	1.1854	(3, 1) S(3)	.62	10485.559	.9534	(6, 3) S(5)	.13
8547.937	1.1696	(7, 4) O(3)	.16	10486.957	.9533	(9, 5) Q(3)	.05
8554.381	1.1687	(8, 5) S(0)	.11	10514.335	.9508	(4, 1) O(3)	.06
8567.798	1.1668	(3, 1) S(4)	.24	10514.751	.9508	(6, 3) S(6)	.05
8571.743	1.1663	(11, 7) Q(1)	.07	10518.106	.9505	(6, 3) S(7)	.09
8604.2189^f	1.1619025	(2, 0) S(1)	.66	10607.923	.9424	(9, 5) Q(1)	.08
8677.205	1.1521	(8, 5) S(1)	.23	10673.254	.9367	(5, 2) S(0)	.11
8681.600	1.1515	(3, 1) S(5)	.35	10832.085	.9229	(5, 2) S(1)	.25
8752.301	1.1422	(7, 4) O(2)	.10	10931.166	.9146	(9, 5) S(1)	.10
8774.565	1.1393	(3, 1) S(6)	.12	10969.527	.9114	(5, 2) S(2)	.14
8778.132	1.1389	(8, 5) S(2)	.11	10986.719	.9099	(4, 1) Q(3)	.09
8780.684	1.1386	(7, 4) Q(5)	.07	11006.116	.9083	(9, 5) S(2)	.05
8785.529^f	1.1379238	(2, 0) S(2)	.35	11037.771	.9057	(4, 1) Q(2)	.07
8820.488	1.1334	(11, 7) S(1)	.07	11047.207	.9050	(9, 5) S(5)	.05
8846.242	1.1301	(3, 1) S(7)	.22	11051.245	.9046	(9, 5) S(3)	.08
8855.740	1.1289	(8, 5) S(3)	.16	11071.979	.9029	(4, 1) Q(1)	.13
8865.795	1.1276	(7, 4) Q(4)	.06	11084.165	.9019	(5, 2) S(3)	.21
8896.464	1.1237	(3, 1) S(8)	.08	11174.837	.8946	(5, 2) S(4)	.09
8908.791	1.1222	(8, 5) S(4)	.06	11240.648	.8894	(5, 2) S(5)	.14
8911.150	1.1219	(8, 5) S(7)	.05	11246.985	.8889	(5, 2) S(9)	.07
8920.150	1.1208	(3, 1) S(11)	.08	11280.982	.8862	(5, 2) S(6)	.05
8925.314	1.1201	(3, 1) S(9)	.15	11295.499	.8851	(5, 2) S(7)	.09
8934.257	1.1190	(7, 4) Q(3)	.15	11374.435	.8789	(4, 1) S(0)	.08
8936.243	1.1187	(8, 5) S(5)	.09	11544.363	.8660	(4, 1) S(1)	.19
8948.703	1.1172	(2, 0) S(3)	.50	11557.437	.8650	(8, 4) Q(1)	.07
8978.149	1.1135	(6, 3) O(4)	.05	11692.662	.8550	(4, 1) S(2)	.11
8985.830	1.1126	(7, 4) Q(2)	.12	11764.948^g	.8497490	(3, 0) Q(1)	.06
9020.321	1.1083	(7, 4) Q(1)	.23	11817.891	.8459	(4, 1) S(3)	.17
9092.375	1.0995	(2, 0) S(4)	.20	11913.154	.8392	(8, 4) S(1)	.09
9205.758	1.0860	(6, 3) O(3)	.14	11918.867	.8388	(4, 1) S(4)	.07
9215.488	1.0848	(2, 0) S(5)	.29	11994.695	.8335	(4, 1) S(5)	.11
9271.128	1.0783	(7, 4) S(0)	.12	12002.786	.8329	(8, 4) S(2)	.05
9317.285	1.0730	(2, 0) S(6)	.11	12038.602	.8304	(4, 1) S(9)	.06
9397.311	1.0638	(2, 0) S(7)	.21	12063.515	.8287	(8, 4) S(3)	.08
9406.642	1.0628	(7, 4) S(1)	.26	12068.765	.8284	(4, 1) S(7)	.08
9421.134	1.0612	(6, 3) O(2)	.09	12093.831	.8266	(8, 4) S(5)	.06
9455.395	1.0573	(2, 0) S(8)	.07	12265.543^g	.8150680	(3, 0) S(1)	.10
9470.217	1.0557	(6, 3) Q(5)	.07	12424.443^g	.8046445	(3, 0) S(2)	.06
9491.630	1.0533	(2, 0) S(9)	.15	12482.612	.8009	(7, 3) Q(1)	.05
9499.977	1.0523	(2, 0) S(11)	.07	12559.776	.7960	(3, 0) S(3)	.09
9520.687	1.0501	(7, 4) S(2)	.13	12755.339	.7838	(3, 0) S(5)	.06
9553.961	1.0464	(6, 3) Q(4)	.06	12868.933	.7769	(7, 3) S(1)	.08
9611.856	1.0401	(7, 4) S(3)	.20	13045.919	.7663	(7, 3) S(3)	.08
9619.135	1.0393	(10, 6) Q(1)	.07	13104.996	.7629	(7, 3) S(5)	.06
9621.425	1.0391	(6, 3) Q(3)	.15	13811.672	.7238	(6, 2) S(1)	.06
9672.309	1.0336	(6, 3) Q(2)	.11	14012.810	.7134	(6, 2) S(3)	.06
9678.952	1.0329	(7, 4) S(4)	.08				

[a] Wavenumber in vacuum (see text).
[b] Wavelength in standard air.
[c] Jennings and Brault 1983.
[d] Jennings, Rahn, and Owyoung 1985.
[e] Knacke and Young 1981.
[f] Bragg, Brault, and Smith 1982.
[g] Fink, Wiggins, and Rank 1965, based on original measurements of Herzberg 1950.

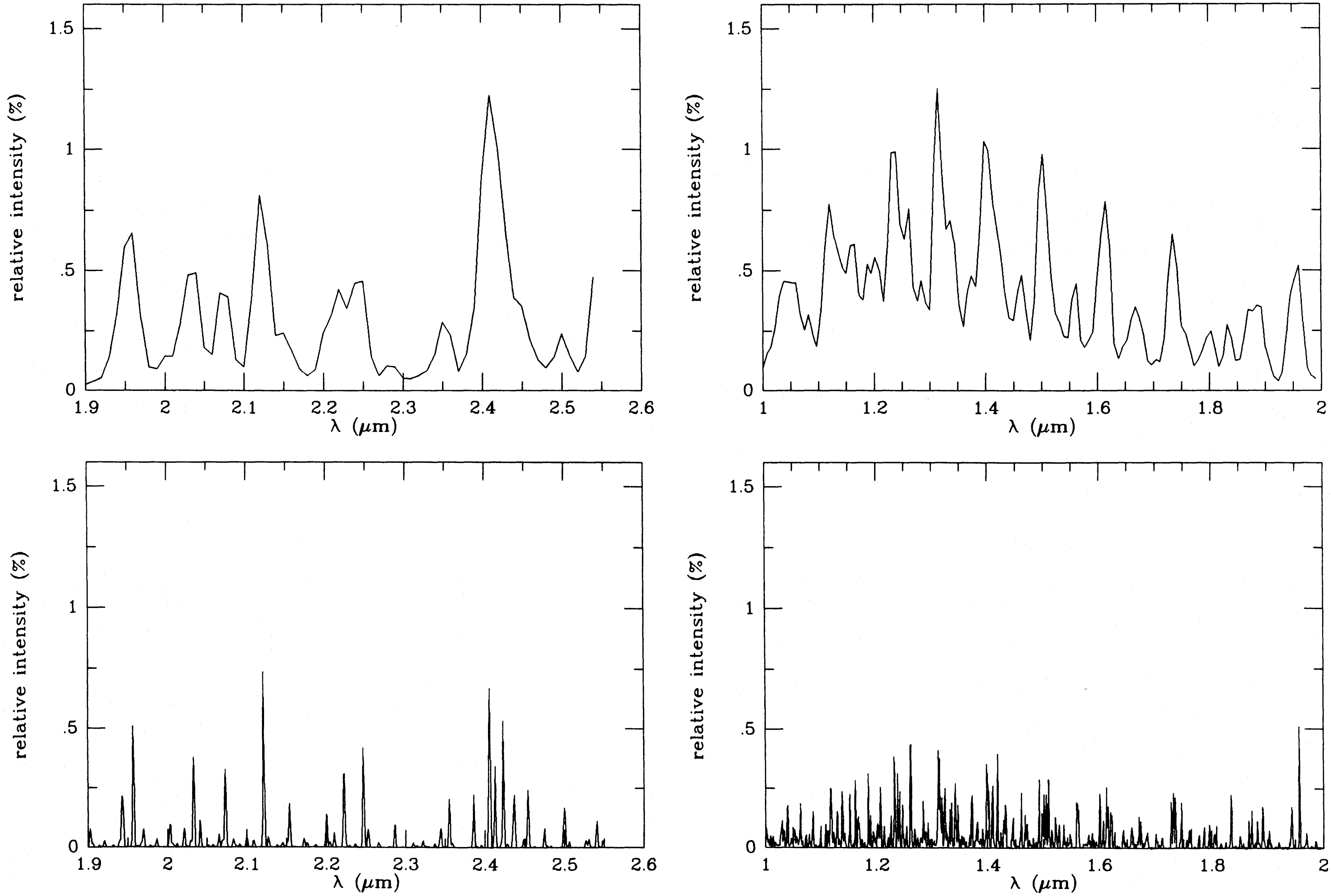

FIG. 3.—Effect of resolution on the appearance of the model 14 simulated spectra. Upper panels are identical with those in Fig. 2. The spectra in the lower panels were computed with $\Delta\lambda = 0.002$ μm (*left*) and 0.0015 μm (*right*). The intensity scales are in units of $0.01 I_{\rm total}/\Delta\lambda$.

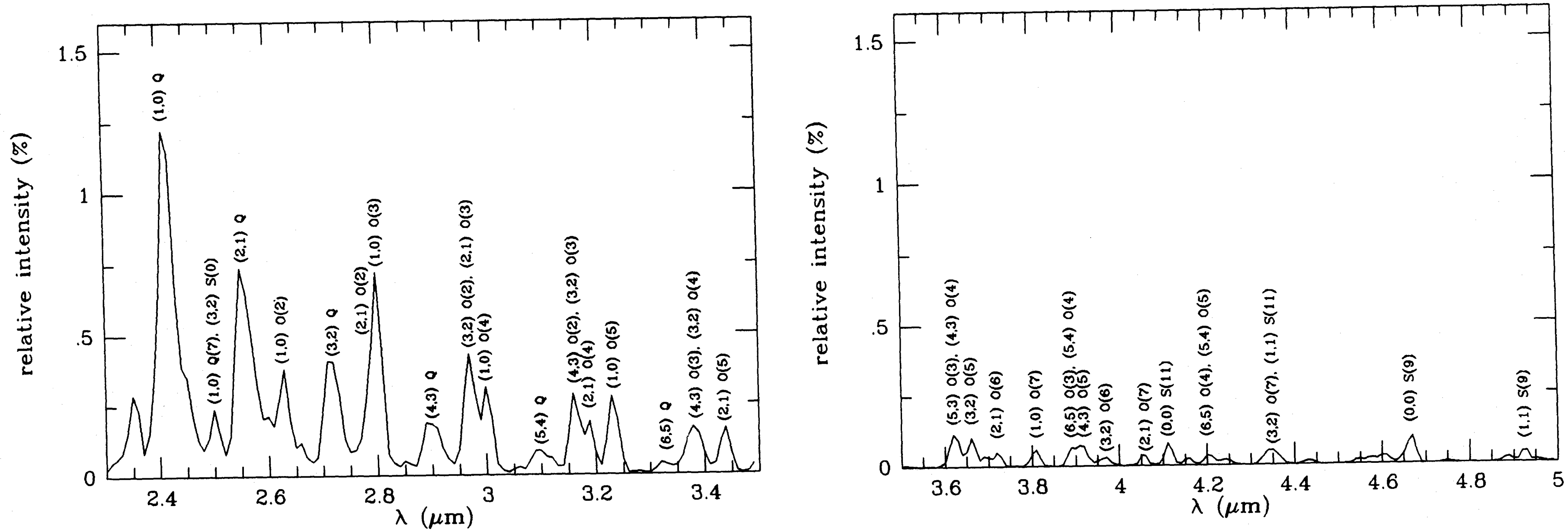

FIG. 4.—Simulated spectrum of model 14 at longer wavelengths. The principal contributors to each strong feature are indicated. The resolution is $\Delta\lambda = 0.02$ μm in both panels. The intensity scale is described in the legend for Fig. 2.

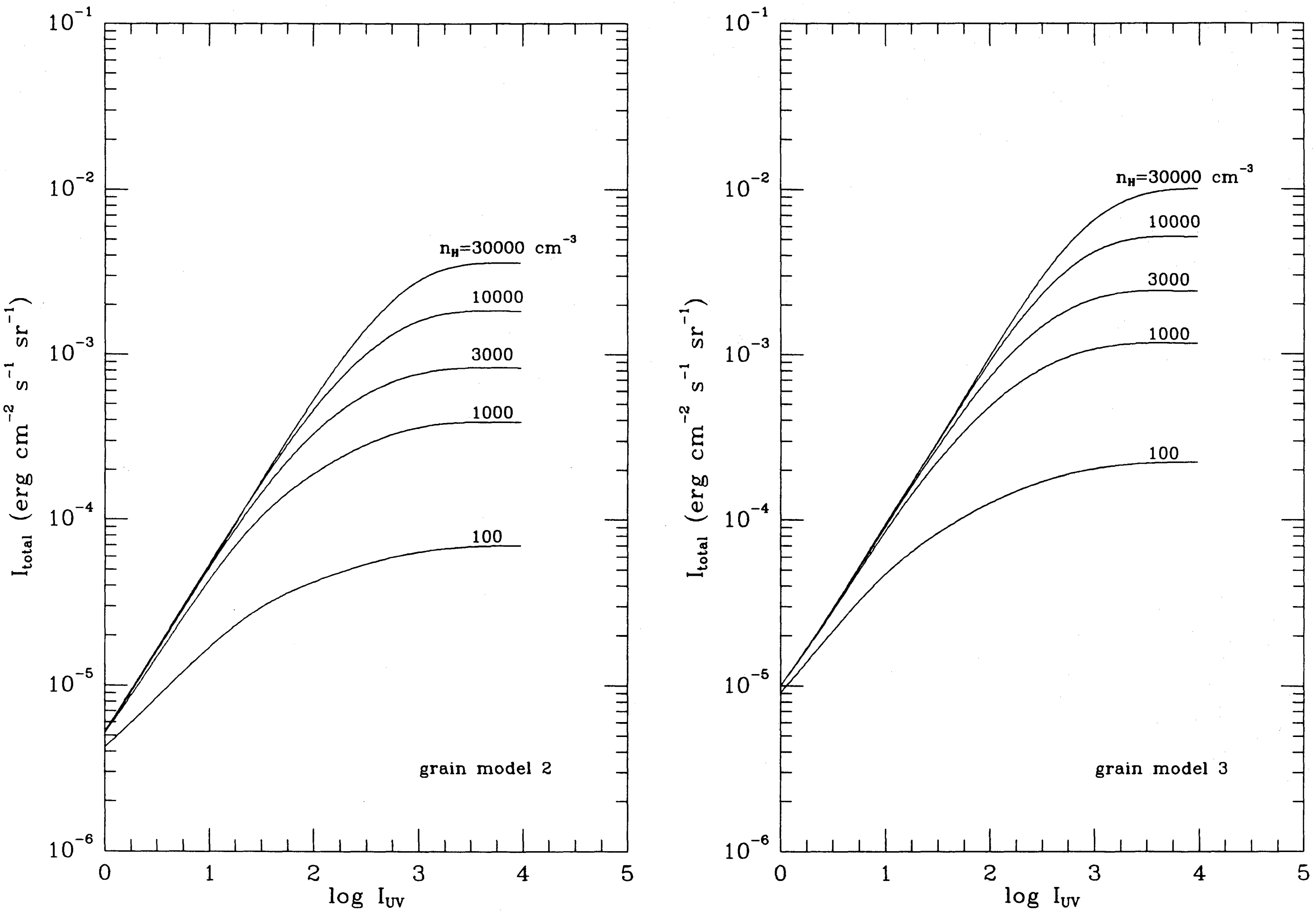

FIG. 5.—Dependence of total fluorescent intensity on the intensity of ultraviolet radiation and hydrogen density. Results for models 1–25 of Table 1 (*left*) and for models 40–69 of Table 4 (*right*).

critical extinction A_V^* such that $\tau_{v'J',01} \approx 1$,

$$A_V^* = 0.20 \frac{I_{UV}}{n_H} \left(\frac{100}{T}\right)^{1/2} \left(\frac{3}{y_f}\right) \left(\frac{0.01}{f}\right) \left(\frac{1000}{\lambda}\right) \left(\frac{b}{3}\right) \text{ mag} , \qquad (15)$$

which follows from equations (9) and (14), and the adopted gas/extinction ratio

$$N_H = N(\mathrm{H}) + 2N(\mathrm{H}_2) = 1.59 \times 10^{21} A_V \text{ cm}^{-2} , \qquad (16)$$

where A_V is the visual extinction in mag. On the other hand, the continuum attenuation by grains corresponds, for grain model 2 at λ1000 Å, to an effective optical depth

$$\tau_{\mathrm{eff}} = s_\lambda \tau_V \approx 3.0 A_V \approx 1.13 \left(\frac{N_H}{6 \times 10^{20}}\right) \qquad (17)$$

that characterizes the continuum attenuation function (§ II). Comparison of equations (15) and (17) indicates that the line and continuum optical depths at 1000 Å are initially comparable when the ratio I_{UV}/n_H is of the order of unity. Thus when $I_{UV}/n_H \ll 1$, line absorption completely dominates the attenuation of the ultraviolet radiation and most of the available photons dissociate and excite H_2. When $I_{UV}/n_H \gtrsim 1$, however, some of these photons are removed by the grains so that the efficiency of excitation of H_2 is reduced. This means that the presence of an intense ultraviolet radiation field (large value of I_{UV}) will not yield the maximum H_2 fluorescence unless the density, n_H, is also large. For the models of Table 1, I_{total} falls a factor of $1/e$ below the linear extrapolation of its value at low I_{UV} for $I_{UV}/n_H \approx 0.07$.

In contrast with the *total* H_2 infrared intensity, the *relative* line intensities are remarkably insensitive to the density and strength of the radiation field. In Figure 6, model spectra at low resolution are presented in the 1–2.5 μm region for a range of densities (*top*) and a range of values of I_{UV} (*bottom*), with all other parameters kept fixed. No noticeable differences can be found in the relative spectra over the range of densities $n_H = 10^2$–3×10^4 cm^{-3}. For intensities I_{UV} ranging between 10 and 10^4, some slight differences

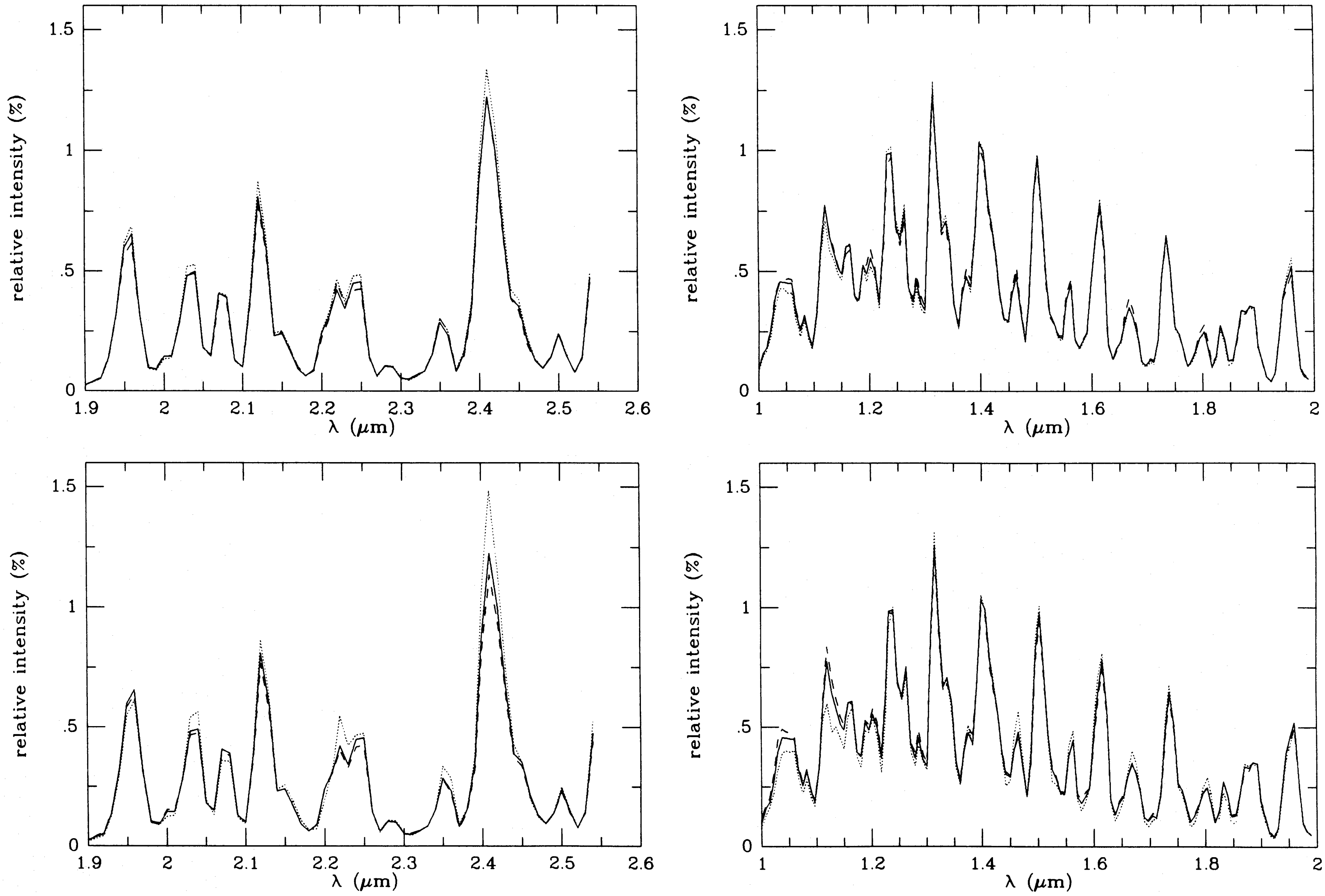

FIG. 6.—Upper panels illustrate the sensitivity of the simulated spectra to density: the solid curve is for model 14 ($n_H = 3000$); the dotted curve is for model 4 ($n_H = 100$); and the dashed curve is for model 24 ($n_H = 30{,}000$). Lower panels illustrate the sensitivity of the simulated spectra to I_{UV}: the solid curve is for model 14 ($I_{UV} = 10^3$), the dotted curve is for model 12 ($I_{UV} = 10^2$); and the dashed curve is for model 15 ($I_{UV} = 10^4$). Resolution and intensity scales are as in Fig. 2.

occur for low $I_{UV} < 10^2$ in the strengths of the (1, 0) lines, but otherwise the spectra are very similar. The insensitivity of the relative line strengths to n_H and I_{UV} is not surprising, since in the parameter regime $n_H < 10^5$ cm^{-3} and $I_{UV} < 10^5$ the populations of the excited vibration-rotation levels of H_2 are controlled by purely radiative cascade processes. Although for $I_{UV} > 10^3$ multiple pumping out of vibrationally excited states can have a 10% or larger effect on level populations, the relative spectra are not significantly affected.

c) Effects of Grain Properties

Because the total H_2 infrared intensity I_{total} depends on the competition between grains and H_2 molecules for the available ultraviolet photons, there are several grain properties that can cause the fluorescent excitation to be more *efficient*, i.e., to yield higher values of I_{total} for the same I_{UV} and n_H. Most models presented in Table 1 were computed using grain model 2 (cf. Roberge, Dalgarno, and Flannery 1981), which has a moderately large albedo $\omega \approx 0.5$ and is partly forward scattering, with $g \approx 0.5$ at the relevant wavelengths $\lambda \approx 912$–1200 Å for H_2 excitation, resulting in an exponential attenuation factor $s_\lambda \approx 3$ (cf. § II). Various recent studies of the ultraviolet grain scattering properties (Chlewicki and Greenberg 1984*a*, *b*; Draine and Lee 1984) have suggested that a more forward-scattering phase function, $g \approx 0.7$–0.9, may be more appropriate for reflection nebulae. At the same time, however, the observations and theories appear to imply a somewhat smaller albedo than is used in grain model 2, $\omega \lesssim 0.4$. The combined effect of the smaller albedo and the larger asymmetry parameter is to give an attenuation factor $s_\lambda \approx 3$ that is consistent with grain model 2. If, however, a grain scattering model with both a more forward-scattering phase function and a higher albedo is used, the exciting photons will be able to penetrate more deeply before being removed by grain absorption. This is illustrated by some models in Table 1 which were obtained with grain model 3, which has $\omega \approx 0.8$ and $g = 1$ at ultraviolet wavelengths, corresponding to $s_\lambda \approx 0.8$. A comparison of models 14 and 28 in Table 1 shows that the total H_2 intensity is increased considerably. In Figure 5*b* and Table 4, the dependence of I_{total} on I_{UV} and n_H is presented for a range of models using grain model 3. For a given density, the asymptotic value of I_{total} is about a factor of 3 larger with grain model 3 than with grain model 2, and I_{total} falls a factor of $1/e$ below the linear extrapolation for $I_{UV}/n_H \approx 0.3$.

Another grain property which affects the total H_2 infrared intensity is the formation efficiency of H_2 on grain surfaces. All models in Table 1 were calculated with a slightly enhanced efficiency, $y_f = 3$. This larger efficiency was chosen to maximize the H_2 infrared line intensities. Even so, a larger efficiency may be appropriate to reflection nebulae, where near-infrared continuum emission

TABLE 4

CLOUD MODEL RESULTS FOR GRAIN MODEL 3

Model[a]	n_H (cm^{-3})	T (K)	I_{UV}	A_V (mag)	N(H) (cm^{-2})	$N(H_2^*)$ (cm^{-2})	I_{total} (erg s^{-1} cm^{-2} sr^{-1})	ε
40	1.0(2)	100	2(0)	13.13	9.5(20)	9.9(13)	1.52(-5)	1.6(-1)
41	1.0(2)	100	1(1)	14.22	2.7(21)	3.1(14)	4.76(-5)	1.0(-1)
42	1.0(2)	100	3(1)	15.35	4.5(21)	5.3(14)	8.18(-5)	5.7(-2)
43	1.0(2)	100	1(2)	16.75	6.7(21)	8.4(14)	1.27(-4)	2.7(-2)
44	1.0(2)	100	1(3)	19.53	1.1(22)	1.3(15)	2.04(-4)	4.3(-3)
45	1.0(2)	100	1(4)	22.36	1.6(22)	1.4(15)	2.24(-4)	4.7(-4)
46	1.0(3)	100	2(0)	12.65	1.2(20)	1.2(14)	1.85(-5)	1.9(-1)
47	1.0(3)	100	1(1)	12.88	5.0(20)	5.6(14)	8.63(-5)	1.8(-1)
48	1.0(3)	100	3(1)	13.34	1.2(21)	1.4(15)	2.19(-4)	1.5(-1)
49	1.0(3)	100	1(2)	14.31	2.8(21)	3.2(15)	4.93(-4)	1.0(-1)
50	1.0(3)	100	1(3)	16.95	7.0(21)	6.7(15)	1.08(-3)	2.3(-2)
51	1.0(3)	100	1(4)	19.84	1.2(22)	7.0(15)	1.17(-3)	2.5(-3)
52	3.0(3)	100	2(0)	12.60	4.3(19)	1.2(14)	1.88(-5)	2.0(-1)
53	3.0(3)	100	1(1)	12.69	1.9(20)	6.1(14)	9.24(-5)	1.9(-1)
54	3.0(3)	100	3(1)	12.88	5.1(20)	1.7(15)	2.65(-4)	1.9(-1)
55	3.0(3)	100	1(2)	13.46	1.4(21)	4.8(15)	7.40(-4)	1.6(-1)
56	3.0(3)	100	1(3)	15.78	5.1(21)	1.4(16)	2.17(-3)	4.6(-2)
57	3.0(3)	100	1(4)	18.73	9.8(21)	1.4(16)	2.41(-3)	5.1(-3)
58	1.0(4)	100	2(0)	12.59	1.3(19)	1.2(14)	1.88(-5)	2.0(-1)
59	1.0(4)	100	1(1)	12.61	6.1(19)	6.3(14)	9.52(-5)	2.0(-1)
60	1.0(4)	100	3(1)	12.68	1.8(20)	1.9(15)	2.84(-4)	2.0(-1)
61	1.0(4)	100	1(2)	12.91	5.6(20)	6.1(15)	9.22(-4)	1.9(-1)
62	1.0(4)	100	1(3)	14.63	3.3(21)	2.6(16)	4.19(-3)	8.8(-2)
63	1.0(4)	100	1(4)	17.57	8.0(21)	3.0(16)	5.16(-3)	1.1(-2)
64	3.0(4)	100	2(0)	12.58	4.2(18)	1.2(14)	1.87(-5)	2.0(-1)
65	3.0(4)	100	1(1)	12.59	2.4(19)	6.3(14)	9.48(-5)	2.0(-1)
66	3.0(4)	100	3(1)	12.61	6.3(19)	1.9(15)	2.86(-4)	2.0(-1)
67	3.0(4)	100	1(2)	12.70	2.1(20)	6.5(15)	9.88(-4)	2.1(-1)
68	3.0(4)	100	1(3)	13.73	1.9(21)	4.1(16)	6.58(-3)	1.4(-1)
69	3.0(4)	100	1(4)	16.53	6.3(21)	6.0(16)	1.01(-2)	2.1(-2)

[a] All of models 40–69 were computed with grain model 3, formation model $\varphi = 1$, $N(H_2) = 1.0 \times 10^{22}$ cm^{-2}, $b = 4.0$ km s^{-1}, $y_f = 3.0$, and $\alpha = 0.0$, unless otherwise indicated.

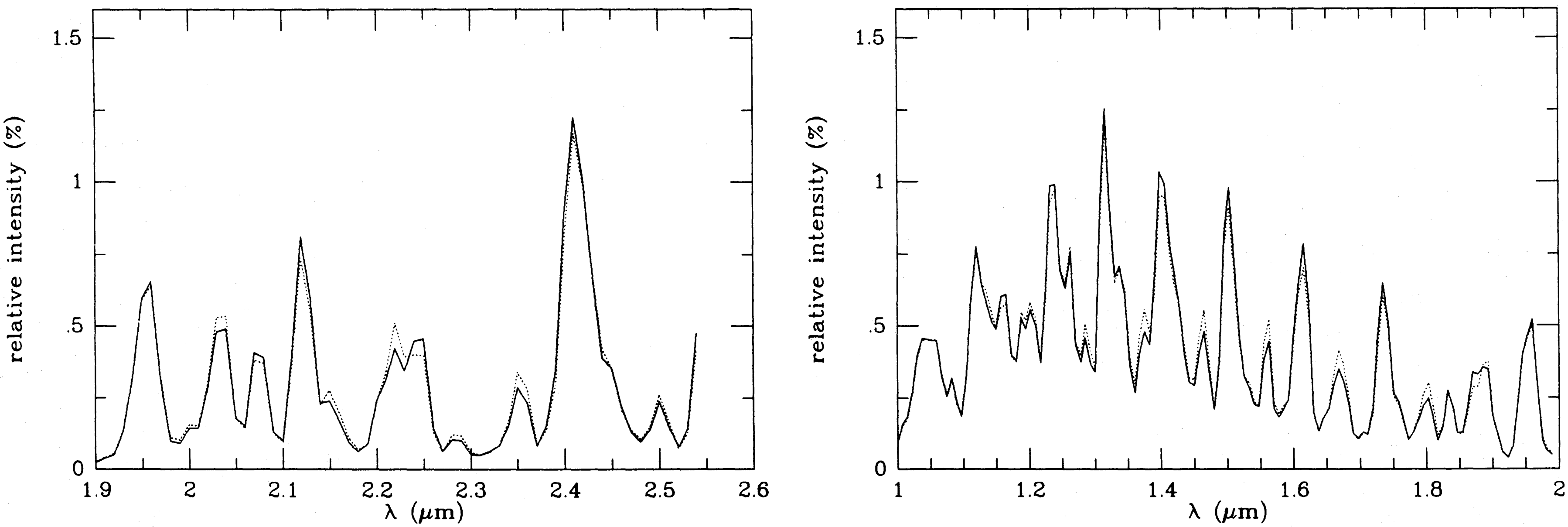

FIG. 7.—Sensitivity of simulated spectra to temperature: the solid curve is for model 14 ($T = 100$ K), and the dotted curve is for model 26 ($T = 30$ K). Resolution and intensity scales are as in Fig. 2.

measurements have revealed the presence of a large number of very small grains (Sellgren 1984; Sellgren *et al.* 1985). The corresponding increase in total surface area may enhance the H_2 formation rate. As equation (15) shows, the competition between grains and molecules for the ultraviolet photons depends not only on I_{UV} and n_H but actually on the ratio $I_{UV}/n_H y_f$. The larger y_f, the more rapidly are H_2 molecules formed in the outer parts of the cloud. Thus the excitation rate per unit volume will be higher, leading to a larger infrared intensity. Quantitatively, the effects on $I_{\rm total}$ of varying y_f can be incorporated by scaling n_H accordingly. On the other hand, in dense, quiescent clouds the grain surface area might be reduced through coagulation (Snow 1983; Jura 1980), thus diminishing the value of y_f. Consequently, y_f remains an uncertain parameter in the models.

Finally, the gas-to-extinction ratio can influence $I_{\rm total}$. If the gas-to-extinction ratio, N_H/A_V, is increased above the adopted value (eq. [16]), the ultraviolet photons will also effect more H_2 excitations before being removed by the grains. In some galaxies, such as the Large Magellanic Cloud (LMC) and the Small Magellanic Cloud (SMC), the gas-to-extinction ratio appears to be enhanced with respect to the local Milky Way value by factors of 4 and about 15, respectively (Koornneef 1982; Bouchet *et al.* 1985). Model 35 in Table 1 was constructed with a larger gas-to-dust ratio, and comparison with model 14 shows that indeed $I_{\rm total}$ is enhanced significantly. This increase in $I_{\rm total}$ will be partly offset, however, by a corresponding decrease in the H_2 formation efficiency on grains. Models 36 and 37 in Table 1 incorporate this reduced H_2 formation efficiency, and the resulting total H_2 intensity is only slightly larger ($\sim 20\%$) than that of model 14.

Although the grain properties affect significantly the total H_2 excitation, the relative line intensities are again changed only slightly.

d) Effects of Temperature

A final parameter that can increase the total H_2 infrared line intensity at a given density and intensity of the ultraviolet radiation field is the temperature in the cloud. The temperature can influence the H_2 excitation in two ways. First, a higher temperature increases the H_2 formation rate (cf. eq. [6]) and thus has the same effect as a larger H_2 formation efficiency. Second, a higher temperature causes the populations in the lowest levels $v = 0$, J to be distributed over more levels through collisions. Thus the ultraviolet absorption lines out of these levels will become optically thick slightly deeper into the cloud, thereby increasing the total H_2 excitation. Comparison of models 26 and 27 with model 14 in Table 1 shows that a factor of 4 increase in $I_{\rm total}$ may result over the temperature range $T = 30$–300 K.

The temperature in the cloud also affects the relative line intensities, as is demonstrated in Figure 7. As mentioned above, the populations in the lowest levels $v = 0$, J are controlled—at least in part—by collisions and thus reflect the distributions of temperature through a cloud. These levels are among the most populous, and the ultraviolet absorptions out of them dominate the excitation rate over a large part of the cloud. Although the excited vibrational population distributions are controlled by the intrinsic radiative properties of the molecule, the rotational distributions within them reflect somewhat the relative populations of those rotational levels that contribute most to the absorption rates. In this way, the temperature sensed by the lowest levels through collisions can affect the populations of the highly excited levels and consequently the appearance of the infrared fluorescence spectrum.

e) Effects of the H_2 *Formation Model*

The effects of the initial population distribution of H_2 upon formation have been investigated by running cloud models which use formation mechanisms $\varphi = 2$ and $\varphi = 3$ (see models 30–32 in Table 1). For formation model $\varphi = 3$, both a low formation temperature $T_f = 15$ K and a higher formation temperature $T_f = 65$ K have been considered. As Table 1 indicates, the *total* H_2 infrared intensity changes only slightly if a different formation model is employed. However, the *relative* line intensities are quite sensitive to the formation model, as Figure 8 illustrates. Although the H_2 formation rate is only 10%–20% of the fluorescent excitation rate, the formation mechanism can influence the populations of those specific levels into which the formation occurs (cf. § II). For example, in formation model 1, the rotational temperature in $v = 1$ is clearly higher than in formation model 2, as is demonstrated, e.g., by the relatively higher intensity in the (1, 0) $S(3)$ line and the lower intensity in the (1, 0) $S(0)$ line. A model with a lower formation temperature $T_f = 15$ K results in a quite different ortho/para H_2 ratio, as the bottom part of Figure 8 shows: the (1, 0) and (2, 1) $S(0)$ and $S(2)$ lines are relatively much stronger in this model than in model 14 with formation mechanism $\varphi = 1$. The differences among the various models are even more pronounced in certain lines in the 1–2 μm region. In particular, the (6, 4) $O(2)$ line at 1.67 μm, and to a lesser extent the (6, 4) $O(3)$ line at 1.73 μm and the (6, 4) Q branch at 1.6 μm, are affected with formation model 3. This is not surprising, since all the newly formed H_2 molecules enter the $v = 6$, $J = 0$ and $J = 1$ levels in formation mechanism 3. If the H_2 molecules were forced to enter, say, vibrational level $v = 3$ instead of $v = 6$ upon formation in the models, strong differences would occur in the relative intensities of the (3, 1) O and Q lines in the 1.3–1.4 μm region. Thus detailed infrared line observations of H_2 in the 1–2 μm region may be useful in probing the nature of the interstellar grains through their sensitivity to the initial population distribution of H_2 upon formation.

f) Effects of Other Parameters

There are various other parameters in the models that can affect the H_2 excitation. Most of the directions in which the results will change can be anticipated from the discussions in the previous sections. For example, if a smaller Doppler parameter b for the H_2 ultraviolet absorption lines is employed, the lines become optically thick at smaller depths into the cloud. Consequently, the total H_2 infrared intensity is expected to be lower. This effect is demonstrated quantitatively in Table 1 by comparing models 33 and 14. If a smaller total H_2 column density is used, the excited H_2 vibration-rotation column densities might not fully reach their asymptotic values, and the total H_2 excitation will thus be smaller. In Table 1, model 34 with a column density $N(H_2) = 10^{21}$ cm^{-2} can be compared with model 14 to assert the effect. Somewhat more difficult to predict is, for example, the influence that the employed H-H_2 and H_2-H_2 collisional cross sections will have on the appearance of the H_2 infrared spectra. The collisional processes affect

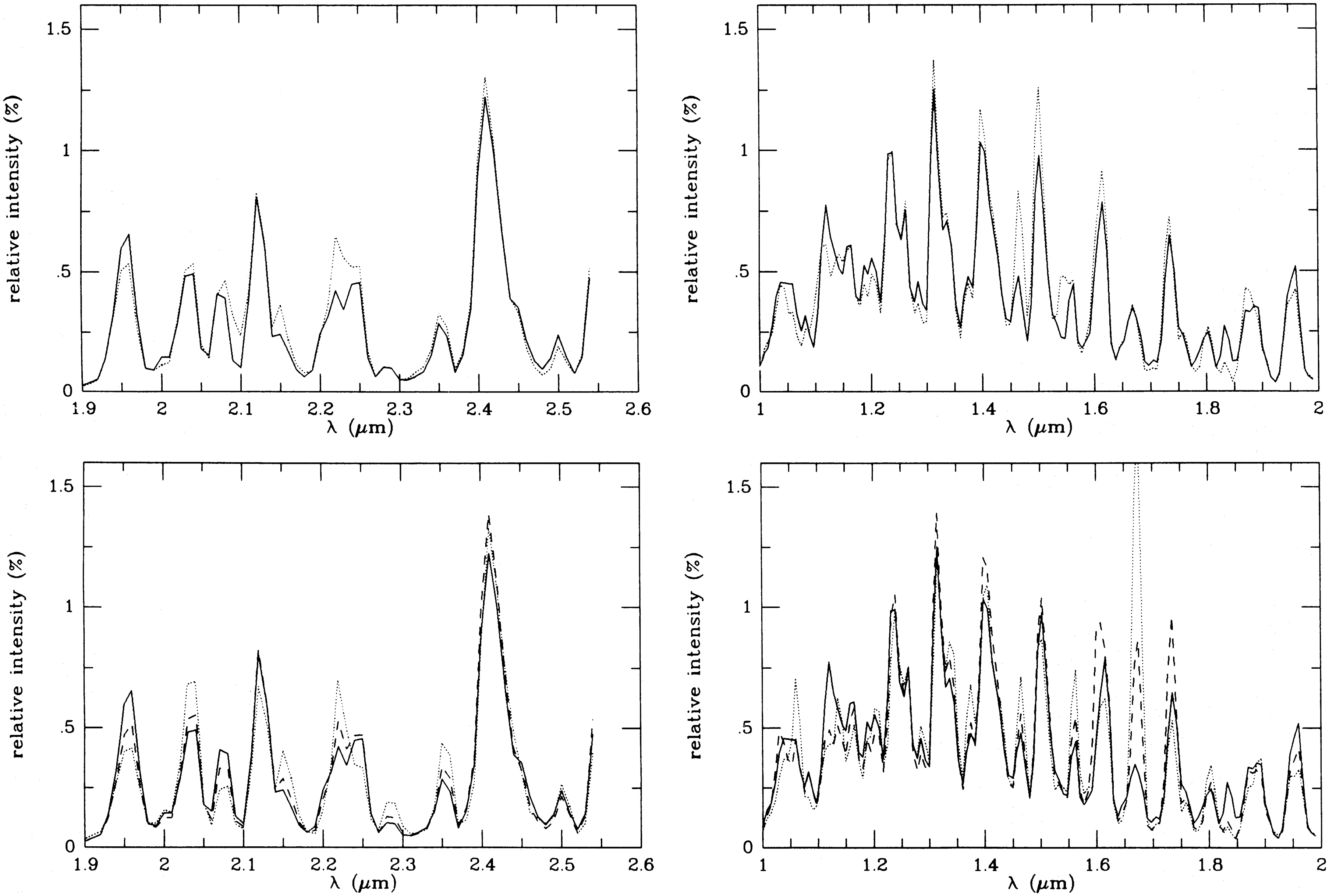

FIG. 8.—Sensitivity of simulated spectra to the H_2 formation model. *Upper panels*: The solid curve is for model 14 ($\varphi = 1$), and the dotted curve is for model 30 ($\varphi = 2$). *Lower panels*: The solid curve is for model 14, the dotted curve is for model 31 ($\varphi = 3$, $T_f = 15$ K), and the dashed curve is for model 32 ($\varphi = 3$, $T_f = 65$ K). Resolution and intensity scales are as in Fig. 2.

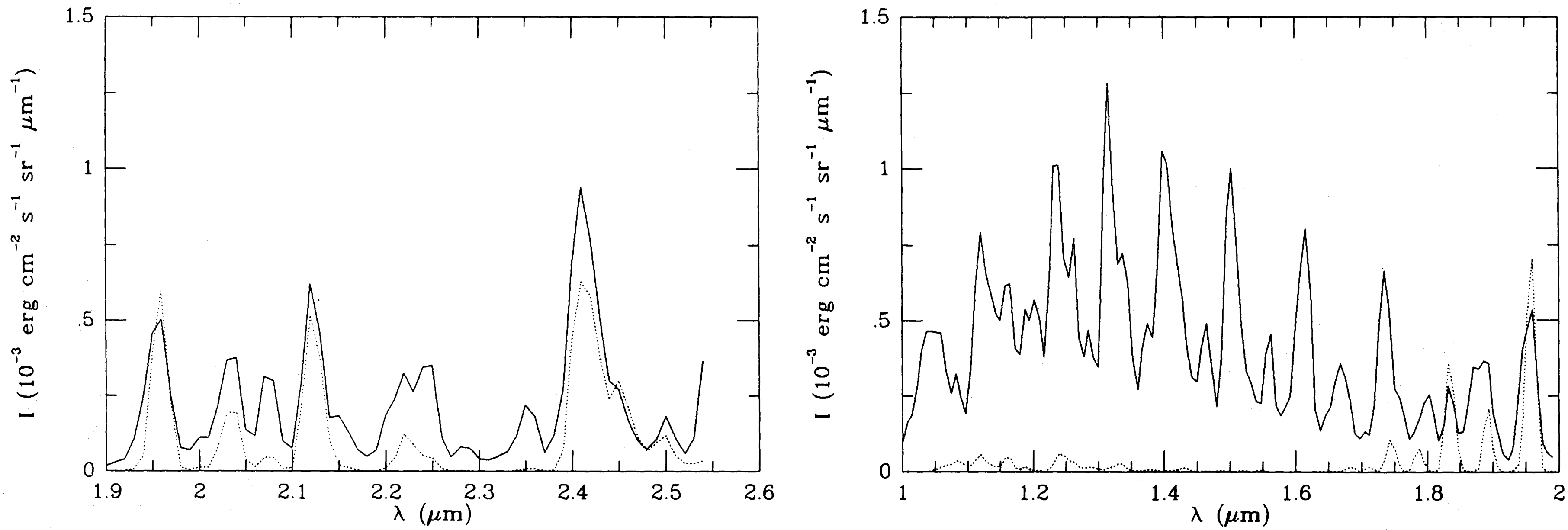

FIG. 9.—Comparison of fluorescent and thermal emission. The simulated spectrum of model 14 is shown by the solid curve, and the corresponding spectrum of the thermal model S2 ($T = 2000$ K) is shown by the dotted curve. Resolution is as in Fig. 2.

the relative populations of the levels $v = 0, J$ out of which the majority of H_2 excitations originate. Some test calculations were run with a different set of H-H_2 collisional cross sections (cf. Allison and Dalgarno 1967), but no noticeable effects were found on the H_2 infrared spectra in the parameter regime considered.

g) *Thermal versus Fluorescent Excitation*

The final two models in Table 1, labeled S1 and S2, are strictly thermal distributions of H_2 at temperatures $T = 1000$ and $T = 2000$ K, respectively. They have been constructed to have column densities in $(v = 1, J = 3)$ identical with that in model 14, and thus identical (1, 0) $S(1)$ line intensities. Note that the total H_2 column densities required to produce this intensity in the (1, 0) $S(1)$ line are orders of magnitude smaller in the thermal models than in the fluorescent models. In Figure 9 the thermal spectra are compared with the fluorescent spectrum of model 14. The differences are quite striking. In the 2–2.5 μm region—the photometric K-band window—two major differences are apparent. First, lines involving vibrational levels $v \geq 2$, such as the (2, 1) $S(1)$ line at 2.25 μm and the (2, 1) $S(0)$ line at 2.36 μm, are virtually absent in the thermal spectra, whereas they are clearly visible in the fluorescent spectra; i.e., the vibrational populations of levels $v \geq 2$ due to fluorescent excitation can be characterized by a temperature $T_{\text{vib}} \approx 6000$–$9000$ K that is much larger than $T_{\text{vib}} = T = 2000$ K due to thermal excitation. Second, the rotational temperature in $v = 1$ is much higher in the thermal spectra, $T_{\text{rot}} = T = 2000$ K, than in the fluorescent spectra, where typically $T_{\text{rot}} \approx 400$–$1000$ K. Here T_{vib} is obtained by comparing the total column density in level v summed over all rotational levels with that in $v = 1$. The rotational temperature T_{rot} characterizing the population in level (v, J) is determined with respect to the population in level $(v, J - 2)$. The differences between thermal and fluorescent excitation are most easily recognized at low resolution, however, in the 1–2 μm region where almost no thermal line emission is seen. In this wavelength region, the fluorescent emission in transitions with $\Delta v = 2$ is as strong as in the $\Delta v = 1$ transitions that occur in the 2–2.5 μm region.

h) *Resonant Fluorescent Excitation by* H *Lyman-α*

Under some circumstances the ultraviolet radiation field may have an excess of photons in the vicinity of the H Lyα line at $\tilde{\nu}_\alpha = 82259.159$ cm^{-1} ($\lambda_\alpha = 1215.6701$ Å). For example, within an ionization-bounded H II region, the number of Lyα photons produced each second can be a large fraction of the total rate of recombinations to excited states of H and hence can be comparable to the total luminosity in ionizing photons of the central star (see, e.g., Draine and Salpeter 1978). Therefore, the flux of Lyα photons at the boundary of the H II region can be a significant fraction of the total flux of nonionizing ($\lambda > 912$ Å) photons. Moreover, this flux can remain large owing to resonant scattering into the neutral region over a line-center optical depth $\tau_{\text{H}} \approx 10^4$, which corresponds to $N(\text{H}) \approx 1.3 \times 10^{16} b_{\text{H}}$ cm^{-2}, where b_{H} is the Doppler broadening parameter in kilometers per second.

Gas heated by weakly ionizing shocks in the interstellar medium may cool predominantly by Lyα radiation. Hydrogen molecules formed somewhat farther into the cooling zone (cf. Hollenbach and McKee 1979) will then be exposed to large fluxes of Lyα radiation. In particular, shock-heated H_2 in equilibrium at $T = 2000$ K has fractional populations in levels $(v, J) = (2, 5)$ and $(2, 6)$ of 6.22×10^{-4} and 1.55×10^{-4}, respectively. Accidental resonances between the H_2 $B\,^1\Sigma_u^+$–$X\,^1\Sigma_g^+$ (1, 2) $P(5)$ and $R(6)$ lines at 1216.074 Å and 1215.731 Å, respectively, out of these levels and the Lyα line may lead to enhanced H_2 excitation rates through these transitions.

In order to explore the effects of enhanced Lyα radiation on the excitation of H_2, we have incorporated a Gaussian Lyα profile,

$$\phi_\nu^\alpha = \phi_0^\alpha \exp\{-1.686 \times 10^5[(\lambda - \lambda_\alpha)/\Delta V]^2\} \text{ cm}^{-2}\text{ s}^{-1}\text{ Hz}^{-1} , \tag{18}$$

into the adopted interstellar radiation field. The full width at half-maximum of this profile, ΔV, is in kilometers per second. As discussed below (§ IV*e*), real Lyα profiles with central reversals and Lorentzian wings are unlikely to be Gaussian in shape. The peak flux is specified in terms of a parameter,

$$\alpha = 310.5 \phi_0^\alpha \Delta V / I_{\text{UV}} , \tag{19}$$

which is the ratio of the integrated Lyα flux, $\int \phi_\nu^\alpha d\nu$, to the integrated continuum flux, $\int \phi_\nu d\nu = 2.82 \times 10^7 I_{\text{UV}}$ cm^{-2} s^{-1}, of the reference interstellar radiation field in the wavelength region $\lambda = 912$–1110 Å. At the boundary of an H II region, for example, the line width of escaping Lyα photons is expected to be 3–4 times the thermal linewidth at $T \approx 10^4$ K ($\Delta V \approx 64$ km s^{-1}). According to Draine and Salpeter (1978), the mean H Lyα flux in the interstellar background may be as high as $\int \phi_\nu^\alpha d\nu \approx 10^7$ cm^{-2} s^{-1}, which corresponds to $\alpha \approx 0.35/I_{\text{UV}}$. Table 5 lists the H_2 lines that are closest (within 27.5 cm^{-1}, or approximately 100 km s^{-1} in Doppler velocity) to exact resonance with H Lyα, along with their oscillator strengths and their total absorption rates, $k^d + k^{\text{ex}}$, at the boundary of model 29. The wavelengths of these H_2 lines are derived from the $X\,^1\Sigma_g^+$ energy levels discussed above and the spectroscopic constants for the $B\,^1\Sigma_u^+$ and $C\,^1\Pi_u$ given by Dabrowski (1984) and Namioka (1964). The wavelengths for P- and R-branch lines of the C–X Werner system are inaccurate owing to the lack of well-determined spectroscopic constants for the Π^+ Λ-components of the C state. Where available, wavelengths derived from measured energy levels are also tabulated. Shull (1978*b*) has previously listed the approximate resonances with H_2 lines that arise in $v'' = 1$, 2, and 3 and that lie within 400 cm^{-1} ($\Delta V \leq 1400$ km s^{-1}) of Lyα, whereas Table 5 lists the closest resonances only, but for a larger range of vibrational states.

All models listed in Table 1 have $\alpha = 0$, except for model 29, for which $\alpha = 1.0$. Comparison of integrated properties of models 28 and 29, which differ only in the value of α, reveals few large differences, as indicated in Table 6. This table lists Lyα absorption rates and column densities for some levels that are affected significantly and slightly by the resonant excitation in model 29 and compares those column densities with the corresponding ones in model 28. The table also presents the inverse lifetimes, A_{vJ}, of the levels considered. As might be expected, for $k^d + k^{\text{ex}} > A_{vJ}$, the effect of Ly$\alpha$ resonant excitation on level populations is noticeable; otherwise, the effect is small. The effect is typically a depletion of the population of the levels out of which the ultraviolet absorption occurs. The accompanying enhancement of populations of other nearby levels is very small because it is spread over a large number

TABLE 5

ACCIDENTAL RESONANCES BETWEEN H LYMAN-α AND H_2 LINES

Transition	λ^a (Å)	$f_{v'J',v''J''}$	$k^d + k^{ex}$ (s^{-1})	λ^b (Å)
B-X (1, 2) P(5)	1216.0741	2.87(-2)	1.3(-7)	1216.0723
B-X (1, 2) R(6)	1215.7293	3.40(-2)	4.1(-5)	1215.7314
B-X (3, 3) R(1)	1215.5429	2.35(-3)	1.7(-6)	1215.5442
B-X (6, 4) P(1)	1215.8817	3.61(-4)	8.3(-8)	1215.8829
C-X (0, 4) P(8)	1215.9460	4.13(-3)	2.7(-7)	1215.5248
C-X (1, 4) P(14)	1215.4093	2.77(-2)	2.5(-6)	
B-X (9, 5) P(1)	1215.6412	1.56(-4)	2.1(-7)	1215.6417
B-X (9, 5) R(2)	1215.9044	2.82(-4)	4.3(-8)	1215.9051
B-X (10, 5) R(6)	1215.3918	2.97(-3)	1.9(-7)	1215.6909[c]
C-X (1, 5) Q(6)	1215.5548	3.03(-2)	2.5(-5)	1215.5562
B-X (16, 5) R(14)	1215.5337	4.75(-4)	3.1(-7)	
B-X (13, 6) P(5)	1215.7872	1.46(-3)	1.2(-6)	1215.7897
B-X (15, 6) P(9)	1215.3485	4.24(-3)	1.0(-7)	
B-X (16, 6) R(11)	1215.8727	4.59(-3)	1.2(-6)	
C-X (3, 6) Q(11)	1215.4875	4.12(-2)	1.5(-5)	
C-X (3, 6) R(13)	1215.5000	2.29(-2)	1.0(-5)	
B-X (15, 7) R(0)	1215.5290	1.01(-4)	6.3(-8)	1215.5272
B-X (17, 7) P(7)	1215.6754	2.05(-3)	2.9(-6)	
C-X (4, 7) Q(8)	1215.4983	1.97(-2)	8.4(-6)	1215.4505
C-X (4, 7) R(10)	1215.4120	1.12(-2)	1.1(-6)	
C-X (5, 7) Q(14)	1215.6028	2.28(-2)	2.7(-5)	
C-X (5, 8) R(6)	1215.6414	3.74(-3)	5.1(-6)	
B-X (22, 8) P(10)	1215.6703	2.38(-3)	3.3(-6)	
B-X (22, 9) P(4)	1215.6015	2.95(-4)	3.4(-7)	1215.6123[d]
C-X (7, 9) P(8)	1215.9694	7.39(-3)	2.9(-7)	
B-X (24, 9) R(9)	1215.8589	1.45(-3)	4.8(-7)	
C-X (7, 9) R(11)	1215.4678	1.01(-2)	2.7(-6)	
C-X (8,10) P(5)	1215.9899	3.89(-3)	9.7(-8)	1215.8136
B-X (27,10) R(9)	1215.8365	9.10(-4)	4.2(-7)	
C-X (9,10) Q(13)	1216.0584	1.15(-2)	6.8(-8)	
C-X (9,11) R(0)	1215.5861	1.01(-2)	1.1(-5)	1215.5582
C-X (9,11) R(1)	1215.3679	5.05(-3)	1.9(-7)	1215.3027
C-X (9,11) R(2)	1215.4145	4.04(-3)	4.1(-7)	1215.3146
C-X (9,11) R(3)	1215.7152	3.60(-3)	4.7(-6)	1215.5987
B-X (28,11) P(4)	1215.6213	1.31(-4)	1.7(-7)	1215.600[d]
B-X (30,11) R(9)	1215.9468	5.28(-4)	3.4(-8)	
B-X (32,11) P(11)	1215.8713	6.47(-4)	1.8(-7)	
C-X (10,11) Q(11)	1216.0441	8.90(-3)	6.8(-8)	
B-X (30,12) R(0)	1215.5548	5.44(-5)	4.5(-8)	1215.552[d]
B-X (32,12) P(7)	1215.5869	1.66(-4)	1.8(-7)	
C-X (11,12) P(7)	1215.4120	2.28(-3)	2.2(-7)	
B-X (33,12) R(9)	1215.5405	2.36(-4)	1.7(-7)	
C-X (11,12) Q(9)	1215.3529	5.70(-3)	1.5(-7)	
B-X (34,12) R(10)	1215.4440	2.31(-4)	4.1(-8)	
C-X (12,13) P(5)	1215.5788	1.73(-3)	1.7(-6)	
C-X (12,13) Q(7)	1215.2928	4.77(-3)	3.4(-8)	

[a] Wavelength in vacuum computed from adopted molecular constants; values for *C–X P*- and *R*-branches are inaccurate.

[b] Wavelength in vacuum computed from observed energy levels of Dabrowski 1984.

[c] The upper level of this transition is strongly perturbed, thus accounting for the large discrepancy with the wavelength computed from constants.

[d] Wavelength in vacuum computed from observed energy levels of Dabrowski 1984 and of Namioka 1964.

of levels. The levels most severely affected will be $(v, J) = (2, 6)$ and $(5, 6)$. The observable consequences will appear most readily in the $S(3)/S(4)$ line intensity ratios of the (2, 1), (2, 0), (5, 3), and (5, 2) bands at 2.0, 1.1, 1.3, and 0.9 μm: the predicted values of these intensity ratios are, respectively, 2.9, 2.6, 2.6, and 2.4 for model 28, and 20, 18, 6.9, and 6.3 for model 29. These intensity ratios could, in principle, be used as a measure of α.

The effects of Lyα excitation discussed above are likely to have been somewhat overestimated because the subtleties of radiative transfer in the H Lyα line have been neglected. Indeed, as pointed out by Shull (1978*b*), some of the closest resonances may be quite ineffective if the intrinsic Lyα profile has a deep self-reversal. Another factor that may be important, especially in the case of a strong shock, is a large systematic difference in radial velocity between the Lyα emitting region and the H_2 fluorescence region. There is also a resonance between H_2 $B\ ^1\Sigma_u^+ – X\ ^1\Sigma_g^+$ (6, 0) $P(1)$ ($\lambda = 1025.9348$ Å) and H Lyβ ($\lambda = 1025.7223$ Å) that involves the ground state of ortho-H_2 and that may be important in some circumstances (cf. Feldman and Fastie 1973). Under most conditions considered in this paper, H Lyβ photons are so likely to have been removed by H absorption and converted into Lyα plus Hα that the possibility of an enhanced radiation field at $\lambda = 1025.7$ Å can be ignored. Resonant fluorescent excitation by emission lines of

TABLE 6

EFFECTS OF LYMAN-α RESONANT EXCITATION

(v, J)	$k^d + k^{ex}$ (s^{-1})	A_{vJ} (s^{-1})	Model 28 $N_{vJ}(H_2)$ (cm^{-2})	Model 29 $N_{vJ}(H_2)$ (cm^{-2})
(2, 5).........	1.3(−7)	1.55(−6)	2.53(14)	2.47(14)
(2, 6).........	4.1(−5)	1.50(−6)	8.65(13)	1.24(13)
(5, 1).........	2.1(−7)	3.71(−6)	1.29(14)	1.27(14)
(5, 6).........	2.5(−5)	3.65(−6)	1.90(13)	7.06(12)
(11, 0)........	1.1(−5)	4.59(−6)	6.07(12)	4.03(12)
(11, 1)........	1.9(−7)	4.60(−6)	2.26(13)	2.29(13)
(6, 5).........	1.2(−6)	4.33(−6)	3.60(13)	3.23(13)
(6, 11)........	1.6(−5)	3.36(−6)	8.64(12)	1.64(12)
(6, 13)........	1.0(−5)	3.00(−6)	6.76(12)	6.25(12)

other species, such as N II, N III, and O VI (Shull 1978*b*), has been ignored here, although it might be important near strong shocks. A specific case of combined excitation by shock heating and ultraviolet radiation with a strong Lyα component is discussed in § IV*e* below.

IV. DISCUSSION

a) The Reflection Nebula NGC 2023

The most striking example of a radiatively excited H_2 emission spectrum published so far is the infrared spectrum of the reflection nebula NGC 2023 (Gatley and Kaifu 1987; Sellgren 1986). Gatley *et al.* (1987) presented low-resolution spectra of the H_2 line emission of NGC 2023 between 1.5 and 2.5 μm, and Hasegawa *et al.* (1987) measured accurately the strengths of about 10 individual H_2 lines at higher resolution, $R \approx 3000$, in the 2–2.5 μm region. The strengths of the (2, 1) and (3, 2) lines relative to those of the (1, 0) lines, the presence of strong H_2 line emission at $\lambda = 1.5$–1.8 μm, and vibrational excitation temperatures that exceed the rotational temperatures all support the attribution of these spectra to the ultraviolet excitation mechanism (cf. § III*g*). The strongest H_2 emission is concentrated in a shell several arcminutes in extent and approximately centered on the exciting star of the visible nebula. The brightest concentration of this emission coincides with the outer edge of the infrared continuum radiation and lies just interior to a rim of CO $J = 1$–0 line emission at radial velocities $V_{LSR} = 10$–11 km s^{-1} (Gatley *et al.* 1987). Other observational data that indicate an interaction between ultraviolet starlight and a fairly dense neutral cloud are the emission in the $2p^2\,{}^2P_{3/2}$–${}^2P_{1/2}$ line of [C II] at $\lambda = 158$ μm (Crawford *et al.* 1985) and emission in several microwave lines of C I (Knapp, Brown, and Kuiper 1975; Pankonin and Walmsley 1976, 1978). It is significant that the C I lines show components at $V_{LSR} = +10$, $+11$ km s^{-1}, the same radial velocities that characterize the CO line emission associated morphologically with the H_2 emission.

Before constructing models of the H_2 emitting region, it is useful first to consider some constraints on the physical conditions in the cloud given by the observations of other species. The extremely small line widths, $\Delta V \approx 0.7$ km s^{-1}, of the C I lines imply a low upper limit on the kinetic temperature of $T < 130$ K (Pankonin and Walmsley 1976). Because this radio line emission may arise predominantly in the smallest, densest, coldest concentrations within the large antenna beams (2ʹ.6 or worse), the presence of warmer atomic and molecular gas cannot be excluded by these observations alone. However, observations of the lowest three rotational transitions in CO give antenna temperatures $T_A^* \approx 30$–40 K, from which excitation temperatures $T_{ex} \approx 39$–51 K are inferred (White, Phillips, and Watt 1981). It is therefore unlikely that the kinetic temperature of the molecular gas associated with NGC 2023 is much less than $T \approx 40$ K, or much more than $T \approx 130$ K.

The models also require an estimate of the ultraviolet flux in the vicinity of HD 37903, the exciting star of NGC 2023. This star is classified B1.5 V and has a measured flux at Earth of $f_\lambda = 3 \times 10^{-11}$ ergs s^{-1} cm^{-2} Å^{-1} at $\lambda = 1300$ Å (Massa, Savage, and Fitzpatrick 1983). The extinction at this wavelength is $A_\lambda \approx 3.0$ mag. The intrinsic flux distribution of this star can be assumed to be similar to that of a $T_{eff} = 22{,}500$ K, $\log g = 4.0$ model atmosphere (Kurucz 1979). On this basis, a reference flux at Earth at $\lambda = 1000$ Å of $f_\lambda = 5 \times 10^{-10}$ ergs s^{-1} cm^{-2} Å^{-1} is adopted. The peak of the H_2 emission is located 80ʺ in projection away from the star; if this is taken to be the true separation between the molecular gas and the star, and if the distance to NGC 2023 is taken to be 450 pc (Witt, Schild, and Kraiman 1984), an unattenuated flux $\phi(\lambda = 1000\ \text{Å}) = 5.6 \times 10^{-5}$ photons s^{-1} cm^{-2} Hz^{-1} at the cloud boundary is inferred. This flux corresponds to $I_{UV} = 1240$ in the standard background radiation field. The wavelength dependence of the radiation field of a B1.5 V star is slightly different from that of the standard interstellar radiation field. To test the influence of this difference, cloud models have been computed with the standard radiation field at $I_{UV} = 1240$ and with a radiation field given by the stellar model mentioned above. Because the wavelength dependences of the photon flux in the $\lambda = 912$–2000 Å region are rather similar in the two cases, no significant variations in the computed H_2 spectra are found. The Lyα contribution to the ultraviolet radiation field from a small H II region around HD 37903 can be estimated according to the prescription that 70% of all recombinations to levels $n \geq 2$ in H produce Lyα photons (Draine and Salpeter 1978). The integrated flux of H-ionizing photons in the above stellar model can be written as $\Phi = 1.1 \times 10^5 I_{UV}$ cm^{-2} s^{-1}, which implies a small value of the Lyα flux parameter: $\alpha = 3.2 \times 10^{-3}$ (cf. § III*h*). In summary, the ultraviolet radiation field responsible for exciting H_2 is given by $I_{UV} \lesssim 1240$, with no significant Lyα contribution.

A "good" model of the NGC 2023 cloud is expected (1) to reproduce the intensities of the strongest H_2 lines measured at high spectral resolution at the position of brightest emission (Hasegawa *et al.* 1987), (2) to fit well the detailed appearance of the

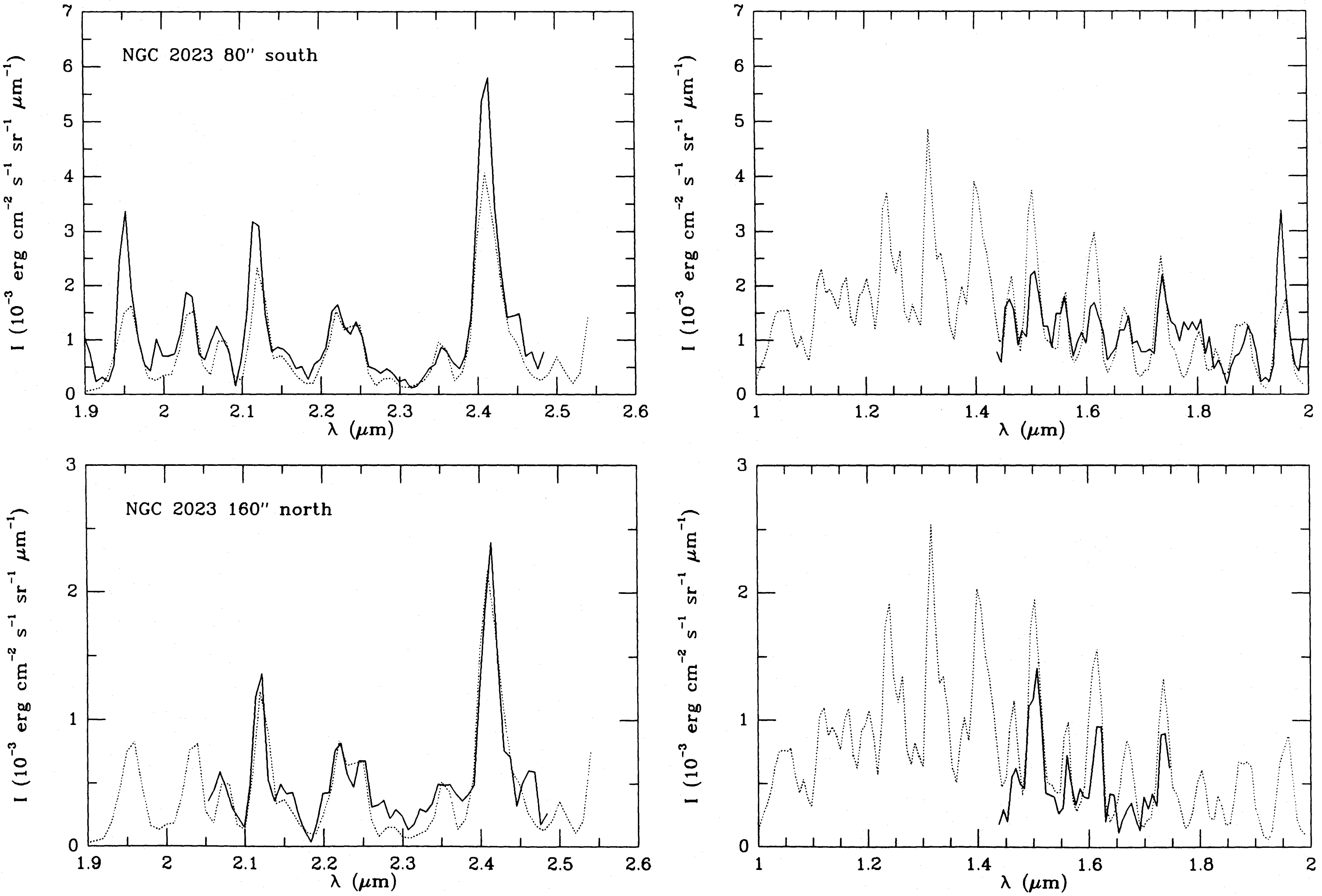

FIG. 10.—Comparison of observed and theoretical spectra for two positions in NGC 2023. The solid curves represent the observational data of Gatley *et al.* (1987), adjusted for a continuum contribution (see text). The dotted curves represent the theoretical spectra for the models described in the text at a resolving power of $\lambda/\Delta\lambda \approx 100$. Note that the observational data are affected by bad atmospheric transmission at $\lambda = 1.8$–$2.0\ \mu$m.

1987ApJ...322..412B

low-resolution spectra at two positions in the cloud (Gatley *et al.* 1987), and (3) to be in harmony with the other observational constraints. The low-resolution spectrum obtained 80″ south of the star is represented well by theoretical spectra derived from models with uniform densities and temperatures $n_H = 10^4$ cm^{-3} and $T = 80$ K, and $I_{UV} = 300$, when grain model 3 and $y_f = 3$ are assumed. Gatley *et al.* (1987) also measured part of the H_2 spectrum 160″ north of the star. This spectrum can be fitted well with the same models, but with I_{UV} reduced to 130. Figure 10 illustrates the good agreement between the theoretical models and the data of Gatley *et al.* (1987) at the two positions. The temperature of 80 K was determined mainly by the relative strengths of the observed (1, 0) $S(1)$, (1, 0) $S(0)$, and (2, 1) $S(1)$ lines. The uncertainties in the observations allow a range in temperature of 40–120 K. Given $T = 80$ K, the combination of parameters $I_{UV}/n_H y_f$ was constrained to be about 0.01 at the 80″ south position by the measured absolute line intensities (cf. Table 4). Similar models with lower densities, $n_H = 3 \times 10^3$ cm^{-3}, also fit the data well, but require scaling factors for the radiation field $I_{UV} \approx 5000$ that are inconsistent with the known ultraviolet flux of HD 37903. Models with higher densities, $n_H = 3 \times 10^4$ cm^{-3}, can reproduce the 80″ south data equally well if either a less intense field, $I_{UV} \approx 240$, is employed, or a smaller H_2 formation efficiency on grains, $y_f \approx 1$. When the less forward-scattering grain model 2 is adopted, both the density, $n_H \approx 3 \times 10^4$ cm^{-3}, and the intensity of the radiation field, $I_{UV} \approx 10^4$, must be higher to account for the observed H_2 line intensities. As mentioned before, such intense radiation fields are inconsistent with the ultraviolet flux of HD 37903. The ratio of the inferred fluxes at the 80″ south and 160″ north positions is somewhat smaller than would be expected for a homogeneous cloud with projected distances equal to the true separations for the star. On the other hand, the deviation is small enough that it can easily be caused by density variations in the cloud, or by projection effects for which there is a slightly larger true separation at the 80″ south position. CCD pictures at various near-infrared wavelengths (Witt and Schild 1986) indicate indeed that the NGC 2023 cloud is highly inhomogeneous.

The model spectra presented in Figure 10 were computed using H_2 formation model $\varphi = 1$. In Figure 11, model spectra using formation models $\varphi = 2$ (*top*) and $\varphi = 3$ (*bottom*) are compared with the observational data of Gatley *et al.* (1987) at the 80″ south position. Formation model $\varphi = 2$ results in somewhat larger absolute infrared intensities, but the fit to the observed relative strengths is not significantly worse than with model $\varphi = 1$. It is clear that formation models 1 and 2 provide much better fits to the data than model $\varphi = 3$. Model $\varphi = 3$ with a low formation temperature $T_f = 15$ K produces relatively too much para-H_2 (even J), resulting in (1, 0) $S(0)$ and (2, 1) $S(0)$ lines that are too strong, for example. If the formation temperature is increased to $T_f = 65$ K, the fit to the observed spectrum is better in the 2–2.5 μm region, but not between 1.5 and 2 μm. In particular, model $\varphi = 3$ results in much too high intensities in the (6, 4) $O(2)$ line at 1.67 μm, because all newly formed H_2 molecules enter $v = 6$ in this model. The fact that none of the observed $\Delta v = 2$ transitions between 1.45 and 2 μm has a significantly enhanced intensity indicates that the H_2 molecules are most likely not formed in any *specific* vibrational level with $v = 4$–7.

The comparison of computed line intensities with the high-resolution measurements of Hasegawa *et al.* (1987) at the 80″ south position is presented in Table 7 for various models with different prescriptions of the H_2 formation process. The high-resolution measurements in the 2–2.5 μm region do not permit more accurate constraints on the H_2 formation models. The table includes the population ratios relative to the population in $v = 1$, $J = 2$ as derived from observations and as obtained from theory. For comparison, the theoretical results of Takayanagi, Sakimoto, and Onda (1987) are indicated as well. The observed relative line intensities imply a ratio of ortho-H_2 (odd J) to para-H_2 (even J) of 1.4–2, which is lower than the statistical ratio of 3. Takayanagi *et al.* and Hasegawa *et al.* attributed this finding to a low formation temperature $T_f \approx 60$–70 K. In the model of Takayanagi *et al.*, all H_2 molecules are formed in the $v = 0$ level with $T_f = 60$ K. As pointed out in § II, other factors that affect the rotational population distributions in general and the ortho/para ratio in particular include the interchange reaction

$$H^+ + H_2(v = 0, J = 0, 2, 4, \ldots) \leftrightarrows H_2(v = 0, J = 1, 3, 5, \ldots) + H^+ \tag{20}$$

(see eq. [1]). In the outermost layers of our model clouds, photoionization of excited $H_2(v \geq 4)$ at $\lambda > 912$ Å followed by photodissociation of the product H_2^+ is the principal source of H^+ and can maintain higher proton densities than cosmic-ray ionization. This source of ionization decreases in importance rapidly with increasing depth, where cosmic-ray ionization becomes dominant. Thus both the proton density, and the rates of formation, destruction, and excitation with which the interchange reaction (20) competes, are found to vary significantly with depth in the models. Takayanagi, Sakimoto, and Onda (1987) did not perform depth-dependent calculations but used a total H_2 excitation rate $\bar{k}^{ex} \approx 3 \times 10^{-8}$ s^{-1}. Our calculations show that $\bar{k}^{ex} \approx 2 \times 10^{-7}$ s^{-1} at the boundary of the cloud, decreasing to $\bar{k}^{ex} \approx 5 \times 10^{-10}$ s^{-1} at the depth z_{max} where the H_2^* density is maximal. At any particular depth, the excitation rate is very level-specific. For example, at z_{max} it ranges from 10^{-10} s^{-1} for odd J to 5×10^{-8} s^{-1} for even J. Thus the use of one excitation rate for all levels without consideration of the depth dependence does not appear to be realistic. Table 7 includes a model, model E, in which the H_2 molecules are formed in $v = 0$ with $T_f = 65$ K. As the table shows, the results do not differ significantly from those of models A and B, where the ortho/para ratio upon formation is equal to 3. Thus the present models do not require $T_f \leq 65$ K with formation in a specific v level in order to reproduce the low ortho/para ratio, in contrast with the calculations of Takayanagi, Sakimoto, and Onda (1987). The differing conclusions evidently result from the higher proton abundance and the larger effects of explicit depth variations of level populations in the present models. A formation temperature as low as $T_f = 15$ K is clearly excluded by the observations.

Although most models in Table 7 reproduce both high- and low-resolution spectra to better than a factor of 2, not all details of the H_2 observations are represented perfectly in any one model. In particular, all models fall short of accounting for the intensities of the (1, 0) S and Q lines measured 80″ south of the star by up to a factor of 2 when I_{UV} is fixed such that the computed (2, 1) and (3, 2) line intensities agree with observations. The intensities of the S lines are rather well determined observationally, except for the (1, 0) $S(3)$ line, which lies in a region of bad atmospheric transmission. The models also underestimate the $J = 5$ column density in $v = 2$ and $v = 3$, resulting in (2, 1) $S(3)$ and (3, 2) $S(3)$ intensities at the 80″ south position that are too low. On the other hand, the models appear to reproduce well the observed (1, 0) S and Q line intensities at the 160″ north position. In the 1.4–2 μm region, the models seem to fit well the low-resolution data at both positions for the (6, 4), (5, 3), (4, 2) and (3, 1) $O(2)$ and $O(4)$ lines, but they give overly strong (6, 4), (5, 3) and (4, 2) $O(3)$ and Q blends, particularly at the 80″ south position. Thus the theoretical models need to produce

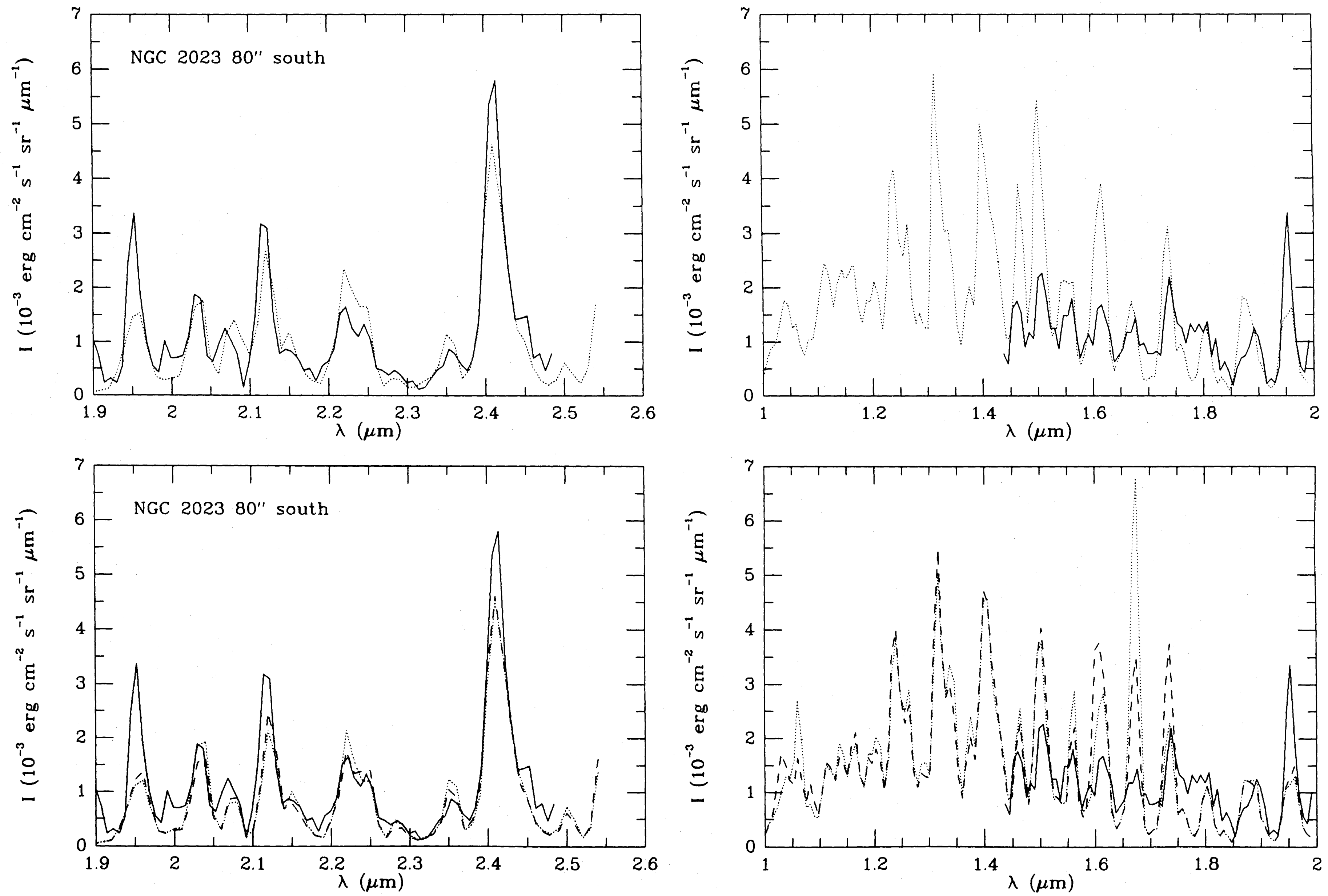

FIG. 11.—Comparison of observed and theoretical spectra of NGC 2023 for different H_2 formation models. The solid curves represent the observed spectra at the 80″ south position as in Fig. 10. *Upper panels*: The dotted curves are for the appropriate model with $\varphi = 2$. *Lower panels*: The dotted curves are for the appropriate model with $\varphi = 3, T_f = 15$ K, and the dashed curves are for $\varphi = 3, T_f = 65$ K. A low formation temperature is evidently excluded.

TABLE 7

COMPARISON OF COMPUTED H_2 INFRARED LINE INTENSITIES[a] AND POPULATION RATIOS[b] WITH OBSERVATIONS FOR NGC 2023 CLOUD

Line or Upper Level	Observed[c]	Model A[d]	Model B[e]	Model C[f]	Model D[g]	Model E[h]	Model F[i]	Model G[j]	Model H[k]	Takayanagi *et al.*[l]
(1,0) S(0)	(3.67±0.3)	2.21	2.37	3.22	2.58	2.15	1.98	3.34	3.23	
(1,0) S(1)	(7.76±0.3)	3.53	4.08	3.20	3.84	3.14	4.49	7.76	7.28	
(1,0) S(2)	(3.24±0.2)	2.02	2.10	2.79	2.22	1.85	2.15	3.17	3.09	
(2,1) S(0)	(1.13±0.3)	1.23	1.35	1.79	1.44	1.21	1.10	1.23	1.52	
(2,1) S(1)	(2.12±0.3)	1.88	2.25	1.73	2.12	1.69	2.38	1.88	2.44	
(2,1) S(2)	(1.55±0.2)	1.03	1.10	1.59	1.21	0.95	1.11	1.03	1.44	
(2,1) S(3)	(1.69±0.2)	0.94	0.95	0.71	0.85	0.68	1.29	0.94	1.44	
(3,2) S(1)	(0.85±0.4)[c] (0.56±0.5)[c]	0.97	1.20	0.90	1.10	0.88	1.23	0.97	1.26	
(3,2) S(2)	(0.42±0.3)	0.51	0.55	0.76	0.59	0.47	0.56	0.51	0.72	
(3,2) S(3)	(0.85±0.2)	0.44	0.46	0.34	0.39	0.32	0.61	0.44	0.69	
$v'=1$ $J'=2$	1.00	1.00	1.00	1.00	1.00	1.00	1.00	1.00	1.00	1.00
3	(1.50±0.15)	1.11	1.19	0.69	1.04	1.02	1.57	1.62	1.57	1.50
4	(0.53±0.05)	0.54	0.51	0.50	0.50	0.50	0.63	0.55	0.56	0.55
$v'=2$ $J'=2$	(0.23±0.10)	0.42	0.41	0.40	0.41	0.41	0.40	0.27	0.34	0.41
3	(0.30±0.05)	0.45	0.49	0.28	0.42	0.40	0.62	0.29	0.39	0.61
4	(0.19±0.03)	0.21	0.20	0.22	0.21	0.19	0.25	0.13	0.20	0.22
5	(0.19±0.03)	0.18	0.16	0.09	0.14	0.13	0.27	0.12	0.18	0.20
$v'=3$ $J'=3$	(0.12±0.10)	0.23	0.27	0.15	0.23	0.22	0.33	0.15	0.21	0.33
4	(0.05±0.05)	0.11	0.11	0.11	0.11	0.10	0.13	0.07	0.10	0.11
5	(0.10±0.04)	0.09	0.09	0.05	0.07	0.07	0.14	0.06	0.09	0.10

[a] In units of 10^{-5} ergs s^{-1} cm^{-2} sr^{-1}.

[b] The lower part of the table lists the ratio of the column density in upper level v', J' of the observed transitions with respect to level $v' = 1$, $J' = 2$.

[c] Observations of Hasegawa *et al.* 1987, 80″ south of HD 37903. Note that two features separated by only 0.001 μm are observed near the wavelength $\lambda = 2.386$ μm of the (3, 2) $S(1)$ line. It is not clear which of the two features should be identified with the (3, 2) $S(1)$ line, or what the identification of the other line is. No other H_2 infrared line with $J \leq 15$ lies within 0.003 μm of the (3, 2) $S(1)$ line. We assume that the stronger of the two features corresponds to the (3, 2) $S(1)$ line.

[d] All models have $n_H = 10^4$ cm^{-3}, $T = 80$ K, $I_{UV} = 300$, grain model 3, $y_f = 3$, and H_2 formation model $\varphi = 1$, unless indicated otherwise.

[e] $\varphi = 2$.

[f] $\varphi = 3$ and $T_f = 15$ K.

[g] $\varphi = 3$ and $T_f = 65$ K.

[h] Specific formation into $v = 0$ with $T_f = 65$ K.

[i] As model A, but with varying temperature and density with depth; $T \approx 400$ K at the boundary.

[j] Model A + thermal emission from $N(H_2) = 2 \times 10^{18}$ cm^{-2} at $T = 1000$ K.

[k] Model A + thermal and fluorescent emission from $N(H_2) = 2 \times 10^{18}$ cm^{-2} at $T = 1000$ K.

[l] Theoretical results of Takayanagi, Sakimoto, and Onda 1987 for $\bar{k}^{ex} = 3 \times 10^{-8}$ s^{-1}, $T_f = 60$ K, and $n_H = 10^4$ cm^{-3}.

more population in all levels of $v = 1$ and in the higher odd-J levels of $v = 2$ and $v = 3$ at the 80″ south position, but at the same time they should have lower populations in $J = 1$ for $v = 4$–6. It is possible to explain some of these discrepancies by adjusting the parameters in the fluorescent excitation models. One possible solution is to construct models with temperatures and densities that vary with depth. In particular, model F of Table 7, which has a temperature $T \approx 400$ K in the outer regions of the cloud, decreasing to $T = 50$ K in the center, provides higher rotational populations in $v = 1$–3. This specific model gives a somewhat too low (1, 0) $S(0)$ intensity, indicating that the warm zone in the model is somewhat too large. Such a temperature variation in the cloud is not unreasonable on theoretical grounds. Explicit calculations of the temperature structure in photodissociation regions (Sternberg 1986) indicate that for $n_H \approx 10^4$ cm^{-3} and $I_{UV} \geq 10^3$, the temperature at the boundary of the cloud is a few hundred degrees, decreasing to less than 100 K deeper in the cloud. Because the part of the cloud located 160″ north of the star is exposed to less intense radiation, its temperature at the outer boundary may be only slightly larger than 80 K, resulting in no significant enhancement of the $v = 1$ population. Alternatively, the relatively large measured populations in $v = 1$ at 80″ south could be produced by a small shocked region of the cloud at that position. As Table 7 indicates, a H_2 column density of 10^{18} cm^{-2} thermally excited at a temperature $T = 1000$ K would be required to explain the excess (1, 0) line emission. Simultaneous fluorescent excitation of this amount of hot gas can then also account for the larger populations in $J = 5$ of $v = 2$ and $v = 3$.

It thus appears that the H_2 measurements constrain the main parameters of the bulk of the molecular gas in NGC 2023, as well as certain properties of the grains, rather closely. For the reference model, we adopt model A of Table 7 with $n_H = 10^4$ cm^{-3}, $T = 80$ K, $y_f = 3$, grain model 3, $\varphi = 1$, and $I_{UV} = 300$ at the position 80″ south of the star. This model can be used to compare with other observational constraints and to predict additional measurable properties that can serve as tests of our theory. In this reference model, the total fluorescent intensity has converged to within 2% of its asymptotic limit, and the excited state density, $n(H_2)$ has fallen to 0.0056 times its maximum value at a depth into the cloud given by a column density $N(H_2) = 3.1 \times 10^{21}$ cm^{-2}. This corresponds to a depth from the boundary of 0.25 pc, or $A_V = 4.8$ mag. This is approximately the thickness of the layer responsible for the detectable H_2 emission. If seen in projection at the adopted distance for NGC 2023, $D = 450$ pc, this thickness would correspond to an angular dimension of 1′.9. The angular extent of the observed emission is similar. A slightly larger distance has been suggested (viz., $D = 575$ pc, by de Boer 1983), but this makes no significant difference for any derived parameters. The bulk of the molecular gas associated with NGC 2023 evidently lies beyond HD 37903 from our viewpoint (Harvey, Thronson, and Gatley 1980). The model was calculated to a total depth of 0.70 pc, or $A_V = 13.5$ mag. Into this depth, the carbon is still predominantly in atomic form, although the CO abundance is by then beginning to become appreciable, in agreement with the fact that the strongest CO emission is observed from a rim which lies just outside the H_2 emission. More details of the C, C^+, and CO abundances and their line emission from NGC 2023, as well as the HD excitation and fluorescent emission, will be given in Paper II.

The observed spectra almost certainly include a substantial amount of continuum radiation, as indicated by the broad-band measurements of Sellgren (1984). Accordingly, we have subtracted a continuum intensity of $I_\nu = 1.8$ mJy nsr^{-1} at the 80″ south position and $I_\nu = 0.26$ mJy nsr^{-1} at the 160″ north position before presenting the observed spectra in Figures 10 and 11.[3] The contribution of the H_2 lines to broad-band intensities can be calculated directly. The results for the reference model are given in Table 8 alongside the fluxes measured by Sellgren (1984) in a 12″ diameter beam at a position 60″ south of HD 37903. The integrated line intensity is a significant fraction of the observed broad-band emission in the *I*, *J*, and *H* bands and is less important at $\lambda \leq 0.7$ μm and at $\lambda \geq 2$ μm.

The models of NGC 2023 can be tested by searching for predicted H_2 lines at wavelengths outside the range observed so far. Table 9 contains predicted intensities for a few selected H_2 lines that lie outside the $\lambda = 1.5$–2.5 μm wavelength region covered by the low-resolution spectra of Gatley *et al.* (1987). Observations of the (1, 0) and (2, 1) *O*(2) and *O*(3) lines, which occur at $\lambda = 2.5$–3 μm, would be of particular interest, since they measure directly the $J = 0$ and $J = 1$ populations and thus the ortho/para ratio in $v = 1$–2. Measurements of the (0, 0) *S*(0) and *S*(1) lines would give direct information on the temperature in the outer part of the cloud. Both sets of observations would have to be performed above the stratosphere. The final column of the table presents the intensities expected on the basis of the (1, 0), (2, 1), and (3, 2) line intensities measured by Hasegawa *et al.* (1987) at the 80″ south position. It is useful to compare the predicted line intensities in the far-red part of the spectrum with the continuum brightness of the nebula. Witt, Schild, and Kraiman (1984) have measured comparable surface brightnesses in the *R* and *I* bands of $I_\nu \approx 0.5$ mJy nsr^{-1} in 14″.6 diameter areas at positions 112″ southeast and southwest of HD 37903. Both the reference model and the infrared line measurements of Hasegawa *et al.* (1987) imply an expected peak intensity in the (3, 0) *S*(3) line at 7960 Å that is $\geq 5.7(\text{Å}/\Delta\lambda)$ mJy nsr^{-1}, which will yield a line/continuum flux ratio of 1.0 or greater at a resolution of $\Delta\lambda \approx 11$ Å.

In summary, detailed models can be constructed of the surface of the molecular cloud associated with NGC 2023 that account for the observed H_2 line emission and that are also in harmony with other existing observations.

b) The Planetary Nebula NGC 7027

The planetary nebula NGC 7027 was one of the first detected sources of H_2 line emission. The emitting molecules appear to be concentrated just outside the ionized region, in a shell approximately 12″ in diameter (Beckwith *et al.* 1980). The relative intensities of the observed H_2 lines are represented quite well by thermal emission at $T \approx 1000$ K (Smith, Larson, and Fink 1981). This is a case, however, where the excited molecules must also be exposed to a substantial ultraviolet flux. The ultraviolet flux of the central star is rather well constrained, and a value of $I_{\rm UV} \approx 775$ is appropriate to describe its effect on H_2 near the ionization boundary, without allowance for internal extinction. The contribution of H Lyα can be estimated from the reddening-corrected Balmer line flux (Miller and Mathews 1972; Pottasch *et al.* 1982) and recombination theory: the result is $\alpha = 51$. The nebula is quite dense, and the neutral shell probably has $n_{\rm H} \gtrsim 10^5$ cm^{-3} in order to be close to pressure balance with the hotter, ionized gas. We have computed two models of this emitting region to illustrate the effects of additional radiative excitation on thermally excited H_2, as shown in Table 10. In the first case, the excitation is purely thermal with $T = 1000$ K and $N(H_2) = 6.6 \times 10^{19}$ cm^{-2}. The second case is a hybrid model in which the excitation is calculated for a uniform slab of the same temperature and H_2 column density, but

TABLE 8

CONTRIBUTION OF H_2 LINES TO BROAD-BAND FLUXES IN NGC 2023

Band	λ_0[a] (μm)	$\Delta\lambda$[a] (μm)	I_ν(model) (mJy nsr^{-1})[b]	I_ν(observed)[c] (mJy nsr^{-1})
R	0.70	0.21	0.040	0.51
I	0.88	0.21	0.169	0.47
J	1.26	0.20	0.909	1.7
H	1.60	0.36	0.864	3.4
K	2.22	0.52	1.063	4.9
L	3.54	0.97	0.493	15
M	4.80	0.60	0.206	9

[a] Nominal central wavelengths in the photometric systems discussed by Campins, Rieke, and Lebofsky 1985 for $\lambda > 1$ μm and by Johnson 1965 for $\lambda < 1$ μm.

[b] A nanosteradian (nsr) $= 10^{-9}$ sr is the solid angle subtended by a circular aperture 7″.36 in diameter; see text.

[c] Broad-band measurements of Sellgren 1984, 60″ south of HD 37903, except for *R* and *I* data that are the mean of intensities at 112″ southeast and 112″ southwest of HD 37903 measured by Witt, Schild, and Kraiman 1984.

---

[3] Note that convenient units for such specific intensities are mJy nsr^{-1} $= 10^{-17}$ ergs s^{-1} cm^{-2} Hz^{-1} sr^{-1}, where 1 nsr $= 10^{-9}$ sr is the solid angle subtended by a circular aperture 7″.36 in diameter.

TABLE 9

PREDICTED LINE INTENSITIES IN THE NGC 2023 REFERENCE MODEL

λ (μm)	Line	I^a	I^b
28.211	(0, 0) $S(0)$	$6.9(-6)^c$	...
17.030	(0, 0) $S(1)$	$4.8(-6)^c$	...
12.275	(0, 0) $S(2)$	$5.5(-6)^c$	...
3.003	(1, 0) $O(4)$	$1.9(-5)$	$3.1(-5)$
2.973	(2, 1) $O(3)$	$1.9(-5)$	...
2.802	(1, 0) $O(3)$	$3.3(-5)$	...
2.785	(2, 1) $O(2)$	$1.4(-5)$	...
2.626	(1, 0) $O(2)$	$2.3(-5)$	...
1.324	(3, 1) $Q(3)$	$1.1(-5)$	$0.8(-5)$
1.318	(3, 1) $Q(2)$	$1.2(-5)$	...
1.314	(3, 1) $Q(1)$	$1.8(-5)$	...
1.311	(4, 2) $S(1)$	$1.5(-5)$	...
1.262	(3, 1) $S(0)$	$1.1(-5)$	...
1.238	(2, 0) $Q(1)$	$1.4(-5)$	...
1.233	(3, 1) $S(1)$	$1.7(-5)$	$1.2(-5)$
1.207	(3, 1) $S(2)$	$9.9(-6)$	$8.0(-6)$
1.189	(2, 0) $S(0)$	$8.4(-6)$	$7.5(-6)$
1.185	(3, 1) $S(3)$	$9.4(-6)$	$1.9(-5)$
1.162	(2, 0) $S(1)$	$1.4(-5)$	$1.6(-5)$
1.138	(2, 0) $S(2)$	$8.2(-6)$	$1.3(-5)$
1.117	(2, 0) $S(3)$	$8.2(-6)$	$1.5(-5)$
1.030	(6, 3) $Q(1)$	$5.2(-6)$	...
0.988	(6, 3) $S(1)$	$5.1(-6)$	...
0.923	(5, 2) $S(1)$	$4.9(-6)$	...
0.911	(5, 2) $S(2)$	$3.0(-6)$	...
0.903	(4, 1) $Q(1)$	$3.1(-6)$	...
0.902	(5, 2) $S(3)$	$2.9(-6)$	...
0.866	(4, 1) $S(1)$	$3.7(-6)$	...
0.855	(4, 1) $S(2)$	$2.4(-6)$	...
0.846	(4, 1) $S(3)$	$2.4(-6)$	...
0.839	(8, 4) $S(1)$	$1.8(-6)$	...
0.815	(3, 0) $S(1)$	$1.9(-6)$	...
0.796	(3, 0) $S(3)$	$9.0(-7)$	$6.0(-7)$

[a] Intensities are in units of ergs s^{-1} cm^{-2} sr^{-1}.

[b] Intensities in the final column are those implied by the line measurements at longer wavelengths of Hasegawa *et al.* 1987, 80″ south of NGC 2023.

[c] In model F (cf. Table 7), which has $T \approx 400$ K at the boundary, the (0, 0) $S(0)$, $S(1)$, and $S(2)$ intensities are increased to $1.3(-4)$, $2.8(-3)$ and $7.6(-4)$ ergs s^{-1} cm^{-2} sr^{-1}, respectively.

with $I_{UV} = 775$, $\alpha = 51$, $n_H = 10^5$ cm^{-3}, and $y_f = 0.3$. The H_2 formation efficiency has been reduced in comparison with the models of § III because the hot grains present in and around NGC 7027 are likely to be less efficient at forming H_2 than normal interstellar grains, even though they may be more abundant. The $v = 0$ and $v = 1$ populations are held nearly thermalized at $T = 1000$ K in this second model by the inclusion of a constant effective rate coefficient, $k_v = 10^{-10}$ cm^3 s^{-1}, for all downward inelastic collisional processes involving $v = 1$ levels. The corresponding upward rate coefficients are evaluated in detailed balance. Comparison of observed (Smith, Larson, and Fink 1981) and calculated line fluxes for selected transitions in Table 10 shows that the purely thermal and thermal-plus-ultraviolet models are indistinguishable in terms of the *detected* (1, 0) lines. However, the intensities of lines arising in $v' = 2$ are enhanced by factors of the order of 3 by ultraviolet excitation, and the effects on transitions with $v' > 2$ are considerably larger. Even so, detection of the radiatively excited lines will be difficult although probably not impossible. For example, the calculated flux in the (4, 1) $S(3)$ line at $\lambda = 8459$ Å would yield a line-to-continuum ratio $I/(I_\nu \Delta\nu) = 0.24(3\ \mathrm{km\ s^{-1}}/\Delta V)$ at a velocity resolution ΔV, based on the unreddened continuum flux $I_\nu = 1.4$ Jy of Miller and Mathews (1972). The calculated spectra can also be used to show that the contribution of H_2 lines to the broad-band fluxes is less than 6% at K and is completely negligible in the other standard photometric bands. A different kind of model of the H_2 emission from NGC 7027, in which part of the molecules form by entirely gas-phase processes, has been discussed by Black, Porter, and Dalgarno (1981), although with a less elaborate treatment of the subsequent radiative excitation. In that model, the rotational excitation within the excited vibrational levels is predicted to be significantly higher than in the grain formation models. Observations of lines involving high-J levels might assess the relative importance of the two formation schemes.

TABLE 10

NGC 7027 H_2 LINE FLUXES

Line	λ (μm)	f(thermal)[a] (10^{-12} ergs s^{-1} cm^{-2})	f(thermal + UV)[a] (10^{-12} ergs s^{-1} cm^{-2})	f(observed)[b] (10^{-12} ergs s^{-1} cm^{-2})
(0, 0) $S(3)$	9.662	3.09	3.20	...
(1, 0) $O(5)$	3.234	1.46	1.49	...
(1, 0) $Q(5)$	2.454	0.90	0.91	<5
(1, 0) $Q(4)$	2.437	0.56	0.57	<1.3
(1, 0) $Q(3)$	2.423	2.60	2.65	2.4 ± 1.0
(1, 0) $Q(2)$	2.413	1.09	1.11	1.2 ± 1.0
(1, 0) $Q(1)$	2.406	3.86	3.92	3.5 ± 1.1
(2, 1) $S(1)$	2.247	0.019	0.048	<0.9
(1, 0) $S(0)$	2.223	0.99	1.01	1.0 ± 0.8
(1, 0) $S(1)$	2.121	3.70	3.77	3.7 ± 1.0
(2, 1) $S(3)$	2.073	0.0096	0.038	<0.5
(1, 0) $S(2)$	2.033	1.01	1.03	0.9 ± 0.5
(7, 5) $O(3)$	1.872	5.1(−12)	0.024	...
(8, 6) $S(1)$	1.764	1.3(−13)	0.013	...
(5, 3) $S(1)$	1.400	2.2(−8)	0.046	...
(4, 2) $S(1)$	1.311	1.8(−6)	0.049	...
(4, 2) $S(3)$	1.261	1.2(−6)	0.041	...
(3, 1) $S(1)$	1.233	1.7(−4)	0.049	...
(2, 0) $S(1)$	1.162	0.014	0.035	...
(6, 3) $S(1)$	0.988	1.8(−10)	0.022	...
(5, 2) $S(1)$	0.923	8.7(−9)	0.018	...
(4, 1) $S(3)$	0.846	3.6(−7)	0.012	...
(3, 0) $S(1)$	0.815	1.9(−5)	5.5(−3)	<0.5[c]

[a] The flux $f = I\Omega$, where $\Omega = 2.66$ nsr (angular diameter of 12″).

[b] The observed flux corrected for extinction is that of Smith, Larson, and Fink 1981 unless otherwise indicated.

[c] The observed limit is from Traub, Carleton, and Black 1978. Note that flux levels 540 times smaller were achieved with the same instrument toward other sources.

c) The Galactic Center

The H_2 line emission from the Galactic center has received considerable attention (Gatley *et al.* 1984; Gatley *et al.* 1986). The emission is strong, and the lines are quite broad: $\Delta V \approx 100$–150 km s^{-1} after correction for the resolution of the spectrometer (Gatley *et al.* 1986). Although this emission may be dominated by thermally excited molecules, the source of ultraviolet radiation in the Galactic center is quite luminous and its contribution to the excitation can be estimated. The data and analysis of Geballe *et al.* (1984) imply an ultraviolet source of effective temperature $T_{\rm eff} \approx 30{,}000$–$35{,}000$ K, with a total luminosity in ionizing photons of $L_{\rm ion} \approx 10^{49}$–$10^{50}$ s^{-1} in the direction of IRS 16. For a model stellar atmosphere with $T_{\rm eff} = 35{,}000$ K, $L_{\rm ion} = 4 \times 10^{49}$ s^{-1} will be accompanied by a luminosity in $\lambda = 912$–1110 Å photons of $L_{\rm UV} = 1.5 \times 10^{50}$ s^{-1} (cf. Black *et al.* 1980). The diameter of the H_2-emitting ring around IRS 16 is approximately $1'.3$ (Gatley *et al.* 1984, 1986). If this is taken to describe the dilution of radiation from the central source, then a value of $I_{\rm UV} = 1.5 \times 10^4$ can be inferred for the photons effective in exciting H_2. If ionized gas at $T = 10^4$ K uniformly fills a sphere of radius 1.7 pc, then the thermal gas pressure can be balanced approximately by neutral gas with $T \approx 10^3$ K and $n_{\rm H} \approx 10^4$ cm^{-3} at the boundary. The peak observed surface brightness in the (1, 0) $S(1)$ line is 2.0×10^{-4} ergs s^{-1} cm^{-2} sr^{-1} (Gatley *et al.* 1986), which gives $I[(1, 0)\ S(1)] \approx 3.3 \times 10^{-3}$ ergs s^{-1} cm^{-2} sr^{-1} after correction for the $A_\lambda = 3.0$ mag extinction to IRS 16 at $\lambda = 2.12$ μm (Geballe *et al.* 1984). This intensity can be supplied by thermal emission from a column density $N(H_2) = 1.56 \times 10^{20}$ cm^{-2} at $T = 1000$ K. For comparison, we have computed a model of a radiatively excited cloud with $n_{\rm H} = 2 \times 10^4$ cm^{-3}, $T = 100$ K, $I_{\rm UV} = 10^4$, $N(H_2) = 10^{22}$ cm^{-2}, $b = 75$ km s^{-1}, grain model 2, $\varphi = 3$, and $T_f = 50$ K. Expecting heavy-element abundances to be somewhat higher in the Galactic center region than in the solar neighborhood, we have adopted a lower gas-to-extinction ratio $N_{\rm H}/A_V = 7.95 \times 10^{20}$ cm^{-2} mag^{-1} and a higher H_2 formation efficiency $y_f = 6$ than in the other models discussed above. This model yields $I[(1, 0)\ S(1)] = 5.3 \times 10^{-5}$ ergs s^{-1} cm^{-2} sr^{-1}, an intensity about 60 times smaller than the maximum observed. The values of the intensity ratios $I[(1, 0)\ S(1)]/I[(1, 0)\ S(0)]$ and $I[(1, 0)\ S(1)]/I[(2, 1)\ S(1)]$ are 1.2 and 1.6, respectively, compared with 3.7 and 200 in a purely thermal spectrum at $T = 1000$ K. A hybrid model like that described for NGC 7027 in § IV*b*, in which $n_{\rm H} = 2 \times 10^4$ cm^{-3}, $T = 1000$ K, $I_{\rm UV} = 10^4$, $N(H_2) = 1.56 \times 10^{20}$ cm^{-2}, and $\varphi = 1$, yields $I[(1, 0)\ S(1)] = 3.1 \times 10^{-3}$ ergs s^{-1} cm^{-2} sr^{-1} and line ratios $I[(1, 0)\ S(1)]/I[(1, 0)\ S(0)] = 3.7$ and $I[(1, 0)\ S(1)]/I[(2, 1)\ S(1)] = 29.8$. Thus at a level of at least one-sixtieth of the peak (1, 0) $S(1)$ line emission, radiatively excited H_2 can be expected to dominate the observed emission. Variations in the relative amounts of thermally excited and radiatively excited gas and in physical conditions from place to place in the Galactic center region could easily produce large variations in the H_2 line spectra. In particular, the line ratio $I[(1, 0)\ S(1)]/I[(2, 1)\ S(1)]$ is expected to be correlated with the absolute intensity of the (1, 0) $S(1)$ line.

The inner 2 pc region around IRS 16 is undoubtedly more complex than the simple picture described above. Far-infrared line emission suggests that much of the material in this region may be in condensations of very high density, 10^5 cm^{-3} or more, and with a small volume filling factor (Genzel *et al.* 1985). In this case, the H_2 fluorescence can be more efficient, and a greater cloud surface area can be exposed to ultraviolet radiation than in the uniform model described above. Indeed, Sternberg (1986) has recently suggested that the H_2 line emission can be explained entirely by a dense photodissociation region heated to high temperatures by the intense ultraviolet radiation field inferred by Genzel *et al.* (1985). A more definitive interpretation of the H_2 line emission must await more extensive data, particularly on the intensities of transitions arising in $v' \geq 3$, as suggested by Sternberg (1986). If the density is indeed greater than 10^5 cm^{-3}, the theoretical models must include collisional processes involving $v' \geq 2$.

d) The Orion Bright Bar Region

Regions in which H_2 is excited both by collisions at high temperatures, $T \approx 1000$–2000 K, and by nearby sources of ultraviolet radiation are probably rather common. In fact, in many cases the high temperature may be the result of the intense ultraviolet radiation rather than shock processes (Tielens and Hollenbach 1985*a*, *b*; Sternberg 1986). That both mechanisms are at work in the bright bar region of the Orion Nebula has already been suggested by Hayashi *et al.* (1985), who observed systematic variations in the $I[(1, 0)\ S(1)]/I[(2, 1)\ S(1)]$ intensity ratio. The maximum surface brightnesses in this region are $I[(1, 0)\ S(1)] = 1.1 \times 10^{-4}$ and $I[(2, 1)\ S(1)] = 6.5 \times 10^{-5}$ ergs s^{-1} cm^{-2} sr^{-1}. The fact that the bright bar is so sharply defined suggests that it is seen nearly edge-on; therefore, its projected angular separation θ from the Trapezium stars must be very close to its true separation, $R = \theta D$. In particular, the maximum intensity of the (2, 1) $S(1)$ line occurs at $\theta = 1'.9$ southeast of the Trapezium, which corresponds to $R = 0.25(D/450\ \mathrm{pc})$ pc. The emission nebula and associated bright bar are evidently foreground to the Kleinmann-Low nebula, the infrared sources, and masers deeper inside the Orion Molecular Cloud for which the distance, $D = 480 \pm 80$ pc, is directly measured (Genzel *et al.* 1981). If we consider a free-free continuum flux density $S_\nu = 360$ Jy at a high frequency $\nu = 24$ GHz where the nebula is optically thin, and adopt a mean nebular temperature of $T = 9500$ K (Chaisson and Dopita 1977), then for a uniform, spherical case B H II region of radius R, we infer a total luminosity of H-ionizing photons of $L_{\mathrm{ion}} = 5.2 \times 10^{48}(D/450\ \mathrm{pc})^2\ \mathrm{s}^{-1}$. The flux of $\lambda = 1000$ Å photons at distance R from the source(s) of radiation can be estimated from the ionizing luminosity if the effective temperature of the radiation source is known. This is a nontrivial exercise for the Orion Nebula: although θ^1(C) Ori is probably the principal source of ionizing photons, the other hot stars may contribute as well at longer ultraviolet wavelengths. Based on the energy distributions of single model atmospheres (Kurucz 1979), at $R = 0.25$ pc from the Trapezium stars the H_2-exciting flux is found to be $I_{\mathrm{UV}} = 2.4 \times 10^4$ or 4.1×10^4 for effective stellar temperatures of $T_* = 40{,}000$ and 35,000 K, respectively. This ignores the effects of internal dust. The estimated contribution of Lyα at the same boundary is given by $\alpha \approx 0.4$–0.7. It is clear from the results of models like No. 69 in Table 4 (see § III) that fluorescence alone can supply the maximum surface brightnesses observed in this region when $I_{\mathrm{UV}} \approx (2$–$4) \times 10^4$ and $n_{\mathrm{H}} \approx 10^4$ cm^{-3}, with grain model 3. Further observations will be required to determine what fraction of the (1, 0) $S(1)$ line intensity is formed in shock-heated gas in the bright bar region.

In discussing regions in which both collisional excitation and fluorescent excitation may play a role, it is important to consider observable properties other than line intensity ratios that will be useful in separating the contributions of the two excitation mechanisms. Webster (1985) has noted that fluorescent lines will be polarized in a characteristic, predictable manner that is distinguishable from polarization which results from scattering by dust particles (cf. Hough *et al.* 1986).

e) T Tauri and Related Objects

The younger stellar object T Tauri is a particularly interesting case in which the ultraviolet fluorescent emission of H_2 has already been identified (Brown *et al.* 1981). The ultraviolet spectrum of T Tau shows the characteristic signature of H_2 excited by intense H Lyα emission at $\lambda = 1215.6701$ Å with which there is a near-resonance in H_2, the $B\ ^1\Sigma_u^+$–$X\ ^1\Sigma_g^+$ (1, 2) $P(5)$ transition at $\lambda = 1216.0737$ Å. The difference in rest wavelengths of these lines corresponds to a Doppler velocity shift of 99.53 km s^{-1}. In order for this Lyα resonant excitation to be efficient, the H Lyα line must be fairly broad and the population of H_2 in $v = 2$, $J = 5$ must be relatively high.

The infrared spectrum of T Tau exhibits a strong (1, 0) $S(1)$ line, which is presumed to be thermally excited (Beckwith *et al.* 1978). The intensity of this line and the high population in $v = 2$ implied by the ultraviolet fluorescence require molecular gas at a temperature $T \approx 2000$ K (Brown *et al.* 1981; Brown, Ferraz, and Jordan 1984). The observed ultraviolet fluorescence will inevitably be accompanied by fluorescent emission in infrared lines. A simple model of the molecular emitting region can be constructed to predict the infrared line spectrum of H_2 and to identify those transitions that arise predominantly from Lyα fluorescent excitation.

The contribution of H Lyα to the ultraviolet radiation field is specified by a line width ΔV and a scaling factor α as described in § III*h* above. No self-absorption in the profile is assumed. Strong resonance lines in the ultraviolet spectrum of T Tau are observed to be quite broad, e.g., the Mg II lines have $\Delta V \approx 140$ km s^{-1} (Brown, Ferraz, and Jordan 1984). The H Lyα line is expected to be even broader, with a width possibly as large as $\Delta V \approx 500$ km s^{-1} (L. W. Hartmann 1987, private communication). The observed fluxes of the ultraviolet lines of H_2, after correction for a large and uncertain extinction, constrain the absorption rate in the B–X (1, 2)$P(5)$ line. If the upper state of the observed (1, 0) $S(1)$ line, ($v = 1$, $J = 3$), and the lower state of the pumping transition, ($v = 2$, $J = 5$), are assumed to be populated in equilibrium at $T = 2000$ K, then the reddening-corrected flux in the infrared line constrains the column density of hot H_2 and permits the Lyα flux to be estimated. A uniform, plane-parallel cloud model with the following parameters is adopted: $n_{\mathrm{H}} = 10^5$ cm^{-3}, $T = 2000$ K, $I_{\mathrm{UV}} = 5$, $\alpha = 1000$, $b = 60$ km s^{-3}, $\Delta V = 500$ km s^{-3}, and $N(H_2) = 2.8 \times 10^{18}$ cm^{-2}. The value of the Doppler parameter of the H_2 lines, b, is suggested by the widths of weak lines in the spectrum of T Tau. The values of n_{H}, I_{UV}, and α are not well constrained by the analysis: it is only required that the product $\alpha I_{\mathrm{UV}} \approx 5000$ and that n_{H} be large enough to maintain nearly thermalized populations in levels of $v = 0$, 1, and 2. For the present computation, a downward collisional rate coefficient of $k(v'J', v''J'') = 10^{-10}$ cm^3 s^{-1} has been adopted for all transitions $v' \rightarrow v'' = 2 \rightarrow 1$, $2 \rightarrow 0$, $1 \rightarrow 0$, $2 \rightarrow 2$, and $1 \rightarrow 1$, and the corresponding upward rates have been evaluated in detailed balance.

The model provides column densities in all levels of H_2 under the specified excitation conditions. In particular, the column density

1987ApJ...322..412B

in $B\,{}^1\Sigma_u^+(v = 1, J = 4)$, the upper state of the principal pumping transition, is $N_B(1, 4) = 16.8$ cm^{-2}. The excitation temperatures,

$$T_{\rm ex} = hc\left\{\lambda k \ln\left[\frac{2J' + 1}{2J'' + 1}\,\frac{N_X(v'', J'')}{N_B(v', J')}\right]\right\}^{-1} \text{ K} , \tag{21}$$

that characterize the emissivities of the ultraviolet transitions $B\,{}^1\Sigma_u^+(v', J') \rightarrow X\,{}^1\Sigma_g^+(v'', J'')$ are calculated to have values $T_{\rm ex} \approx$ 3000–3700 K for the lines in the range $\lambda = 1200$–1600 Å. The fluxes of ultraviolet lines are calculated according to

$$f_{\rm UV} = B_\nu(T_{\rm ex})[1 - \exp(-\tau)]\Delta\nu\Omega_{\rm UV} \times 10^{-0.4A_\lambda} \text{ ergs s}^{-1}\text{ cm}^{-2} , \tag{22}$$

where $B_\nu(T)$ is the Planck function evaluated at the transition frequency, τ is the line-center optical depth (eq. [9]), $\Delta\nu = 1.00 \times 10^{12}(b/60 \text{ km s}^{-1})(1000 \text{ Å}/\lambda)$ Hz is the line width, and $\Omega_{\rm UV} = 4.7$ nsr is the solid angle of the large aperture of the *IUE* spectrograph used in the observations. The extinction A_λ is based on a color excess $E(B-V) = 0.54$ mag and a standard extinction curve with $A_V = 3.1E(B-V)$ mag. Brown, Ferraz, and Jordan (1984) compared their measured flux ratios with predicted values for optically thin lines, but noted that some lines might be reduced in strength by self-absorption. Our expression, equation (22), for the line flux incorporates this optical depth effect directly. In the model discussed here, the effect is small, but nonnegligible, with $\tau \approx 0.6$–3.0 for the stronger lines. The fluxes in the optically thin infrared lines are

$$f_{\rm IR} = \frac{hc\tilde{\nu}}{4\pi} A_{v'J', v''J''} N_X(v'J')\Omega_{\rm IR} 10^{-0.4A_\lambda} \text{ ergs s}^{-1}\text{ cm}^{-2} , \tag{23}$$

where $\Omega_{\rm IR} = 0.46$ nsr for comparison with fluxes measured in a 5″ aperture by Beckwith *et al.* (1978).

The results of this model computation are summarized in Table 11, which lists wavelengths, intrinsic intensities, and reddened fluxes as well as observed fluxes for selected ultraviolet and infrared lines of H_2. The infrared line intensities obtained in the present model are compared with those resulting from a purely thermal distribution at $T = 2000$ K. It is obvious that odd-J levels in $v \geq 2$ have significantly enhanced populations because of the pumping by the B–X (1, 2) $P(5)$ line. The ultraviolet lines with even-valued rotational quanta in the lower state, e.g., B–X (1, 3) $P(8)$, arise from Lyα pumping of the $B\,{}^1\Sigma_u^+$–$X\,{}^1\Sigma_g^+$ (1, 2) $R(6)$ transition at $\lambda = 1215.7314$ Å, which is only 12.12 km s^{-1} off exact resonance. For a Lyα line width of $\Delta V = 500$ km s^{-1}, the excitation rate in the (1, 2) $R(6)$ line is a factor of 1.3 times larger than that in the (1, 2) $P(5)$ line; however, the ratio of lower-state populations at $T = 2000$ K, $n(2, 5)/n(2, 6) = 3.9$, more than compensates for the difference in pumping efficiency, so that the fluorescent lines excited through B–X (1, 2) $P(5)$ tend to be approximately 3 times stronger than the corresponding lines excited through B–X (1, 2) $R(6)$, as indicated in the table. The relative excitation rates in the two resonances will be a strong function of the width of the Lyα line when $\Delta V \leq 100$ km s^{-1}. This means, of course, that accurate measurements of all of the ultraviolet line fluxes could be used to infer the Lyα intensity at two points on its velocity profile. As mentioned in § III*h*, the $S(3)/S(4)$ line intensity ratios in the (2, 1), (2, 0), (5, 3), and (5, 2) bands should be sensitive to the value of α. For the specific model discussed here, the values of these ratios are 4.1, 3.6, 9.4, and 8.5, respectively. Although Brown, Ferraz, and Jordan (1984) do not discuss the identification of any $B\,{}^1\Sigma_u^+$–$X\,{}^1\Sigma_g^+$ (v', v'') $R(6)$ and $P(8)$ lines in their spectra, the strongest of the predicted lines may contribute at the expected level to unassigned features in the published spectrum, notably at 1523 and 1468 Å. Resonant excitation by Lyα of H_2 lines arising in higher states is also included in the calculations, although thermal populations are maintained only in $v \leq 2$. The highly populated ground state of ortho-H_2, ($v = 0$, $J = 1$), can also be excited by H Lyβ, $\lambda = 1025.7223$ Å, through the near-resonance with H_2 B–X (6, 0) $P(1)$ at $\lambda = 1025.935$ Å, for which the rest velocity difference is 62.1 km s^{-1}. In the absence of a good estimate of the Lyβ intensity, this process has been omitted. Observationally, the Lyβ excitation mechanism would be revealed by strong emission in the B–X (6, 13) $P(1)$ line at 1607.504 Å, which has a branching ratio of 27.0% of the total ultraviolet fluorescence. A striking consequence of this would be the relatively large intensities of the $Q(1)$ and $O(3)$ lines of the (13, 10), (13, 9), and (13, 8) vibration-rotation bands that cannot be excited efficiently otherwise.

The close agreement between observed and computed line fluxes from 0.126 to 2.25 μm demonstrates that the model satisfies the basic observational constraints. However, this model should be taken not as a realistic representation of the molecular emitting region in T Tau but rather as a device for predicting the intensities of unobserved transitions of H_2. Model calculations of the type described here could be refined further to study the structure of the extended atmosphere of T Tau if better, more extensive observations were available. High-resolution spectra of fluorescent lines in the 1 μm region would be particularly interesting for the velocity information they could provide about the extended atmosphere. We note that there are numerous, potentially detectable transitions with common states, whose intrinsic intensity ratios are fixed and whose apparent intensity ratios would provide a good measure of the extinction to the emitting region. For example, the lower state of the observed B–X (1, 7) $P(5)$ line at 1504.8 Å is also the upper state of the (7, 5) $S(3)$, (7, 4) $S(3)$, and (7, 3) $S(3)$ lines at 1.56, 1.04, and 0.766 μm, respectively. The relative fluxes in these infrared lines can yield directly a determination of reddening over a factor of 2 in wavelength. The apparent strength of the ultraviolet line is affected by self-absorption within the emitting region as well as by external extinction, but this can be treated through a model analysis as discussed above. The amount of extinction and the shape of the extinction curve for T Tau remain controversial (Schwartz 1974; Cohen and Kuhi 1979; Cohen 1980; Meyer and Ulrich 1984; Cohen and Witteborn 1985).

Ultimately the study of H_2 line formation in an extended atmosphere like that of T Tau will need to be combined with an accurate treatment of the formation of optically thick Lyman lines in a nonstatic, dusty, and perhaps nonspherical atmosphere. In principle, the analysis of accurate measurements of various H_2 lines could yield important insight into the structure of such an atmosphere.

Infrared line emission of H_2, presumably from shock-heated gas, has been detected in a number of Herbig-Haro objects (Fischer, Righini-Cohen, and Simon 1980; Elias 1980; Simon and Joyce 1983; Harvey *et al.* 1986). Ultraviolet fluorescent emission in H_2 has also been observed in the Herbig-Haro objects HH 43 and HH 47 (Schwartz 1983; Schwartz, Dopita, and Cohen 1985). The observed fluxes in the ultraviolet lines suggest that fluorescent lines of H_2, like (3, 2) $S(1)$, should be present in the infrared spectrum

TABLE 11

H_2 LINE FLUXES IN T TAURI

Line	λ^a Å	$10^4 I(model)^b$ erg s^{-1} cm^{-2} sr^{-1}	$10^4 I(thermal)^c$ erg s^{-1} cm^{-2} sr^{-1}	$10^{13} f(model)^d$ erg s^{-1} cm^{-2}	$10^{13} f(observed)^e$ erg s^{-1} cm^{-2}
(0,0) S(5)	69076.35	3.34	3.32	1.5	...
(0,0) S(7)	55097.	4.83	4.87	2.2	...
(0,0) S(9)	46933.3	3.53	3.66	1.6	...
(1,0) O(5)	32341.	3.60	3.60	1.5	...
(1,0) Q(5)	24541.	4.48	4.49	1.8	...
(1,0) Q(3)	24230.68	6.41	6.41	2.5	...
(1,0) Q(2)	24127.80	2.12	2.12	0.84	...
(1,0) Q(1)	24059.35	6.37	6.37	2.5	...
(3,2) S(1)	23858.	0.997	0.0525	0.39	...
(2,1) S(1)	22471.	0.762	0.752	0.30	< 3
(1,0) S(1)	21212.54	9.13	9.13	3.5	3.1±0.4
(1,0) S(2)	20332.03	3.40	3.41	1.3	...
(7,5) S(1)	16201.	0.924	2.39(-5)	0.32	...
(7,5) S(3)	15611.	1.10	2.84(-5)	0.38	...
(5,3) Q(3)	15052.	0.929	1.04(-3)	0.31	...
(4,2) Q(3)	14090.	1.04	8.18(-3)	0.33	...
(5,3) S(1)	13997.	1.30	1.46(-3)	0.42	...
(3,1) Q(1)	13237.	1.17	0.0378	0.36	...
(4,2) S(1)	13112.	1.51	0.0119	0.47	...
(3,1) S(1)	12327.	1.78	0.0935	0.53	...
(7,4) S(3)	10401.00	1.13	2.90(-5)	0.30	...
(7,4) S(4)	10328.94	0.372	9.37(-6)	0.097	...
(6,3) S(1)	9876.69	0.523	1.05(-4)	0.13	...
(6,3) S(3)	9657.81	0.743	1.58(-4)	0.18	...
(6,3) S(4)	9584.19	0.348	5.09(-5)	0.084	...
(6,3) S(6)	9507.87	0.449	3.40(-5)	0.11	...
(5,2) S(1)	9229.20	0.520	5.83(-4)	0.12	...
(4,1) S(1)	8659.74	0.366	2.89(-3)	0.079	...
(8,4) S(6)	8288.41	0.318	3.14(-6)	0.065	...
(8,4) S(3)	8287.23	0.343	2.87(-6)	0.071	...
(7,3) S(3)	7663.10	0.450	1.16(-5)	0.083	...
B-X (1,8) P(5)	1562.3921	16.0	...	1.6	≥ 1.6
B-X (1,8) R(3)	1547.3371	9.89	...	0.98	1.2
B-X (1,7) P(8)	1524.6531	...	...	0.60	...
B-X (1,7) P(5)	1504.7557	16.4	...	1.5	2.1
B-X (1,7) R(6)	1500.4487	...	...	0.54	...
B-X (1,7) R(3)	1489.5675	11.5	...	1.1	1.7
B-X (1,6) P(8)	1467.0849	...	...	0.39	...
B-X (1,6) P(5)	1446.1157	16.3	...	1.4	1.3
B-X (1,6) R(6)	1442.8728	...	...	0.35	...
B-X (1,6) R(3)	1431.0142	11.6	...	0.97	0.93
B-X (1,3) P(8)	1293.8751	...	...	0.28	...
B-X (1,3) P(5)	1271.9284	20.0	...	1.0	0.75
B-X (1,3) R(6)	1271.0188	...	...	0.23	...
B-X (1,3) R(3)	1257.8227	6.78	...	0.33	≤ 0.35

[a] Wavelengths $\lambda < 2000$ Å are vacuum values measured by Dabrowski 1984; other wavelengths are values in standard air.

[b] See text.

[c] The thermal calculation assumes $T = 2000$ K and $N(H_2) = 2.8 \times 10^{18}$.

[d] Fluxes assume $A_V = 1.67$ mag and a standard extinction law; see text.

[e] Observed fluxes are those of Beckwith *et al.* 1978 in the infrared and Brown, Ferraz, and Jordan 1984 in the ultraviolet.

at a level of at least 2×10^{-14} ergs s^{-1} cm^{-2}, which corresponds to a surface brightness of 4×10^{-6} ergs s^{-1} cm^{-2} sr^{-1}. This point has been developed in more detail recently by Schwartz, Cohen, and Williams (1987), who obtained infrared spectra of several low-excitation HH objects. Lightfoot and Glencross (1986) have recently presented infrared spectra of HH 7–11 and NGC 1333 that show strong H_2 emission. The measured surface brightness of the (1, 0) $S(1)$ line lies in the range 3×10^{-4} to 1.9×10^{-3} ergs s^{-1} cm^{-2} sr^{-1}, and some of their spectra seem to have a fluorescent contribution, judging by apparent emission at the positions of highly excited transitions.

f) *Unresolved Star-forming Regions*

Some galaxies are thought to be undergoing remarkably efficient bursts of star formation (cf. Rieke *et al.* 1980). Among the signatures of such activity are (1) intense H recombination line emission that indicates the presence of gas ionized by young, massive stars; (2) intense infrared line emission of H_2 that reveals a large quantity of disturbed molecular gas; (3) stellar absorption features that arise in a large population of supergiant stars of recent origin; and (4) a high luminosity in the far-infrared resulting from warm interstellar dust in the star-forming regions. The infrared spectrum of the prototypical starburst galaxy, M82, shows most but not all of these features: the H_2 (1, 0) $S(1)$ line has remained undetectable at the level of $f < 4 \times 10^{-14}$ ergs s^{-1} cm^{-2} (Rieke *et al.* 1985). Strong H_2 line emission has been reported for NGC 6240 (Joseph, Wright, and Wade 1984; Rieke *et al.* 1985; DePoy, Becklin, and Wynn-Williams 1986), Arp 220 (Rieke *et al.* 1985), NGC 3690 (Fischer *et al.* 1983), and NGC 253 (Rieke, Lebofsky, and Walker 1987), all of which have been identified as starburst galaxies. The starburst hypothesis has been questioned for NGC 6240 (DePoy, Becklin, and Wynn-Williams 1986), where the evident galaxy-galaxy interaction may be *directly* responsible for some of the observed phenomena rather than indirectly through its stimulation of an enhanced rate of star formation. In any case, the intense H_2 emission has been attributed to shock-heated gas in all such systems where it has been seen. It is therefore of interest to inquire whether fluorescent emission of H_2 can be detected from unresolved ensembles of young, hot stars and the remnants of the molecular clouds out of which they formed. As the sensitivity of infrared spectrometers improves, fluorescent H_2 emission may become more readily measurable. A simple model can be used to illustrate how measurements of H and H_2 lines might provide a valuable measure of star-forming activity.

Ultraviolet light from early-type stars ionizes some of the surrounding gas for $\lambda < 912$ Å and excites H_2 in the surfaces of the molecular reservoirs for $\lambda > 912$ Å. The intensities of H recombination lines and of H_2 fluorescent lines can be used to gauge the number of early-type stars, the mass of ionized gas, and the fraction of the original gas that has been converted into massive stars. Consider a spherical region of radius ρ that contains $\mathcal{N}_c$ identical neutral clouds each of density $n_{\rm H}$, temperature T_c, and radius r_c, embedded in a uniform photoionized gas of electron density n_e and temperature $T_e \approx 10^4$ K. Mixed randomly in this region are $\mathcal{N}_*$ identical early-type stars of effective temperature T_* and radius R_*, which are responsible for the ionization. The total pressure of each phase of the gas is the sum of thermal gas pressure and "turbulent" pressure characterized by a superthermal Doppler parameter b. The cloud models of Tables 1 and 4 have been computed for $b_c = 4$ km s^{-1}. If it is assumed that the neutral cloud boundaries are in approximate pressure balance with ionized gas in which $b_i \approx 16$ km s^{-1}, then

$$\frac{n_{\rm H}}{n_e} \approx 32\left[\frac{0.5(b_i/16)^2 + 0.5}{(b_c/4)^2 + 0.0855(T_c/100)}\right] . \tag{24}$$

Each early-type star has a total luminosity of ionizing photons L_i^* s^{-1} and a spectral luminosity of $\lambda = 1000$ Å photons, L_ν^* s^{-1} Hz^{-1}, which are functions of the effective stellar temperatures. Table 12 lists values of these parameters based on the model atmospheres of Kurucz (1979). If the ionized gas is treated as a case B Strömgren sphere of radius ρ, then the flux of the H Brγ line measurable at a distance D is

$$f_\gamma = 1.0 \times 10^{-12}\left(\frac{L_i^*}{5 \times 10^{48}}\right)\left(\frac{\mathcal{N}_*}{8000}\right)\left(\frac{D}{\rm Mpc}\right)^{-2} \text{ ergs s}^{-1}\text{ cm}^{-2} . \tag{25}$$

The corresponding total H_2 flux summed over all fluorescent lines, $f_{\rm H_2} = A_c I_{\rm total} D^{-2}$, can be written

$$f_{\rm H_2} = 4.6 \times 10^{-13}\left(\frac{I_{\rm total}}{10^{-3}}\right)\left(\frac{\mathcal{M}_c}{10^4}\right)^{2/3}\left(\frac{\mathcal{N}_c}{80}\right)^{1/3}\left(\frac{n_{\rm H}}{3000}\right)^{-2/3}\left(\frac{D}{\rm Mpc}\right)^{-2} \text{ ergs s}^{-1}\text{ cm}^{-2} , \tag{26}$$

where $A_c = \mathcal{N}_c 4\pi r_c^2$ is the total surface area of cloud material, $I_{\rm total}$ is assumed to have the same meaning as in § III, and $\mathcal{M}_c$ is the total mass in neutral clouds in units of $M_\odot$. The fluxes of individual lines can be reckoned through use of the relative intensities tabulated in § III. The total intensity, $I_{\rm total}$, is a function primarily of $n_{\rm H}$ and $I_{\rm UV}$. The characteristic scaling factor of the radiation field in this situation is defined in terms of the 1000 Å flux,

$$\phi_{1000} = \frac{L_\nu^*}{4\pi d_*^2} \text{ cm}^{-2}\text{ s}^{-1}\text{ Hz}^{-1} , \tag{27}$$

TABLE 12

LUMINOSITIES OF EARLY-TYPE STARS

T_* (K)	log g	$L_\nu^*(R_\odot/R_*)^2$ (s^{-1} Hz^{-1})	$L_i^*(R_\odot/R_*)^2$ (s^{-1})	L_i^*/L_ν^* (Hz)
25,000..........	3.5	2.38(31)	9.54(44)	4.02(13)
30,000..........	4.0	5.78(31)	6.63(45)	1.15(14)
35,000..........	4.0	1.04(32)	3.96(46)	3.79(14)
40,000..........	4.5	1.48(32)	9.59(46)	6.46(14)
50,000..........	4.5	2.66(32)	2.61(47)	9.82(14)

NOTE.—The tabulated numbers are based on the model atmospheres of Kurucz 1979. For the log g = 4.0 models, the spectral luminosity can be approximated by

$$L_\nu^* = 5.44 \times 10^{33}(R_*/10\ R_\odot)^2(T_*/30{,}000\ {\rm K})^{3.9}\ {\rm s}^{-1}\ {\rm Hz}^{-1}$$

within 13% per cent over the range 25,000 ≤ T_* ≤ 40,000 K.

evaluated at one-half the mean separation of the hot stars,

$$d_*/2 \approx \rho \mathcal{N}_*^{-1/3} \text{ pc} . \tag{28}$$

Thus

$$I_{\text{UV}} = 2300\left(\frac{L_\nu^*}{10^{34}}\right)\left(\frac{\mathcal{N}_*}{8000}\right)^{2/3}\left(\frac{\Omega}{\text{nsr}}\right)^{-1}\left(\frac{D}{\text{Mpc}}\right)^{-2} , \tag{29}$$

where $\Omega = \pi(\rho/D)^2$ nsr is the solid angle subtended by the star-forming region (or, in a more practical sense, by a spectrometer aperture). The mass of ionized gas within the Strömgren sphere of radius ρ can be written

$$\mathcal{M}_i = 3.58 \times 10^5(1 - \eta_c)^{1/2}\left(\frac{L_i^*}{5 \times 10^{48}}\right)^{1/2}\left(\frac{\mathcal{N}_*}{8000}\right)^{1/2}\left(\frac{\Omega}{\text{nsr}}\right)^{3/4}\left(\frac{D}{\text{Mpc}}\right)^{3/2} M_\odot , \tag{30}$$

where $\eta_c = \mathcal{N}_c(r_c/\rho)^3$ is the volume filling factor of the clouds.

As an example, consider the most extreme case of H_2 line emission from NGC 6240. If we adopt $D = 92$ Mpc and a reddening-corrected H Brγ flux of $f_\gamma = 1.4 \times 10^{-13}$ ergs s^{-1} cm^{-2} in a beam of size $\Omega = 1.4$ nsr (Rieke *et al.* 1985), then we infer $\mathcal{N}_*(L_i^*/5 \times 10^{48}) \approx 9.5 \times 10^6$ from equation (25). The implied mass of early-type stars is of the order of 10^8 $M_\odot$ or more. The mean density and the total mass of ionized gas are $n_e \approx 14(1 - \eta_c)^{-1/2}$ cm^{-3} and $\mathcal{M}_i \approx 1.4 \times 10^{10}$ $(1 - \eta_c)^{1/2}$ $M_\odot$, respectively. If $b_i = 30$ km s^{-1}, then $n_{\text{H}} \approx 10^3$ cm^{-3}, and the nonionizing radiation is expected to be $I_{\text{UV}} = 26$. Model 48 of Table 4 suggests $I_{\text{total}} \approx 2 \times 10^{-4}$ and a relative intensity of the (1, 0) $S(1)$ line of approximately 0.018. Equation (26) implies that a total cloud mass $\mathcal{M}_c \approx 1.6 \times 10^{11}$ $M_\odot$ in the form of $r_c = 3.4$ pc clouds with a total filling factor $\eta_c = 0.17$ would be required to produce the observed (reddening-corrected) (1, 0) $S(1)$ line flux of 1.8×10^{-12} ergs s^{-1} cm^{-2} (Rieke *et al.* 1985) by fluorescence alone. This would increase by a factor of 10 the already enormous mass involved in this suggested starburst galaxy; therefore, it is more likely that the observed H_2 line emission is excited primarily by a large-scale shock (cf. Rieke *et al.* 1985). It is possible, of course, that the clouds and hot stars are more closely associated with each other than our estimates based on a random distribution suggest, or that the densities in the clouds are significantly higher. In that case, I_{total} could be up to an order of magnitude larger. Alternatively, if $\mathcal{M}_c \approx 0.1\mathcal{M}_i$, then we expect $f_{H_2} \approx 9.8 \times 10^{-13}$ ergs s^{-1} cm^{-2} and $f[(1, 0)\ S(1)] \approx 1.5 \times 10^{-14}$ ergs s^{-1} cm^{-2}, less than 1% of the observed flux. Thus, within the context of the starburst explanation of NGC 6240, H_2 fluorescence lines are expected at a level of 0.1 times the H Brγ flux if one-tenth of the total mass of ionized gas remains in neutral clouds. This example suggests that measurements of the fluorescent lines of H_2 can be used to place limits on the amount of molecular cloud material left in starburst regions. Observations in the 1–2 μm region would directly reveal the amount of H_2 excited by fluorescence, and would thus give direct information on the molecular cloud mass.

g) Other Sources

Sellgren (1986) has detected strong H_2 emission in two other reflection nebulae besides NGC 2023, Parsamyan 18 and NGC 1333. In Parsamyan 18 the relatively strong (2, 1) lines indicate that ultraviolet fluorescence is responsible for the excitation. The observed surface brightness can easily be accounted for by reasonable values of the parameters n_{H} and I_{UV}, similar to those for NGC 2023. Wynn-Williams *et al.* (1986) have recently found H_2 emission in the compact nebula associated with IRAS 04238 + 5336. They note the similarity of the spectrum to that of Parsamyan 18. Indeed, there are plausible—if barely significant—features at the expected positions of all the accessible low-J S-branch lines of the (2, 1) and (3, 2) bands in the spectrum published by Wynn-Williams *et al.* (1986). Thus there is a strong indication that IRAS 04238 + 5336 is also a source of radiatively excited H_2. Further study of the H_2 lines could reveal much about the physical conditions in this compact nebula.

V. CONCLUDING REMARKS

Infrared line spectra of H_2 due to ultraviolet excitation followed by fluorescence contain a significant amount of information on the physical properties of the line-emitting region. As demonstrated in § III, the absolute H_2 infrared line intensities depend primarily on the density in the cloud and the strength of the incident ultraviolet radiation, and to a lesser extent on the temperature of the gas, the total thickness of the cloud, and the optical properties of the grains. The relative line intensities are rather insensitive to most of these parameters; they vary slightly with temperature and with the model that is adopted for the formation process of H_2 on the surfaces of grains. Detailed infrared spectra of H_2 at comparatively low resolution, such as those recently obtained for the NGC 2023 region, can be used to infer the physical conditions quite accurately. The main uncertainty in the derived parameters stems from our limited knowledge of the scattering properties of grains at ultraviolet wavelengths, and of the formation rate of H_2 on grains. Measurements between 1 and 2 μm can constrain the models for the initial vibration-rotation population distribution of H_2 on the surfaces of grains.

In general, excitation by ultraviolet fluorescence will provide larger populations in vibrational levels with $v \geq 2$ than collisional excitation in realistic molecular shocks. As a consequence, fluorescent emission can be distinguished from collisionally excited emission through its more prominent transitions with $v' \geq 2$. Observations at $\lambda < 2$ μm, where $\Delta v \geq 2$ transitions occur, will be particularly useful. At longer wavelengths, observations of the (0, 0) $S(0)$ and $S(1)$ lines at 28 and 17 μm may provide more direct information on the temperature in the cloud, and on the ortho/para H_2 ratio.

In many regions, H_2 is probably excited both by collisions at high temperatures, $T \approx 1000$–2000 K, and by nearby sources of ultraviolet radiation. In these cases, the (1, 0) and (2, 1) infrared lines in the 2 μm region that are excited by resonance fluorescence will often be overwhelmed by the strong collisionally excited emission. As discussed in § IIIg, the amount of H_2 necessary to produce a certain line intensity at 2 μm by thermal excitation is orders of magnitude less than that required by ultraviolet excitation. However, at shorter wavelengths $\lambda < 2$ μm the fluorescent emission will be relatively more prominent.

1987ApJ...322..412B

Fluorescent excitation of H_2 can also be measured by means of its ultraviolet absorption lines superposed on the spectra of early-type stars. In these cases the measured rotational population distribution within $v = 0$ alone does not suffice to distinguish the contributions of shock-heated gas along the line of sight from fluorescent excitation. Measurable concentrations of molecules in vibrationally excited levels, however, can be maintained in dilute, diffuse interstellar clouds only by fluorescent excitation; thus their detection would provide a direct measure of the relative importance of shock heating and fluorescent excitation in these diffuse clouds (cf. van Dishoeck and Black 1986).

The main limitation of the present models is the neglect of collisional processes in general in $v \geq 1$. This implies in practice that the models are restricted to regions with densities less than 10^5 cm^{-3}. For higher densities, the collisional processes will modify the relative line intensities (Sternberg 1986). Models of denser clouds will be of interest for comparison with a multitude of recent observational data, but realistic models must await more accurate collisional rates.

The authors are indebted to I. Gatley for providing them with his H_2 spectra of NGC 2023 in advance of publication. They are grateful to A. Sternberg for useful comments on the manuscript. This work was supported in part by the National Aeronautics and Space Administration through Theoretical Astrophysics grant NAGW-763 to the University of Arizona. The hospitality of the Institute for Advanced Study, and its partial support through National Science Foundation grant PHY-8217352, are greatly appreciated.

REFERENCES

Allison, A. C., and Dalgarno, A. 1967, *Proc. Phys. Soc. London*, **90**, 609.
———. 1969, *Atomic Data*, **1**, 91.
Bartoe, J.-D. F., Brueckner, G. E., Nicolas, K. R., Sandlin, G. D., VanHoosier, M. E., and Jordan, C. 1979, *M.N.R.A.S.*, **187**, 463.
Beckwith, S., Evans, N. J., Gatley, I., Gull, G., and Russell, R. W. 1983, *Ap. J.*, **264**, 152.
Beckwith, S., Gatley, I., Matthews, K., and Neugebauer, G. 1978, *Ap. J.* (*Letters*), **223**, L41.
Beckwith, S., Neugebauer, G., Becklin, E. E., Matthews, K., and Persson, S. E. 1980, *A.J.*, **85**, 886.
Benvenuti, P., Dopita, M., and D'Odorico, S. 1980, *Ap. J.*, **238**, 601.
Black, J. H., and Dalgarno, A. 1976, *Ap. J.*, **203**, 132.
———. 1977, *Ap. J. Suppl.*, **34**, 405.
Black, J. H., Dupree, A. K., Hartmann, L. W., and Raymond, J. C. 1980, *Ap. J.*, **239**, 502.
Black, J. H., Porter, A., and Dalgarno, A. 1981, *Ap. J.*, **249**, 138.
Black, J. H., and van Dishoeck, E. F. 1987, in preparation (Paper II).
Black, J. H., and Willner, S. P. 1984, *Ap. J.*, **279**, 673.
Bouchet, P., Lequeux, J., Maurice, E., Prévot, L., and Prévot-Burnichon, M. L. 1985, *Astr. Ap.*, **149**, 330.
Bragg, S. L., Brault, J. W., and Smith, W. H. 1982, *Ap. J.*, **263**, 999.
Brown, A., Ferraz, M. C. de M., and Jordan, C. 1984, *M.N.R.A.S.*, **207**, 831.
Brown, A., Jordan, C., Millar, T. J., Gondhalekar, P., and Wilson, R. 1981, *Nature*, **290**, 34.
Burke, J. R., and Hollenbach, D. J. 1983, *Ap. J.*, **265**, 223.
Campins, H., Rieke, G. H., and Lebofsky, M. J. 1985, *A.J.*, **90**, 896.
Carruthers, G. R. 1970, *Ap. J.* (*Letters*), **161**, L81.
Chaisson, E. J., and Dopita, M. A. 1977, *Astr. Ap.*, **56**, 385.
Chlewicki, G., and Greenberg, J. M. 1984*a*, *M.N.R.A.S.*, **210**, 791.
———. 1984*b*, *M.N.R.A.S.*, **211**, 719.
Cohen, M. 1980, *M.N.R.A.S.*, **191**, 499.
Cohen, M., and Kuhi, L. V. 1979, *Ap. J. Suppl.*, **41**, 743.
Cohen, M., and Witteborn, F. C. 1985, *Ap. J.*, **294**, 345.
Crawford, M. K., Genzel, R., Townes, C. H., and Watson, D. M. 1985, *Ap. J.*, **291**, 755.
Dabrowski, I. 1984, *Canadian J. Phys.*, **62**, 1639.
de Boer, K. S. 1983, *Astr. Ap.*, **125**, 258.
DePoy, D. L., Becklin, E. E., and Wynn-Williams, C. G. 1986, *Ap. J.*, **307**, 116.
Draine, B. T. 1978, *Ap. J. Suppl.*, **36**, 595.
Draine, B. T., and Lee, H. M. 1984, *Ap. J.*, **285**, 89.
Draine, B. T., and Salpeter, E. E. 1978, *Nature*, **271**, 730.
Duley, W. W., and Williams, D. A. 1986, *M.N.R.A.S.*, **223**, 177.
Elias, J. H. 1980, *Ap. J.*, **241**, 728.
Federman, S. R., Glassgold, A. E., and Kwan, J. 1979, *Ap. J.*, **227**, 466.
Feldman, P. D., and Fastie, W. G. 1973, *Ap. J.* (*Letters*), **185**, L101.
Field, G. B., Somerville, W. B., and Dressler, K. 1966, *Ann. Rev. Astr. Ap.*, **4**, 207.
Fink, U., Wiggins, T. A., and Rank, D. H. 1965, *J. Molec. Spectrosc.*, **18**, 384.
Fischer, J., Righini-Cohen, G., and Simon, M. 1980, *Ap. J.* (*Letters*), **238**, L155.
Fischer, J., Simon, M., Benson, J., and Solomon, P. M. 1983, *Ap. J.* (*Letters*), **273**, L27.
Ford, A. L., Docken, K. K., and Dalgarno, A. 1975, *Ap. J.*, **200**, 788.
Gatley, I., *et al.* 1987, *Ap. J.* (*Letters*), **318**, L73.
Gatley, I., Jones, T. J., Hyland, A. R., Beattie, D. H., and Lee, T. J. 1984, *M.N.R.A.S.*, **210**, 565.
Gatley, I., Jones, T. J., Hyland, A. R., Wade, R., Geballe, T. R., and Krisciunas, K. 1986, *M.N.R.A.S.*, **222**, 299.
Gatley, I., and Kaifu, N. 1987, in *Astrochemistry*, ed. M. S. Vardya and S. P. Tarafdar (Dordrecht: Reidel), p. 153.
Geballe, T. R., Krisciunas, K., Lee, T. J., Gatley, I., Wade, R., Duncan, W. E., Garden, R., and Becklin, E. E. 1984, *Ap. J.*, **284**, 118.
Genzel, R., Reid, M. J., Moran, J. M., and Downes, D. 1981, *Ap. J.*, **244**, 884.
Genzel, R., Watson, D. M., Crawford, M. K., and Townes, C. H. 1985, *Ap. J.*, **297**, 766.
Glass-Maujean, M. 1986, *Phys. Rev. A*, **33**, 342.
Gould, R. J., and Harwit, M. 1963, *Ap. J.*, **137**, 694.
Green, S., and Truhlar, D. G. 1979, *Ap. J.* (*Letters*), **231**, L101.
Gull, T. R., and Harwit, M. 1971, *Ap. J.*, **168**, 15.
Habing, H. J. 1968, *Bull. Astr. Inst. Netherlands*, **19**, 421.
Harvey, P. M., Joy, M., Lester, D. F., and Wilking, B. A. 1986, *Ap. J.*, **301**, 346.
Harvey, P. M., Thronson, H. A., and Gatley, I. 1980, *Ap. J.*, **235**, 894.
Hasegawa, T., Gatley, I., Garden, R. P., Brand, P. W. J. L., Ohishi, M., Hayashi, M., and Kaifu, N. 1987, *Ap. J.* (*Letters*), **318**, L77.
Hayashi, M., Hasegawa, T., Gatley, I., Garden, R., and Kaifu, N. 1985, *M.N.R.A.S.*, **215**, 31P.
Herzberg, G. 1950, *Canadian J. Phys.*, **A28**, 144.
Hollenbach, D., and McKee, C. F. 1979, *Ap. J. Suppl.*, **41**, 555.
Hollenbach, D. J., Werner, M. W., and Salpeter, E. E. 1971, *Ap. J.*, **163**, 165.
Hough, J. H., *et al.* 1986, *M.N.R.A.S.*, **222**, 629.
Jennings, D. E., and Brault, J. W. 1983, *J. Molec. Spectrosc.*, **102**, 265.
Jennings, D. E., Rahn, L. A., and Owyoung, A. 1985, *Ap. J.* (*Letters*), **291**, L15.
Johnson, H. L. 1965, *Ap. J.*, **141**, 923.
Jordan, C., Brueckner, G. E., Bartoe, J.-D. F., Sandlin, G. E., and VanHoosier, M. E. 1977, *Nature*, **270**, 326.
———. 1978, *Ap. J.*, **226**, 687.
Joseph, R. D., Wright, G. S., and Wade, R. 1984, *Nature*, **311**, 132.
Jura, M. 1974, *Ap. J.*, **191**, 375.
———. 1975*a*, *Ap. J.*, **197**, 575.
———. 1975*b*, *Ap. J.*, **197**, 581.
———. 1980, *Ap. J.*, **235**, 63.
Knacke, R. F., and Young, E. T. 1981, *Ap. J.* (*Letters*), **249**, L65.
Knapp, G. R., Brown, R. L., and Kuiper, T. B. H. 1975, *Ap. J.*, **196**, 167.
Koornneef, J. 1982, *Astr. Ap.*, **107**, 247.
Kurucz, R. L., 1979, *Ap. J. Suppl.*, **40**, 1.
Leonas, V. B., and Pjarnpuu, A. A. 1981, *Soviet Astr. Letters*, **7**, 19.
Lightfoot, J. F., and Glencross, W. M. 1986, *M.N.R.A.S.*, **221**, 993.
Massa, D., Savage, B. D., and Fitzpatrick, E. L. 1983, *Ap. J.*, **266**, 662.
Mathis, J. S., Mezger, P. G., and Panagia, N. 1983, *Astr. Ap.*, **128**, 212.
Meyer, D. M., and Ulrich, R. K. 1984, *Ap. J.*, **283**, 98.
Miller, J. S., and Mathews, W. G. 1972, *Ap. J.*, **172**, 593.
Namioka, T. 1964, *J. Chem. Phys.*, **40**, 3154.
Pankonin, V., and Walmsley, C. M. 1976, *Astr. Ap.*, **48**, 341.
———. 1978, *Astr. Ap.*, **67**, 129.
Pottasch, S. R., Goss, W. M., Arnal, E. M., and Gathier, R. 1982, *Astr. Ap.*, **106**, 229.
Raymond, J. C., Black, J. H., Dupree, A. K., Hartmann, L., and Wolff, R. S. 1981, *Ap. J.*, **246**, 100.
Rieke, G. H., Cutri, R. M., Black, J. H., Kailey, W. F., McAlary, C. W., Lebofsky, M. J., and Elston, R. 1985, *Ap. J.*, **290**, 116.
Rieke, G. H., Lebofsky, M. J., Thompson, R. I., Low, F. J., and Tokunaga, A. T. 1980, *Ap. J.*, **238**, 24.
Rieke, G. H., Lebofsky, M. J., and Walker, C. E. 1987, *Ap. J.*, submitted.
Roberge, W. G. 1981, Ph.D. thesis, Harvard University.
Roberge, W. G., Dalgarno, A., and Flannery, B. P. 1981, *Ap. J.*, **243**, 817.
Sandlin, G. D., Bartoe, J.-D. F., Brueckner, G. E., Tousey, R., and VanHoosier, M. E. 1986, *Ap. J. Suppl.*, **61**, 801.
Savage, B. D., Bohlin, R. C., Drake, J. F., and Budich, W. 1977, *Ap. J.*, **216**, 291.
Schwartz, R. D. 1974, *Ap. J.*, **191**, 419.
———. 1983, *Ap. J.* (*Letters*), **268**, L37.
Schwartz, R. D., Cohen, M., and Williams, P. M. 1987, *Ap. J.*, **322**, 403.
Schwartz, R. D., Dopita, M. A., and Cohen, M. 1985, *A.J.*, **90**, 1820.
Sellgren, K. 1984, *Ap. J.*, **277**, 623.

Sellgren, K. 1986, *Ap. J.*, **305**, 399.
Sellgren, K., Allamandola, L. J., Bregman, J. D., Werner, M. W., and Wooden, D. H. 1985, *Ap. J.*, **299**, 416.
Shull, J. M. 1978*a*, *Ap. J.*, **219**, 877.
———. 1978*b*, *Ap. J.*, **224**, 841.
Shull, J. M., and Beckwith, S. 1982, *Ann. Rev. Astr. Ap.*, **20**, 163.
Simon, T., and Joyce, R. R. 1983, *Ap. J.*, **265**, 864.
Smith, H. A., Larson, H. P., and Fink, U. 1981, *Ap. J.*, **244**, 835.
Snow, T. P. 1983, *Ap. J. (Letters)*, **269**, L57.
Spitzer, L., Cochran, W. D., and Hirshfeld, A. 1974, *Ap. J. Suppl.*, **28**, 373.
Spitzer, L., and Jenkins, E. B. 1975, *Ann. Rev. Astr. Ap.*, **13**, 133.
Sternberg, A. 1986, Ph.D. thesis, Columbia University.
Takayanagi, K., Sakimoto, K., and Onda, K. 1987, *Ap. J. (Letters)*, **318**, L81.
Tielens, A. G. G. M., and Hollenbach, D. 1985*a*, *Ap. J.*, **291**, 722.
———. 1985*b*, *Ap. J.*, **291**, 747.
Traub, W. A., Carleton, N. P., and Black, J. H. 1978, *Ap. J.*, **223**, 140.
Turner, J., Kirby-Docken, K., and Dalgarno, A. 1977, *Ap. J. Suppl.*, **35**, 281.
van Dishoeck, E. F., and Black, J. H. 1982, *Ap. J.*, **258**, 533.
———. 1986, *Ap. J. Suppl.*, **62**, 109 (vDB).
Webster, A. 1985, *M.N.R.A.S.*, **217**, 761.
Werner, M. W., and Harwit, M. 1968, *Ap. J.*, **154**, 881.
White, G. J., Phillips, J. P., and Watt, G. D. 1981, *M.N.R.A.S.*, **197**, 745.
Witt, A. N., and Schild, R. E. 1986, *Ap. J. Suppl.*, **62**, 839.
Witt, A. N., Schild, R. E., and Kraiman, J. B. 1984, *Ap. J.*, **281**, 708.
Wynn-Williams, C. G., Heasley, J. N., DePoy, D. L., Hill, G. J., and Becklin, E. E. 1986, *Ap. J.*, **304**, 409.

JOHN H. BLACK: Steward Observatory, University of Arizona, Tucson, AZ 85721

EWINE F. VAN DISHOECK: Princeton University Observatory, Peyton Hall, Princeton, NJ 08544